



NTNU – Trondheim
Norwegian University of
Science and Technology

Failure Mechanisms in Cutter Tools for Tunnel Boring

Jarand Nærland

Materials Science and Engineering

Submission date: June 2015

Supervisor: Nuria Espallargas, IPM

Co-supervisor: Javier Macias Rico, BAT

Norwegian University of Science and Technology
Department of Engineering Design and Materials

Abstract

Tunnel boring machines (TBM) utilize cutter discs as a primary tool for cutting through hard rock. The discs are mounted on a rotating, circular cutter head which is pressed against the rock. A microscopical examination of worn cutter discs has been carried out. The goal was to map fracture mechanisms on TBM cutters with different reason of change, position on the cutter head and rock mass involved. Testing was performed on samples from a full scale TBM and from a novel test method for cutter wear assessments on hard rock tunnel boring recently developed by NTNU. This method is called the Rolling Indentation Abrasion Test (RIAT).

The mode of contact for TBM cutters was found to be rolling, while RIAT mini-cutters cutters also experienced a minor sliding component. Abrasive wear was dominant in both sample types. An increase in fatigue wear was seen in TBM cutters as rock abrasivity decreased. This was credited longer cutter life and larger fluctuations in load. The presence of nanocrystalline deformation layers of comparable thickness in both sample types indicate similar deformation in the two processes.

A furnace test on undeformed TBM cutter material was performed to correlate temperature and holding time with the sample hardness profiles. Comparison of hardness measurements and tempering results indicate a surface temperature in excess of 620 °C in three TBM cutters. This temperature is given a holding time of one hour. The temperature gradient was seen to correlate with depth of deformation in the material. A high deformation rate is believed to account for steep hardness gradients found. No estimate for surface temperature was found for the RIAT mini-cutters.

Samandrag

Tunnelboremaskinar (TBM) nyttar ståldiskar som primært kuttemedium for boring i hard stein. Diskane er festa radiaalt på eit sirkulært, roterande kuttehovud som vert pressa mot bergveggen. Ei undersøking av slitte ståldiskar har vorte gjennomført med lys- og elektronmikroskopi og hardleiksmålingar. Målet med undersøkinga er å kartleggje brotmekanismar i TBM ståldiskar. Diskane har ulik grunngeving for utskifting, kjem frå ulike posisjonar på kuttehovudet og er nytta i ulike bergartar. Prøvene vart henta frå ei fullskala tunnelboremaskin og ei nyutvikla testmetode for slitasjemåling på TBM-diskar for hard stein, utvikla ved NTNU. Metoden vert kalla the Rolling Indentation Abrasion Test (RIAT).

Resultat frå undersøkinga syner at kontaktmoduset for TBM kuttarar er rulling. Rulling er óg dominerande kontaktmodus for RIAT mini-kuttarane, men desse har i tillegg ein liten glidande komponent. Abrasiv slitasje var dominerande i baae prøvetypar. Ei auke i utmattingsbrot vart observert i samband med redusert abrasivitet i berget. Dette skuldast truleg auka levetid på kuttarane i kombinasjon med ei høgare lastvariasjon i desse områda. Nanokrystalline deformasjonslag vart funnet i baae prøvetypar. Tjukklikeken på laga i dei ulike prøvetypane var samanliknbar, noko som indikerer tilsvarande deformasjon i dei to prosessane.

Eit anløpingsforsøk vart gjennomført på ei udeformert TBM-prøve for å korrelere hardleiksmålingar frå brukte prøvar til kjente temperaturer og haldetidar. Ein overflatetemperatur på omlag 620 °C vart funnet i tre TBM prøvar. Temperaturen vart funnen med ei haldetid på Æ ein time. Temperaturgradientane var i samsvar med deformasjonen observert i prøvene. Høg deformasjonsrate er truleg kopla saman med dei høge hardleiksgradientane observert i fleire av prøvene. Ingen temperaturestimater vart gjennomført for RIAT-prøvene.

Preface and Acknowledgements

This master's thesis is carried out for the Department of Engineering Design and Materials at NTNU. It is a cooperative project, supported by the Department of Materials Science and Engineering and the Department of Civil and Transport Engineering.

The goal of this thesis is to understand the basic mechanisms producing wear on steel cutter discs for Tunnel Boring Machines (TBMs). Samples were collected from a full scale tunnelling project in Røssåga and compared to small scale samples from a novel wear test developed for hard rock TBMs. The analysis includes microstructure examination, tempering and hardness measurements. Sample preparation and electron- and optical microscopy has been performed at the labs at the Department of Materials Science and Engineering. The nanocrystalline deformation layer was studied at NTNU NanoLab and the nano indentations were performed at the Department of Engineering Design and Materials.

The author wishes to thank supervisor Nuria Espallargas for her guidance during this project work. In addition, co-supervisor Javier Macias has been very helpful, especially when trying to understand the geological parameters affecting wear on the steel discs. The sample preparations and etching would not have been possible without instruction and guidance from Trygve Schanche. Gratitude is also given to Amin Hossein Zavieh for guidance with FIB imagery and Prof. Bjørn Holmedal for help on plastic deformation theory.

A special thanks is given to Christian O. Paulsen for his technical assistance by problem solving during the programming of this report, and to Kristian Knarbakk for proofreading everything I wrote. Lastly, I thank my wife Elisabeth for patiently bearing with me during the finalizing of this thesis. I am truly blessed.

Trondheim, 11.06.15



Contents

Abstract	i
Samandrag	ii
Preface and Acknowledgements	iii
List of Abbreviations	vi
List of Equations	vii
List of Figures	vii
List of Tables	x
1 Introduction	1
1.1 Background	1
1.2 Objective	2
2 Theory	3
2.1 Tunnel Boring Machines	3
2.2 Cutter Discs	5
2.3 Steel and Microstructure	6
2.3.1 Steel and Martensite	6
2.3.2 Grains and Dislocations	7
2.3.3 Nanocrystalline Deformation Layers	10
2.3.4 Tempering	13
2.3.5 H13 Tool Steel	13
2.4 Mechanisms of Wear	14
2.4.1 Abrasive Wear	14
2.4.2 Fatigue Wear	16
2.4.3 Heat Generation	19
2.5 Rock Abrasivity and Cutter Wear	20
2.5.1 Rock Abrasivity Test Methods - State of the Art	20
2.5.2 Rolling Indentation Abrasion Test (RIAT) Method	23

2.5.3	Rock Type and Wear	25
3	Experimental	26
3.1	Samples	26
3.2	Metallography	29
3.2.1	Sample Preparation	29
3.2.2	Etching	29
3.2.3	Microscopes	30
3.3	Tempering	34
3.4	Hardness Measurements	35
4	Results	36
4.1	Field Data from Røssåga	36
4.2	Failure Mechanism Examination	44
4.2.1	Modes of Contact	44
4.2.2	Wear Mechanisms	49
4.2.3	Deformation Structure	57
4.3	Tempering	66
5	Discussion	76
5.1	Field Data from Røssåga	76
5.2	Failure Mechanism Examination	77
5.3	Tempering	79
6	Conclusion and Future Work	83
6.1	Conclusion	83
6.2	Future Work	84
	Appendices	89
A	Problem Text	90
B	Risk Analysis	93
C	Field Data from Røssåga	97
D	Failure Mechanism Examination	98
D.1	Modes of Contact	98
D.2	Wear Mechanisms	101
D.3	Deformation Structure	104
E	Tempering	105

List of Abbreviations

AVS - Abrasion Value cutter Steel

BSE - Backscattered Electrons

CAI - CERCHAR Abrasivity Index. Rock abrasivity index introduced by Centre d' Études et Rescherches des Charbonnages de France in 1986.

D&B - Drill and Blast

EBSD - Electron Backscatter Diffraction

EDS - Energy Dispersive Spectrometer

FIB - Focused Ion Beam

H13 - Industrial grade tool steel. Alloying elements decided within a certain range specific for this grade.

LAC - LCPC Abrasivity Coefficient. Rock abrasivity index introduced by Laboratoire Central des Ponts et Chaussées in the 1980's.

RIAT - Rolling Indentation Abrasion Test

SEM - Scanning Electron Microscope

TBM - Tunnel Boring Machine

TMCP - Thermomechanical Control Processing

UCS - Uniaxial Compressive Strength

List of Equations

2.3.1	Hall-Petch relationship	10
2.3.2	True strain	11

List of Figures

2.1	Wilson's improved TBM	3
2.2	Gripper TBM	4
2.3	Rock chipping by cutter discs	4
2.4	Refurbished and worn cutters	5
2.5	Typical cutter disc design	5
2.6	Iron-carbon phase diagram	6
2.7	Illustration image of martensite	8
2.8	Misalignment in crystal structure	9
2.9	Edge dislocation in a crystal lattice	10
2.10	Production methods for different grain size ranges	11
2.11	Illustration of strain	11
2.12	Hardness of a nanocrystalline region of Fe-0.80 %C pearlitic sample	12
2.13	Abrasive mechanisms	15
2.14	Deformation layer illustration	16
2.15	Deformation layer in H13 tool steel	16
2.16	Effect of re-adhesion and oxide layers	17
2.17	Surface deformation in sliding contact	17
2.18	Wear mechanism in rolling contact	18
2.19	Crack growth in lamellar surface layer	18
2.20	Local and global heating due to friction	19
2.21	CERCHAR test setup	20
2.22	LCPC test setup	21
2.23	AVS test setup	21
2.24	Experimentally measured force on cutters	22
2.25	The RIAT tool and the mini-cutter rings	24
2.26	Preliminary wear results from RIAT testing	25
3.1	The TBM used in Røssåga	26
3.2	Uncut samples	27
3.3	Effect of sample cutting on microstructure	29
3.4	Leica MEF4 optical microscope	31
3.5	FIB instrument and cross section	32
3.6	FIB milling steps	33

3.7	Furnace used for tempering	34
3.8	Hardness indenter and indentation	35
3.9	Micro hardness indenter	35
4.1	Overview of wear mechanisms on the Røssåga TBM	36
4.2	Reasons for cutter changes on all cutter head positions	37
4.3	Overview of cutter positions from cutter head center	38
4.4	Cubic meters of rock per cutter versus tunnel progress on TBM at Røssåga	40
4.5	Cubic meters of rock per cutter versus tunnel progress on TBM at Røssåga	42
4.6	Cubic meters of rock per cutter versus tunnel progress on TBM. Linear comparison	43
4.7	Contact mode in TBM cutter disc 314	44
4.8	Contact modes of RIAT mini-cutter 8, worn by quartzite	45
4.9	Contact modes of RIAT mini-cutter 11, worn by quartzite	46
4.10	Contact mode of RIAT mini-cutter 003, worn by granite	47
4.11	Contact mode of RIAT mini-cutter 001, worn by Chinese basalt	48
4.12	Wear mechanisms in TBM cutter 302, transverse cross section	49
4.13	Wear mechanisms in TBM cutter 302, parallel cross section	50
4.14	Wear mechanisms in TBM cutter 302, parallel cross section	51
4.15	Folding in RIAT mini-cutter 002, worn by Chinese basalt	52
4.16	Folding in RIAT mini-cutter 3, worn by Iddefjord granite	53
4.17	Abrasion on wear surface. Sample 4, worn by quartzite	54
4.18	Abrasion on wear surface. Sample 6, worn by Iddefjord granite	55
4.19	SEM image of wear surface of RIAT mini-cutter 3, worn by Iddefjord granite	56
4.20	TBM cutter disc 314, transverse cut cross section	57
4.21	FIB microstructure in TBM cutter 302, transverse cut cross section	58
4.22	FIB microstructure in TBM cutter 302, parallel cut cross section	59
4.23	FIB microstructure in TBM cutter 140, parallel cut cross section	60
4.24	FIB microstructure in TBM cutter 140, transverse cut cross section	61
4.25	FIB microstructure in TBM cutter 383, transverse cut cross section	62
4.26	FIB cross section. Surface worn by Chinese basalt, sample 002, transverse cut cross section	63
4.27	FIB image of RIAT mini-cutter 3, worn by Iddefjord granite	64
4.28	FIB cross section. Surface worn by Quartzite, sample 11, transverse cut cross section	65
4.29	Hardness profiles of TBM cutter 314, slice 1	66
4.30	Hardness profiles of TBM cutter 314, slice 2	67
4.31	Hardness profile of TBM cutter 302	67
4.32	Hardness profile of RIAT mini-cutter 3, worn by Iddefjord Granite	68
4.33	Hardness profile of TBM cutter 140	69

4.34	Hardness profile of TBM cutter 383	70
4.35	Hardness results of tempered HD4	71
4.36	Hardness results of tempered HD4 with TBM cutter 140, 314 (slice 1) and 383 surface hardness indicated	72
4.37	Hardness profiles of tempered HD4 with TBM cutter 140 hardness indicated	73
4.38	Hardness profiles of tempered HD4 with TBM cutter 314, slice 1, hardness indicated	74
4.39	Hardness profiles of tempered HD4 with TBM cutter 383 hardness indicated	75
C.1	Overview of cutter positions on TBM cutter head	97
D.1	Optical image of TBM cutter 140	98
D.2	Optical image of TBM cutter 302	99
D.3	Optical image of cross section in TBM cutter 383	100
D.4	Optical image of cross section in TBM cutter 314	101
D.5	SEM image of wear surface of RIAT mini-cutter 8, worn by quartzite	102
D.6	SEM image of wear surface of RIAT mini-cutter 7, worn by basalt . .	103
D.7	FIB image of RIAT mini-cutter 3, worn by Iddefjord granite	104
E.1	Hardness profiles of tempered HD4 with TBM cutter 140 hardness indicated	105
E.2	Hardness profiles of tempered HD4 with TBM cutter 383 hardness indicated	106
E.3	Hardness profiles of tempered HD4 with TBM cutter 314 hardness indicated	106

List of Tables

2.1	Effect of alloying elements in tool steels	7
2.2	Typical alloying composition of H13 tool steel	14
2.3	AVS classification of rock abrasion	22
3.1	Probable composition of the samples from Røssåga.	27
3.2	Composition of the H13 tool steel used in the RIAT samples	27
3.3	Sample overview	28
3.4	Etchants used for optical microscopy imaging	30
3.5	Steps in FIB milling	33
4.1	TBM cutter log	41

Chapter 1

Introduction

1.1 Background

Tunnel boring machines (TBMs) are gaining presence as a suitable method on underground expansion especially for long tunnels. In doing so, they encounter a great variability of geologies, ranging from soft clay to very hard rock. Due to the large investments involved in long tunnels excavated by tunnel boring, planning and risk management take a great importance for the technical success of the projects. To create estimates for building costs, geological back-mapping of tunnels is continuously performed. The combination of rock parameters, intact rock and rock mass are the basis of these prediction models.

An important parameter for tunnelling costs by TBMs is their cutter disc consumption. The cutters are continuously worn out as boring takes place and are immensely affected by the above mentioned geological parameters. Replacement of cutters can in some rock formations amount to 15 % of the total tunnelling cost. In some cases, worn out cutter tools, and in fact worn out cutter head structures, can jeopardize whole tunnelling projects. As of yet, few projects have studied the effect on steel cutters microstructure from different geological formations. The knowledge of how wear is affected by microstructural changes may be used to further improve our understanding of cutter disc life. This knowledge may further improve the current tunnel boring technology and cost estimates.

To more accurately predict wear rates on cutter discs in hard rock tunnel boring, a novel test method for cutter wear assessments on hard rock tunnel boring was recently developed by NTNU. Previous wear tests use crushed rock and sliding contact as abrasive medium, grinding at a mounted steel sample. The new test method utilizes rolling contact over intact rock to produce wear. Sample analysis from this testing will be included in this master's thesis.

1.2 Objective

The goal of this master's thesis is to investigate the cause of failure and the temperatures reached at the contact surface of failed cutter rings from a real tunnel project. Worn samples from the novel hard rock test method will be included as part of this thesis to study differences and similarities to the full scale samples. By understanding the wear mechanisms working in both full and small scale boring, it may be possible to more accurately, and cost effectively, produce wear estimates for cutter consumption. If successful, the results may also improve tunnel boring technology. The problem text in full is found in Appendix A.

Specific objectives of this master's thesis are:

- Identify the degradation mechanisms (microstructural changes) by using material characterization techniques
- Record microstructure and hardness of the discs to correlate the changes in mechanical properties to tempering due to heating during use
- Identify the temperature achieved in the cutter tool - rock interface during the boring process by analyzing microstructure and hardness changes
- Compare real failures (field data) to lab scale testing
- Identify the role of the geology in the degradation/failure of the tools

Chapter 2

Theory

2.1 Tunnel Boring Machines

Perhaps the first to consider mechanised horizontal drilling through hard rock was Leonardo da Vinci [1]. Although a drawing has never been found in his sketches, his notes explain methods of both horizontal and vertical drilling, indicating that this idea was not unknown to him.

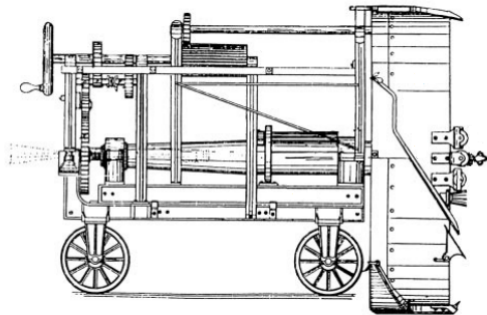


Figure 2.1: Wilson's improved machine. Built in 1857. Adapted from [2].

No further development is recorded until the first working TBM was patented by Charles Wilson in 1856. The improved version of the original design is shown in Figure 2.1. It was used to build the 7645 m Hoosac tunnel in Massachusetts, USA [2]. Although TBMs were used in various tunnelling projects, troubles with reliability and efficiency of the design hampered their practical use for almost a century. James Robbins built a machine resembling the present design in 1953. It utilized a combination of fixed and rotating steel disc cutters, and set a world record for production length per 8

hours (18.5 m) and 24 hours (49 m) [2]. The ground was soft Pierre shale and could therefore not be considered rock but it was a clear indication of the potential of a TBM.

TBMs excavates a circular cross section with sizes usually varying from 2.5 to 15 m [3]. They may be utilized in most ground classes but often require a certain sustainability of the geological formations to obtain a solid support structure. If the rock structure is not solid by its own, as is the case e.g. in soil, a concrete mantel may be constructed during boring. The supporting concrete will provide stability of the advancing machine. Failure in this stabilizing construction or the geology itself may cause the TBM front to become buried, causing a delay in construction progress

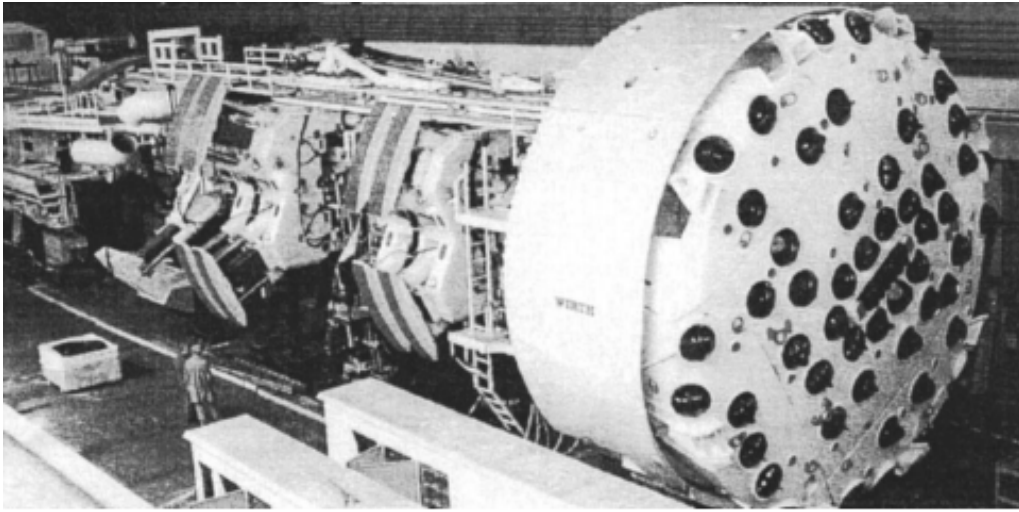


Figure 2.2: Gripper tunnel boring machine in factory [3].

of potentially several months. Modern machines are distinguished by which type of rock they excavate, namely soil and rock. A rock type gripper TBM is shown in Figure 2.2 for reference. This type of TBM does not build a concrete mantle, relying solely on the quality of the rock mass for stability. The research presented in this work will be based on hard rock TBMs similar to this machine.

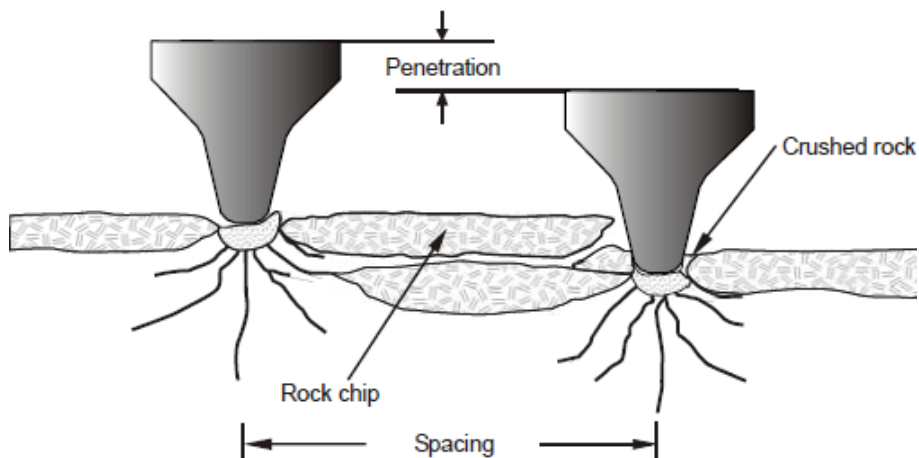


Figure 2.3: Rock chipping by cutter discs [4].

The TBM digs its way forward by pressing the cutter head towards the rock while rotating it [5]. Mounted on the cutter head are steel discs which roll and slide along the rock. Applied pressure acts both as a driving force for the rock grinding process and as a balance force to stabilize the surroundings. The contact pressure directly beneath the surface pulverize the rock forming grooves [4]. As seen in Figure 2.3, cracks form on the bottom of two neighbouring grooves and combine to cut off the wall between them. Debris is extracted by transport screws and conveyor belts.

2.2 Cutter Discs



Figure 2.4: **a)** Cutters with new outer rings ready for use. **b)** Worn discs replaced due to general wear.

Cutter discs are exposed to extreme wear during use. For this reason, cutter disc design allows for replacement of the outer ring individually, given that the bearing is intact.

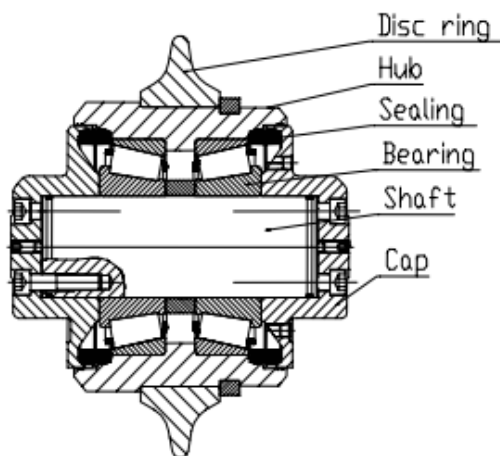


Figure 2.5: Typical cutter disc design [6].

Figure 2.4a shows refurbished cutters ready for use. General wear is apparent in Figure 2.4b, showing cutters removed for refurbishing. The layout of a disc cutter is shown in Figure 2.5. Replacement of the rings occur either when the limit for allowable general wear is reached, or when special types of wear, namely chipping or blocking is discovered during inspection.

Abrasive wear dominate the main reason of cutter change in normal TBM operation conditions [5]. Often also in combination with a certain degree of fatigue and chipping. Failure to replace rings with these types of wear may lead to lower efficiency of the boring process and destruction of the bearing, other discs or the entire cutter head. Such replacements will increase the maintenance costs considerably and decrease the TBM performance.

2.3 Steel and Microstructure

2.3.1 Steel and Martensite

Steel is per definition an alloy of iron and carbon but usually consist of a number of different alloying elements [7]. Its mechanical properties varies greatly with the alloying content and the thermo-mechanical process applied to produce the finished product. The carbon content of different steel alloys introduce quite a significant effect of mechanical properties due to the positioning of carbon in the iron lattice.

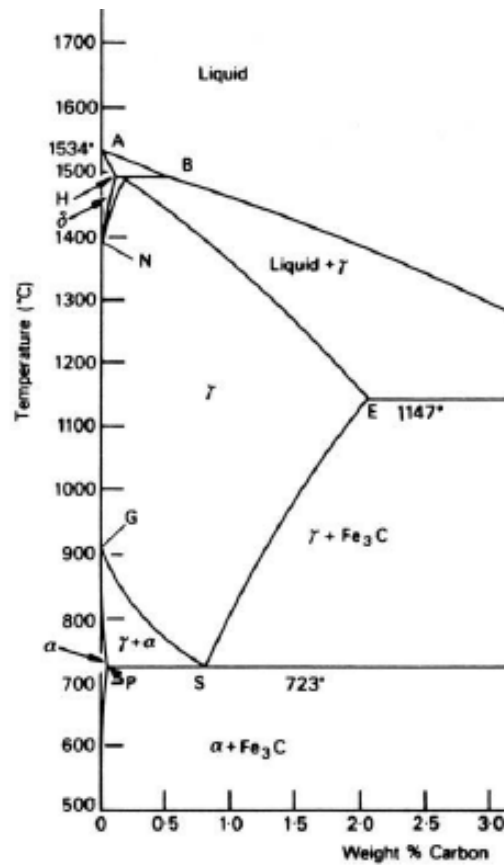


Figure 2.6: Iron-carbon phase diagram. Adapted from [8].

As shown in Figure 2.6, at ambient pressure, iron and low alloy steel have three stable allotropes. These are body-centred cubic (ferrite, α and δ) and face-centred cubic (austenite, γ). During the forming process, the steel is heated to a temperature in the austenite area and subsequently quenched to room temperature. Slow cooling of austenite leads to the formation of ferrite. The solubility of carbon in austenite greatly exceeds that in ferrite and at lower temperatures, a carbon rich phase is formed by diffusion to avoid supersaturation. When rapidly quenched, diffusion does not have sufficient time to occur and bainite or martensite are then formed. Both are very hard and brittle phases separated by the superior cooling speed of

the latter. The martensite will be supersaturated with carbon. The supersaturation leads to a hard and brittle material if not properly heat treated.

The cutter discs used in TBMs are made of martensitic tool steel. The term tool steel dictates a high carbon content, leading to easy martensite formation [9]. It is coined from the frequent use of this alloying type in hot and cold working tools. Other elements are added to obtain certain properties to the material. Some of these are described in Table 2.1. As alloy composition and heat treatment used to produce TBM discs are regarded as company secrets, this study will use a known industrial grade tool steel named H13. The properties of this steel are further described in Section 2.3.5.

Table 2.1: Effect of alloying elements in tool steels [9].

Element	Effect
C	Increase hardenability and hardness. Forms carbides during tempering stages.
Ni	Increase hardenability and ductility.
Mn, Si	Increase hardenability. Used as de-oxidizing agent.
Mo, Cr, W	Increase hardenability. Forms carbides if tempered above 500 °C. The carbides increase hardness and abrasive resistance in general and improve temperature resilience of the steel due to carbide stability at high temperatures.
V	Forms carbides which give precipitation hardening. Reduce hardenability.

As previously mentioned, martensite forms without any diffusion of atoms by deformation of the austenite crystal lattice. This leaves the material with a supersaturation of carbon occupying interstitial positions of the atomic lattice. The extra atoms push the lattice apart, giving martensite a body-centred tetragonal unit-cell, similar to the cubic α -structure of ferrite with a slightly elongated z-axis. The transformation is normally athermal, requiring continuous cooling to proceed and it induces significant plastic deformation to the material. In order to minimize the strain energy of the deformation when constrained by its surroundings, martensite forms as laths or thin plates. A martensitic microstructure is shown in Figure 2.7. Plastic deformation may also induce martensitic transformation. Both the plastic deformation induced by the transformation and from external pressure will increase the hardness and reduce ductility of the material [7].

2.3.2 Grains and Dislocations

A well known and exploited strengthening mechanism in metals is grain refinement. To understand this effect the subject of grains and dislocations must first be explained.

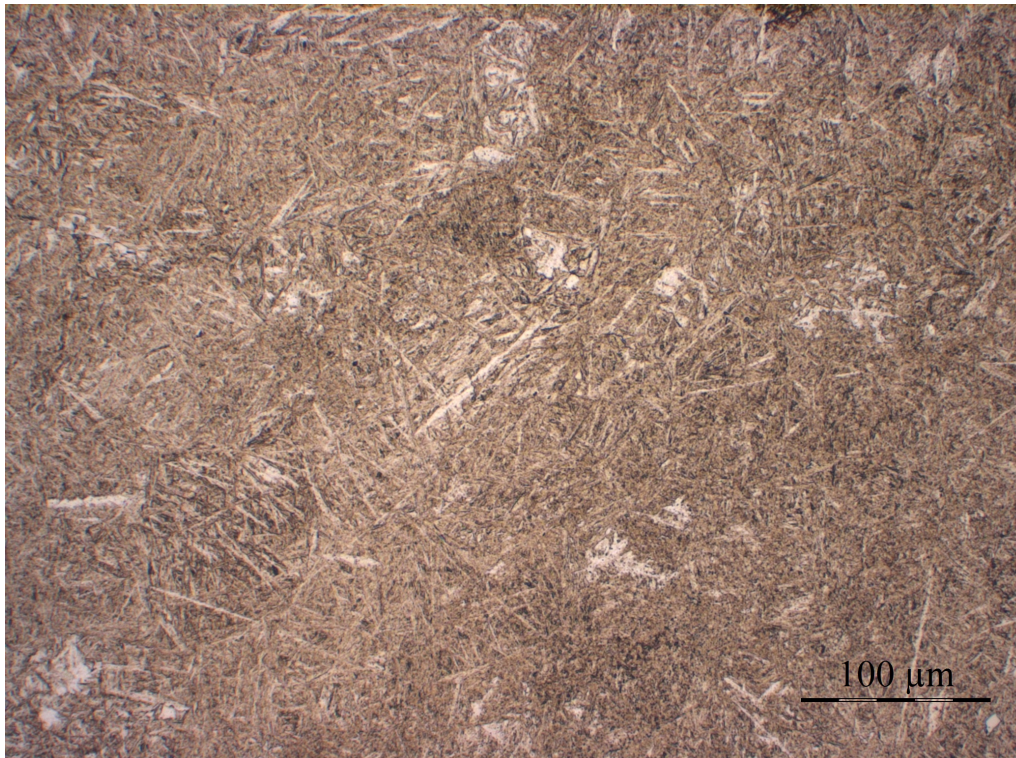


Figure 2.7: Optical image of martensitic microstructure. Gray phase: martensitic laths. White phase: retained austenite. Etched with Kallings no. 2. 200X magnification.

Solidification of metals occurs by the growth of crystals [7]. The most commonly known analogue to this process in metals is the formation of ice crystals during freezing of water. The atoms in a material are arranged in specific lattices in each crystal but their growth directions will vary, giving different degrees of misalignment in the solid material [10]. This is illustrated in Figure 2.8. In metallurgy, the different crystals are called grains and the interfaces between them are dubbed grain boundaries.

In all metals, plastic deformation creates dislocations. A dislocation may be seen as a plane of atoms which abruptly stops. This plane is called a dislocation line. They are formed in order to minimise the strain energy which is stored in the lattice during plastic deformation and moves by the breaking and forming of bonds between adjacent atoms [11].

Principally, two types of dislocations exist. They are distinguished by the way they form new bonds. An edge dislocation will form new bonds with atoms perpendicular to the dislocation line, parallel to the direction of movement, as illustrated in Figure 2.9. A screw dislocation will form new bonds perpendicular to the direction of movement, parallel to the dislocation line. Usually, dislocations are mixtures of these two types.

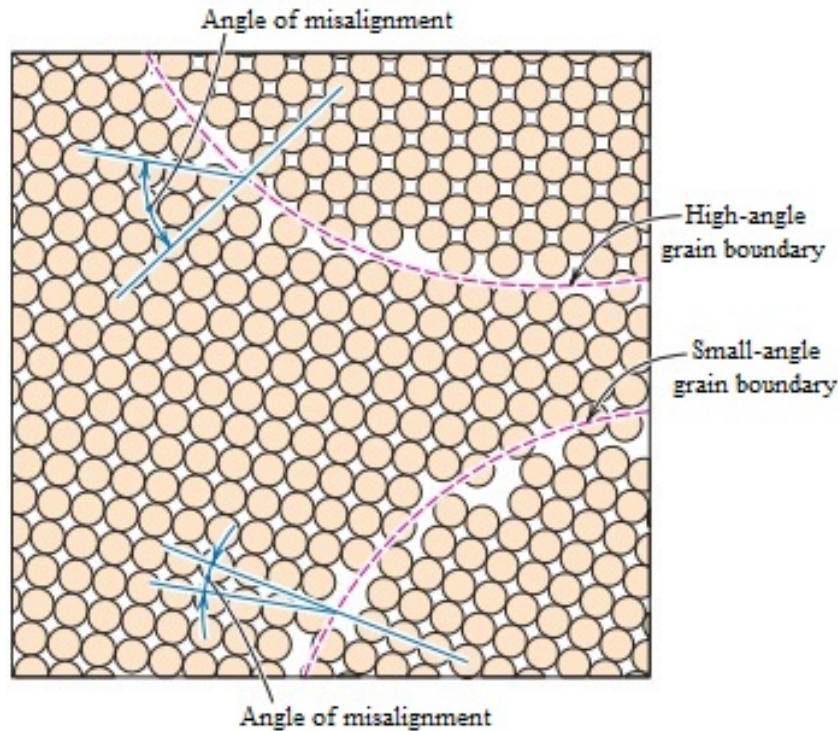


Figure 2.8: Misalignment in crystal structure [10].

If not for dislocation movement, metals would not be deformable. Readily moving dislocations correspond to an easily deformed, soft metal. The greater hindrance a dislocation face from movement, the higher yield and tensile strength of the metal. Work hardening is the generation of dislocations through plastically deforming a metal. The dislocations effectively lock each other, increasing the hardness of the metal. Other effective methods of hindering dislocation movement are precipitation hardening and through the addition of carbon. Small, finely spread precipitates hinder dislocation movement, either by being too hard for dislocations to shear, or by the energy required to create new surface when a precipitate is sheared by progressing dislocations [11]. If the precipitates coarsen through heat treatment, the strengthening effect will dissipate. Large precipitates at grain boundaries may even be detrimental to the mechanical properties of the metal. As for hardening by carbon addition, stresses surrounding the carbon atom in the crystal lattice hinder the dislocations, thereby increasing strength. The supersaturation of carbon in martensite is highly effective at hindering dislocation movement and, in combination with few slip systems, results in the brittle and hard microstructure described in section 2.3.1 [10].

During deformation, the dislocations move in certain atomic planes specific to the materials crystal structure. Due to the misalignment between the orientations of neighbouring grains, extra energy is required to transfer a dislocation from one

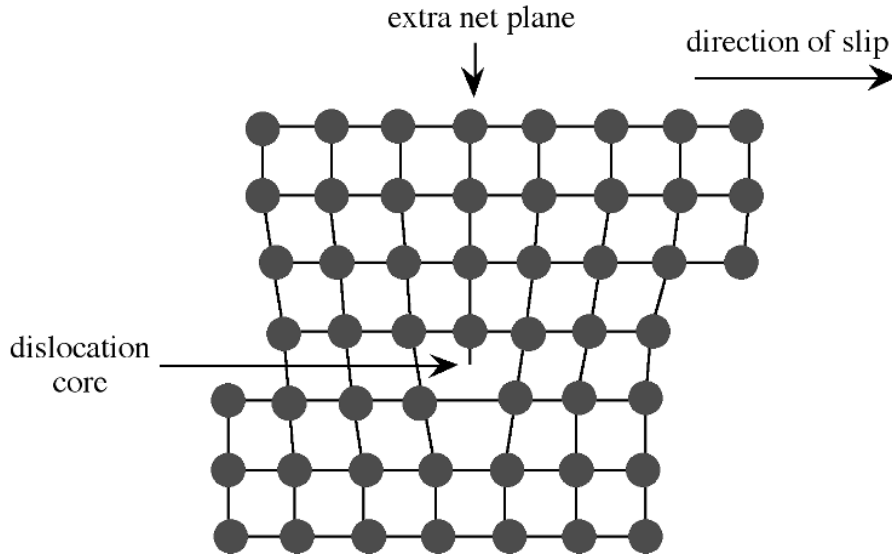


Figure 2.9: Edge dislocation in a crystal lattice [12].

grain to another. This hindering cause an increase in strength and is described by the Hall-Petch relation shown in Equation 2.3.1 [10].

$$\sigma_y = \sigma_o + \frac{k}{\sqrt{d}} \quad (2.3.1)$$

Here, σ_y is the yield strength of the metal, σ_o is the friction stress, k is a material constant and d is the grain size. The friction stress may be regarded as the yield stress in a single crystal.

The amount of dislocations piling at a grain boundary is proportional to the stresses affecting the neighbouring grains [7]. Fracture occurs when this stress transcend the material tensile strength. Smaller grains experience fewer dislocations at each grain boundary relative to large grained structures, giving greater ductility prior to fracture. Reduction in grain size is the only parameter known to increase both strength and ductility of a metal.

2.3.3 Nanocrystalline Deformation Layers

Grain refinement can be obtained in several ways, with phase transformation, particle nucleation and plastic deformation the most commonly used techniques [7]. The combination of these methods are used to obtain great strength in construction steels without the need for large amounts of expensive alloying elements. In thermomechanical control processing (TMCP) steels the average ferrite grain size may be as small as 5 to 10 μm in commercial grades. These are produced by a combination of strict temperature control and mechanical deformation. A practical limit for industrial scale TMCP production is believed to be 1 μm , which is reached

in laboratory scale testing [7]. For further reduction in grain size, other methods must be utilized as depicted in Figure 2.10.

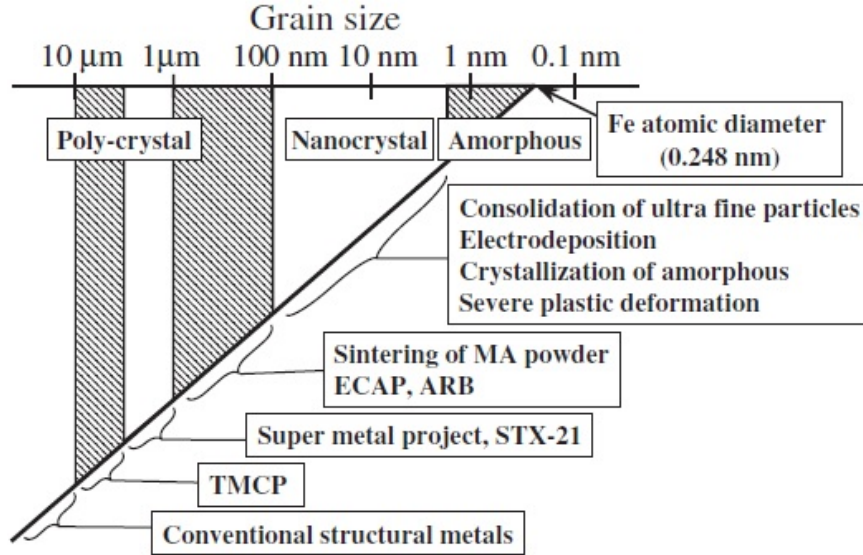


Figure 2.10: Production methods for different grain size ranges [13].

When subjected to severe deformation, a nanocrystalline grain structure may be formed. The minimum amount of strain needed to produce nanocrystalline structure is considered to be approximately 7-8. This does however depend on the material, microstructure and deformation conditions [13]. True strain is defined as shown in Equation 2.3.2 [11]. Here, ϵ is the true strain, t_0 is the grain height prior to deformation and t is the grain height after deformation.

$$\epsilon = \ln\left(\frac{t_0}{t}\right) \quad (2.3.2)$$

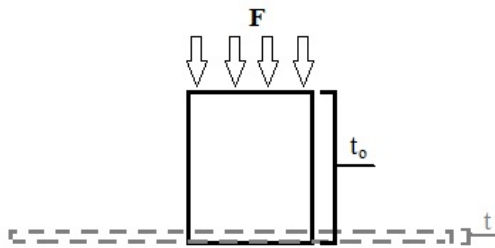


Figure 2.11: Illustration of strain. A grain is deformed from thickness t_0 to t .

The practical meaning of strain is illustrated by using Equation 2.3.2 and a simplified grain shown in Figure 2.11. Deforming a grain with original size, $t_0 = 150 \mu\text{m}$, to $t = 100 \text{ nm}$, gives a strain of $\epsilon = 7.31$. Little is known of the underlying mechanisms of grain refinement by plastic deformation but the foundation for the most commonly accepted models is grain fragmentation by dislocation wall formation [14]. The walls of dislocations form subgrains which are further fragmented by yet more wall formation. This self-organization of the dislocations is

one of the greatest unsolved problems in dislocation theory. The scope of this report does not include dislocation modelling and further theory on grain refinement will therefore not be presented.

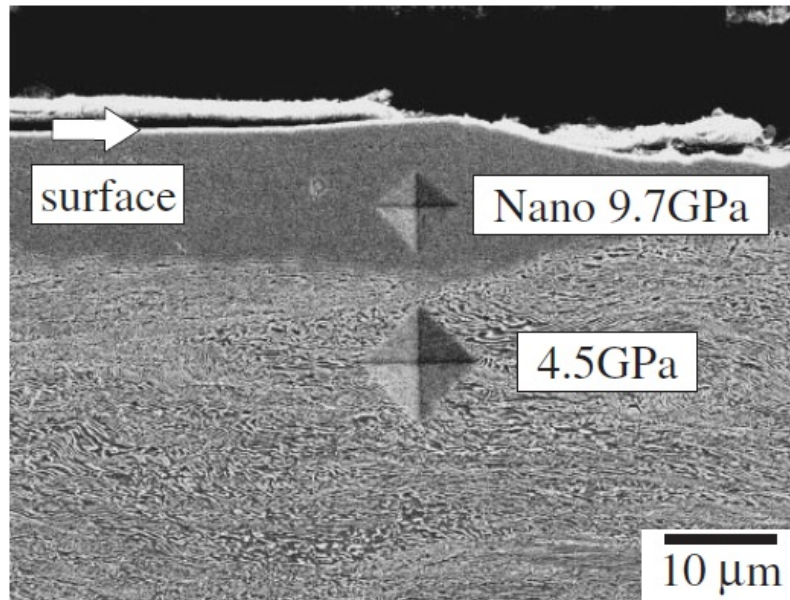


Figure 2.12: Hardness of a nanocrystalline region of Fe-0.80 %C pearlitic sample [13].

From Equation 2.3.1, a nanocrystalline crystal structure may be expected to possess superior yield strength relative to the larger grained areas of the metal. In addition, the ductility should be higher following the argumentation made in Section 2.3.2. The increase in hardness is seen in Figure 2.12. It should however be noted that the Hall-Petch relation has been shown in some studies to be inadequate when handling grains of less than $1\ \mu\text{m}$ [15].

Due to a low dislocation density after deformation, as all dislocations form cell walls, the rate of work hardening in nanocrystalline material is low. This leads to low tensile ductility. The dominating deformation mechanisms are found to depend greatly on grain size, with smaller grains ($< 100\ \text{nm}$) not able to support generation of dislocations due to size issues. In general, ductility is significantly lower when dislocations cannot contribute [15].

The fine grained structure in nanocrystalline layers is also found to have higher resistance to fatigue from cyclic load relative to the more conventional grain sized materials. This effect is credited to higher yield stress. In contrast, it has been found that the da/dN crack growth velocities are higher. This is believed to follow the finer fracture scale of smaller grains [15].

2.3.4 Tempering

Tempering is used to improve the toughness of brittle phases such as martensite. It involves reheating the quenched steel, usually to temperatures between 250 and 650°C [10]. Already at 100°C carbon starts to diffuse from its interstitial positions [7]. Thin needles of ϵ -phase form throughout the matrix while relaxing some of the lattice strain of the martensite. This causes an increase in ductility and a reduction in strength. The relaxation of the crystal lattice causes a partial change in crystal structure from bct to bcc.

The ϵ -particles are small and densely distributed enough to cause precipitation strengthening, reducing some of the strength lowering effects from tempering. Tempering at 200-350°C will allow the excess carbon in the martensite matrix to diffuse into carbide phases of Fe_3C -particles while the martensite essentially transforms to ferrite [7]. The new carbide phase nucleates at the ϵ -phase and leads to larger particles, reducing the precipitation strengthening effect. Higher temperature will coarsen the Fe_3C -particles and reduce the dislocation density in the material. Resulting from this treatment is an increased ductility while the fine ferrite structure provides good mechanical strength [10]. The sum of these properties is termed improved toughness.

The tempering effect is highly time dependent. Even though carbon may start diffusing at temperatures as low as 100°C, the time until the effect is measurable is significant. For tempering to be effective during short intervals of time, the temperature should be considerably higher. A 2 hour tempering of H13 tool steel showed a threshold temperature of 500°C for the hardening ϵ -phase to occur. At 550°C, effective reduction in hardness was apparent [16].

The free energy of a metal is increased during plastic deformation, mostly due to generation of dislocations [17]. A study performed on niobium-microalloyed steel revealed pre-deformation to initiate age hardening after 5 minutes versus 2 hours in undeformed material at 620 °C. The effect was mainly credited to the pre-deformation-induced strain energy, which could promote second-phase precipitation [18]. This increase may affect the tempering process in the cutter discs by lowering the required temperature for phase transformations or accelerate the reaction kinetics.

2.3.5 H13 Tool Steel

As previously mentioned in Section 2.3, H13 is an industrial grade tool steel. It has been chosen for use in the small scale testing as it is the steel base of several cutter ring manufacturers. Composition of a typical H13 steel is given in the Table 2.2. Several studies have investigated the effect of heat treatment on wear resistance for H13 [16, 19], which indicate a connection between heat treatment prior to use and wear properties. This is explained by softening of the martensite by carbon diffusion and formation of carbides in the matrix. In this study, only one tempering process will be used. This will introduce the opportunity to study the ongoing tempering of

the steel during use.

Table 2.2: Typical alloying composition of H13 tool steel [20].

C [wt%]	Mn [wt%]	Si [wt%]	Cr [wt%]	V [wt%]	Mo [wt%]
0.43-0.46	0.20-0.50	0.80-1.20	5.00-5.50	0.08-1.20	1.20-1.75

Because most tool steels are relatively hard, even when tempered, it is usually necessary to control carbide morphology during annealing to maximize machinability and formability [20]. Carbides and inclusions are natural crack initiation points in ductile materials. Round carbides will provide a larger crack tip radius than flat inclusions, directly affecting the crack driving force [21]. A spheroidal carbide shape is therefore the desired form.

Grain boundaries are very good nucleation sites for particles. Due to high C-content, incorrect heat treatment during forming can produce networks of carbides on austenite grain boundaries in H13 tool steels. These precipitates lead to reduced mechanical properties [20]. The presence of Mo and V may reduce this effect by also forming carbides, thereby reducing the amount of available carbon [7]. If the particles are small and finely dispersed, they may offer mechanical strength, as explained in Section 2.3.2.

2.4 Mechanisms of Wear

Wear is most readily described as an objects loss of mass due to its interaction with another material [22]. This section explains the concepts of abrasive and fatigue wear. A link between wear and microstructure is introduced and heat generation from friction and deformation is explained.

2.4.1 Abrasive Wear

In abrasive wear, a solid object is pressed against another of equal or greater hardness. The solid object experiences a mass loss as the harder counterpart press into it, thereby releasing wear debris. If the hardness of a given object is less than 80 % of the abrasive particle, severe abrasion may be expected [22].

Several different mechanisms usually produce wear simultaneously. The most dominant in metals are cutting, fracture and fatigue [22]. Illustrations of these mechanisms are given in Figure 2.13. Hard asperities pressed into a softer surface will remove material by cutting. This is a combination of micro-cutting and ploughing, where material is plastically deformed without removal. Wear by fracture involves brittle cracks propagating from the surface contact. When continuously loaded the accumulation of cracks along the surface may produce debris. The repeated load on the object may also lead to fatigue, even when the load is within the objects yield tolerance.

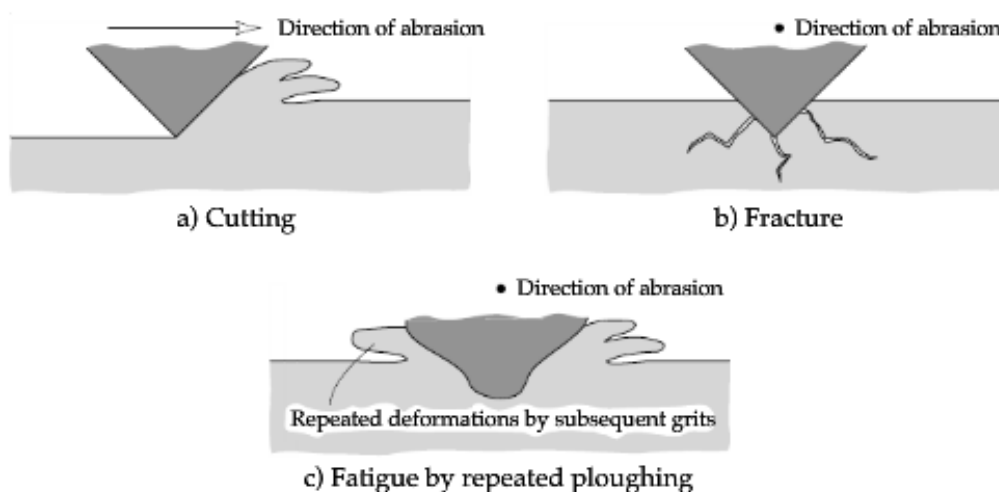


Figure 2.13: Abrasive mechanisms adapted from [22].

A separation can be made between two modes of abrasive contact, two- and three-body abrasion. In both modes, two surfaces move relative to each other. Two-body abrasion may be likened to sandpaper grinding a metal surface. The hard silica-particles are attached to the paper, and cuts into and deforms the softer material. Had the silica-particles of the sandpaper come loose, three-body abrasion would have occurred. The hard particles would then produce wear on either surface when clamped between the two. Cutting of silicone wafers and sample polishing in metallography utilize this mode of contact. Two-body abrasion is considered 10 times more effective than three-body mode [22].

Harder materials may be more resistant towards abrasion, but will be more vulnerable to fracture from knocks. The phase composition and microstructure of the material will determine its total abrasion resistance. Wear resistance of austenite and bainite is often better than that of martensite. The softer materials are often more ductile and will therefore have a superior toughness compared to the hard martensite [22]. This suppresses the abrasive mechanisms micro-cutting and fracture, reducing the overall wear.

The presence of precipitates may also affect the wear resistance by giving added strength or brittleness to the material. Effectiveness of the precipitates will depend highly on their size, volume fraction and nucleation points in the matrix. Alloying elements such as chromium, molybdenum, nickel and manganese give considerable improvements in abrasive wear resistance due to this effect [22]. The abrasive wear resistance of carbide containing steels have been found to be four times higher than carbide free steels of the same alloy [22].

2.4.2 Fatigue Wear

Wear does not depend solely on hard materials cutting into softer ones. Cyclic repetition of high local stresses will also generate wear. This is often the case between asperities during sliding or rolling where the wear is generated by fatigue propagated cracks [22].

Sliding

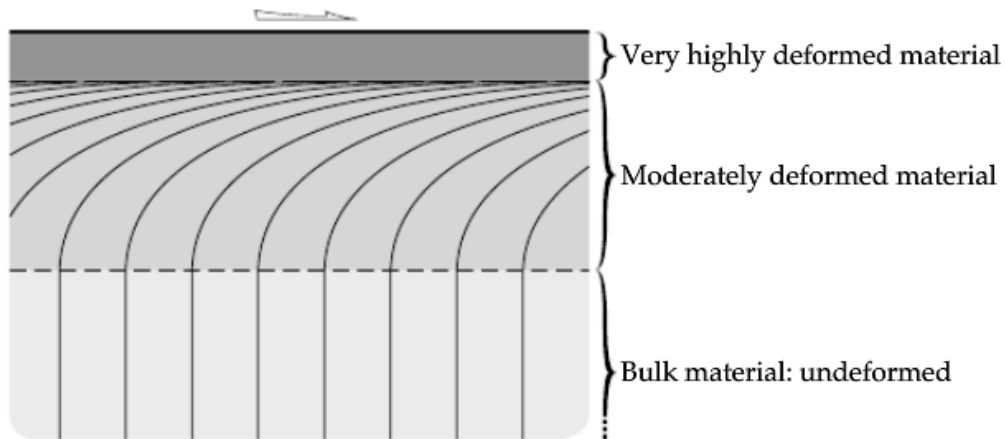


Figure 2.14: Deformation layer illustration [23]

Sliding motion combined with high friction has been shown to produce a deformation layer up to 0.1 mm deep into the surface of a metal [22]. This may be seen both in the illustration in Figure 2.14 and in the image of a worn H13 tool steel in Figure 2.15.

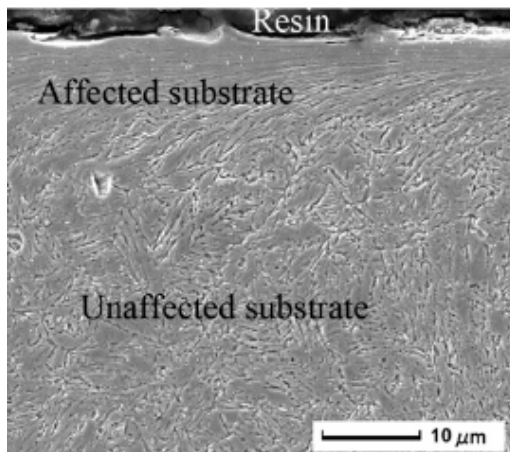


Figure 2.15: Deformation layer in H13 tool steel [16].

The thickness of this layer is dependent on the frictional forces acting on the bodies, and no layer is seen for low-friction contacts [22]. The strain induced by sliding will eventually break down the original grain structure close to the surface to form dislocation cells. The inside of the cells are free from dislocations as they have tangled together to form walls [24]. This new structure is found to resemble that of heavily worked metals [24].

Weak areas in the surface layer make easy nucleation points for crack formation if subject to frictional forces. These cracks will grow due to the cyclic load until they succeed in re-surfacing to produce debris by

chipping. To some extent, these cracks may be hindered by reattachment. Pressing the two crack surfaces together may cause them to adhere, preventing further crack growth. In steels, this effect is absent when oxygen is present. The oxide growth on the fracture surfaces will, as illustrated in Figure 2.16 prohibit adhesion and promote crack propagation [22]. The presence of water may accelerate this form of crack propagation, as it will increase the formation speed of the oxide layer.

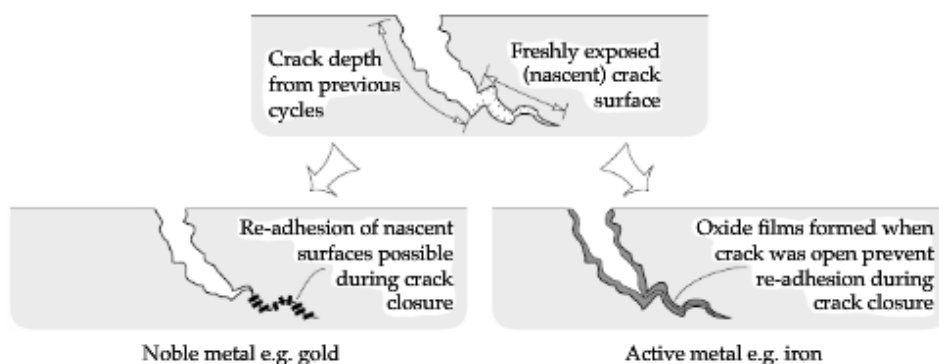


Figure 2.16: Effect of re-adhesion and oxide layer [22].

Cracks also initiate under the surface. Strain in the material just below a contact asperity may reach extreme values, but does not directly cause crack formation because of its triaxial compressive nature. The high deformations may lead to dislocations piling up at imperfections until small voids are formed [25]. Connection between several voids will form a crack and the repeated loading will promote growth. As illustrated in Figure 2.17 this may either reach the surface itself or encounter a crack generated there, to produce de-lamination or chipping [22].

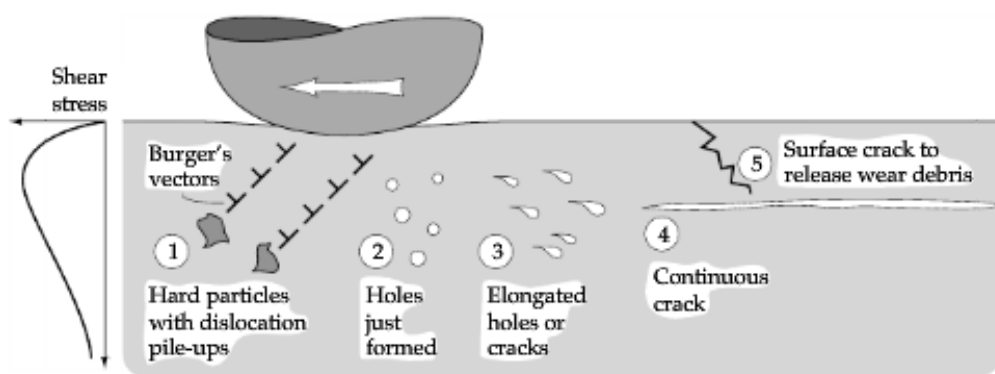


Figure 2.17: Deformation layer illustration [22].

Current de-lamination theory does not account for increase in temperature due to friction. It is believed that surface parallel cracks may block heat transfer from friction, leading to a higher temperature in the top layer. This heating may lead to tempering which will be discussed in Section 2.3.4.

Rolling

Local contact stresses are very high during rolling. The repetitive load cycle may cause fatigue and crack propagation. In addition, any oxides formed on the surface will be crushed under the high pressure. Illustrations of these cases are shown in Figure 2.18.

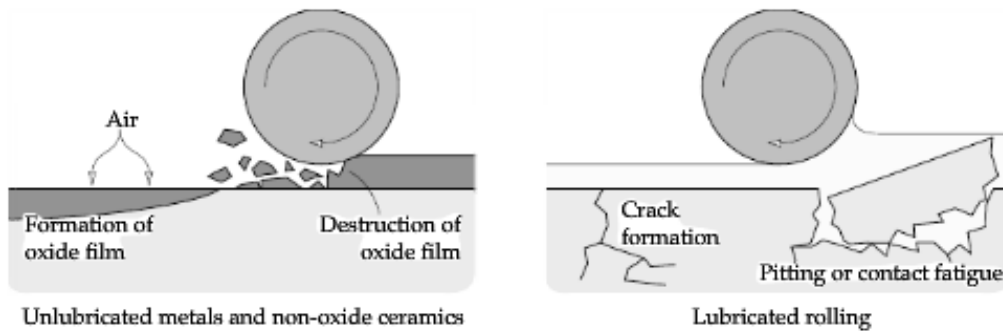


Figure 2.18: Wear mechanisms in rolling contact. Adapted from [22].

As with sub-surface initiated cracks in sliding mode, material properties are decisive to crack initiation during rolling [22]. Cracks may form at inclusions or imperfections by dislocation pileup [21]. De-lamination by sub-surface crack formation results in deep pits with straight edges and few cracks visible at the surface. The opposite is true for surface initiated cracking, where multiple cracks are visible around the shallow pits. The edges will be rounded off due to deformation during crack growth [22].

The rolling motion is often not perfect when a wheel moves on a surface. This shortcoming introduces a sliding component in the system. As mentioned in Section 2.4.1, the surface layer may sustain severe plastic deformation during sliding. The new lamellar structure makes crack propagation along the cell boundaries possible, as illustrated in Figure 2.19 [26].

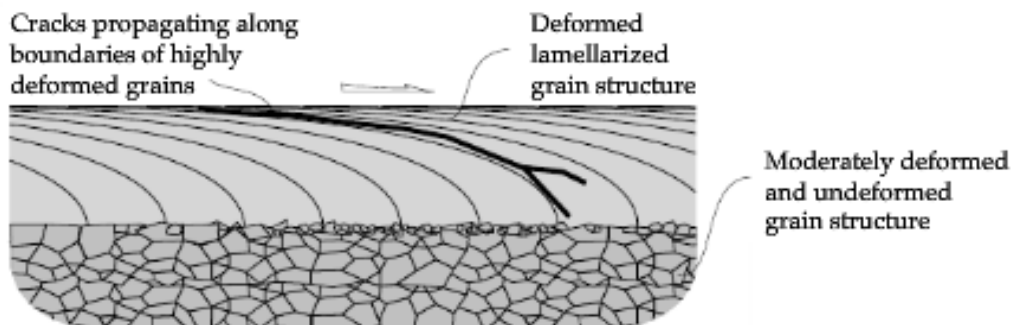


Figure 2.19: Lateral crack growth in lamellar surface layer [22].

Softer material may be plastically deformed during sliding. This effect in cutter discs is termed mushrooming as the cross section obtains a mushroom-like profile [4].

The plastic deformation will not by itself lead to material loss, but will create a larger contact area for the cutter discs, leading to reduced cutting efficiency.

2.4.3 Heat Generation

Most of the energy expended in plastic deformation is converted to heat [27]. The temperature increase is closely connected to the strain rate of the deformation. A high rate will produce a large local temperature increase [27]. It will also affect heat conductivity of the material. If the deformation rate is sufficiently high (approximately 10/s), the process may be termed adiabatic, with virtually no heat conducted away from the deformed area. This will lead to very high local temperatures [28].

Contact between asperities will also generate heat from friction. Since the true contact area between opposing asperities is always considerably smaller than the apparent contact area, the friction energy and resulting heat at these contacts becomes highly concentrated, as illustrated in Figure 2.20 [22]. These local zones of high temperature will experience a different thermal expansion than the surrounding material, leading to a physical elevation of the heated area [22]. The material response to elevated temperature differs, but as a general rule, wear resistance is reduced by increasing temperature.

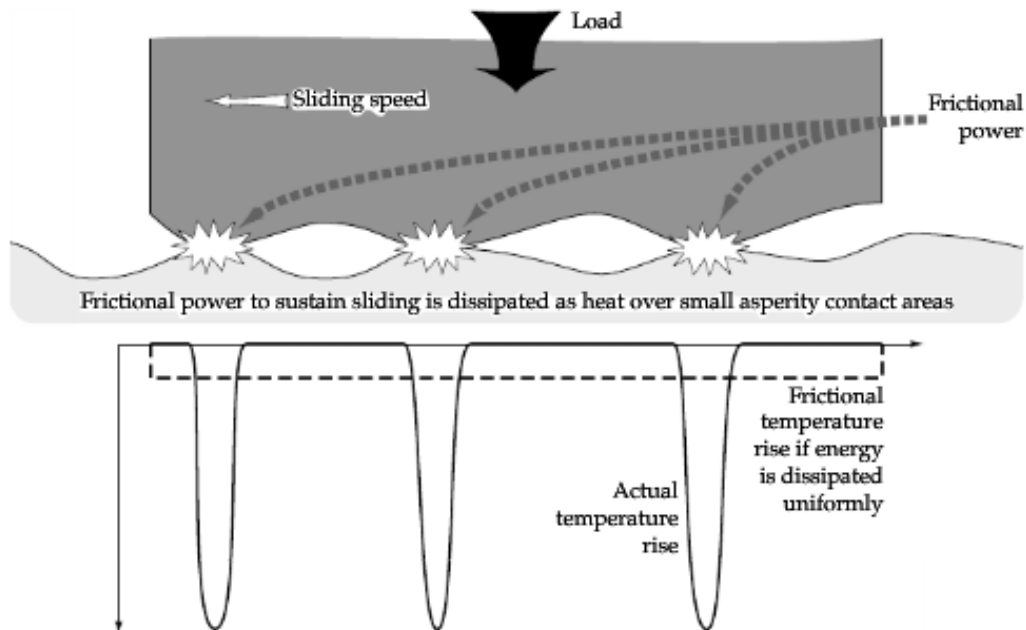


Figure 2.20: Local and global heating due to friction [22].

2.5 Rock Abrasivity and Cutter Wear

2.5.1 Rock Abrasivity Test Methods - State of the Art

Commonly, many different layers of rock are encountered during a single tunnelling project. It is therefore important to investigate in what way different types of rock influence the cutter tool consumption. There are several accepted and commonly used test methods for estimations of rock abrasiveness of cutter discs. The CERCHAR Abrasivity Index (CAI), LCPC Abrasivity Coefficient (LAC) and the Abrasion Value Cutter Steel (AVS) all quantify the total abrasive wear on steel by various rock types [29,30].

The CERCHAR apparatus, imaged in Figure 2.21, was originally developed and introduced in the 1980s. A steel stylus is pressed against a rock specimen firmly held by the test apparatus. While loaded with a normal force of 70 N, the stylus is moved a total distance of 10 mm across the rock. The duration of the stylus movement should be held within 1 ± 0.5 s with the original apparatus and 10 ± 2 s with the modified design. Wear is measured on the tip of a steel stylus of Rockwell hardness, type C, HRC 55.

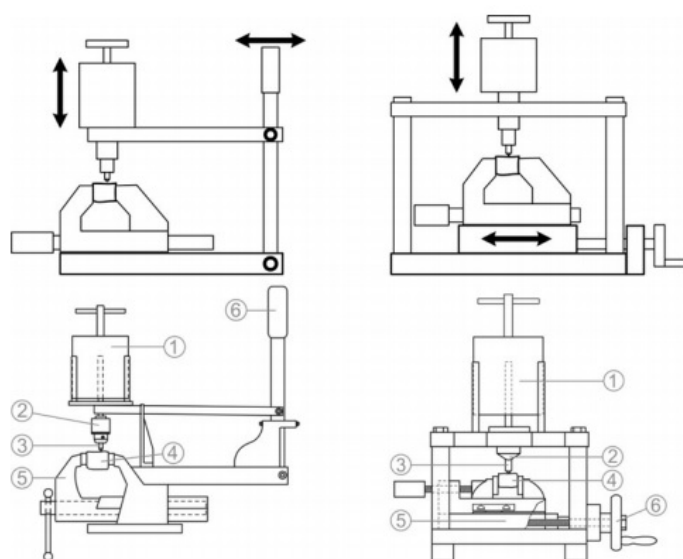


Figure 2.21: Two main types of CERCHAR test apparatus commonly used. Left hand setup, original design. Right hand setup, modified design, as reported by West [31]. 1 = mass, 2 = pin chuck/guide, 3 = stylus, 4 = specimen, 5 = vice, 6 = lever/hand crank [32]

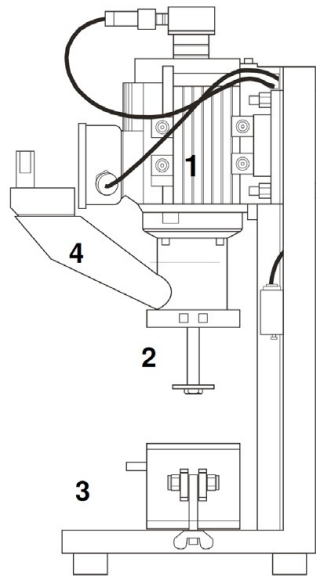


Figure 2.22: LCPC abrasivity testing device according the French standard P18-579 (1990). 1 = motor, 2 = steel impeller, 3 = sample container, 4 = funnel tube [33].

An outline of the test apparatus used in LCPC testing is shown in Figure 2.22. The impeller, a rectangular plate, is made of standardized steel with Rockwell hardness, type B, HRB 60-75. It rotates for a duration of 5 minutes at a speed of 4,500 rpm in the sample container. The container is filled with 500 ± 2 g crushed, sieved and air dried sample material of fraction 4-6.3 mm. Weight loss of the impeller is used to quantify the rock abrasivity.

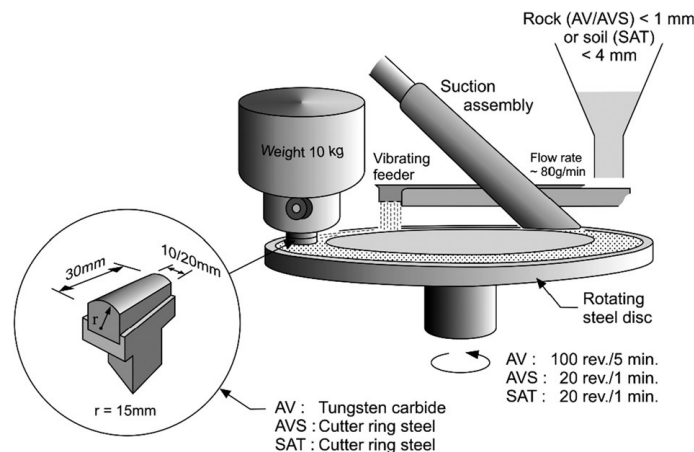


Figure 2.23: Outline of the Abrasion Value (AV) and Abrasion Value cutter Steel (AVS) test [34]

AVS measures the ability of a rock to induce wear on cutter ring steel. The measurement is time dependent and use finely crushed rock powder as abrasive medium. A test setup with parameters for the AVS test is shown in Figure 2.23. The weight loss of the sample is measured after 1 minute (at 20 rpm) and compared with measurements of 2621 recorded values in the NTNU/Sintef database [34]. Values range from 0.0 (limestone) to 68.5 (quartzite)

Table 2.3: AVS classification of rock abrasion [34].

AVS (mg)	Abrasion on cutter steel
≥ 44.0	Extremely high
36.0-44.0	Very high
26.0-43.9	High
13.0-25.9	Medium
4.0-12.9	Low
1.1-3.9	Very low
≤ 1.0	Extremely low

Heterogeneity in the rock mass, uneven movements of the cutter head and even the breaking of rocks result in significant variations in disc load. This may be shown in Figure 2.24 [35]. The TBM used for the measurements provided in Figure 2.24 had a diameter of 9.93 m and about 80 17" diameter cutter discs. The total thrust was about 8 MN, cutter head torque about 1.3 MNm. Its average rotational speed was about 2.3 rev/min with a penetration of 3.5 mm/rev. The peak and average force measured was 820 and 85 kN respectively for the outer cutter, 900 and 110 kN for the middle cutter and 720 and 210 kN for the inner cutter [35]. There is currently no practicable procedure to reproduce the complex force variation experienced by the cutter discs in affordable small scale lab tests. To simplify, all the above mentioned models focus on the abrasive aspect of the wear prediction. This will reduce the direct correlation between laboratory testing and real operations as it removes most of the wear by chipping.

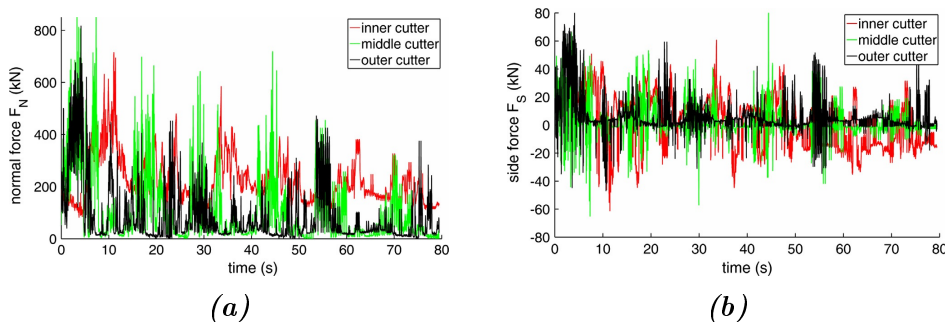


Figure 2.24: a) Normal force F_N on cutters plotted against time [35]. b) Side force F_S on cutters plotted against time [35].

2.5.2 Rolling Indentation Abrasion Test (RIAT) Method

Two of the most apparent weaknesses with the tests mentioned in 2.5.1 when used to predict wear in hard rock TBMs are the contact mode utilized and thus the wear mechanisms these modes reproduce. When ruling out chipping caused by knocks and fatigue, cutter disc wear is dominated by two-body abrasion. Soil grinding the metal sample, as tested with AVS, will produce wear by three-body abrasion. As mentioned in section 2.4.1, this wear mechanism is around ten times less efficient than two-body abrasion. The CERCHAR and LCPC tests initiate wear by two-body abrasion. In all three methods, the contact mode will be only sliding. During production, a combination of rolling and sliding will occur, with rolling as the dominant mode of contact. Had this not been the case, disc wear would have been significantly higher [4]. In order to overcome these challenges a novel characterization method for rock abrasiveness is currently under development at NTNU [36]. This method, called the Rolling Indentation Abrasion Test (RIAT), utilize mini cutter discs for wear measurements on hard rock samples in a rolling-sliding motion. Following this design, the discs are worn by two-body abrasion in what is assumed to be a predominantly rolling contact. The test configuration is seen in Figure 2.25 [37]. Preliminary results from the analysis of the RIAT discs are presented in this thesis.

The RIAT uses a tool fitted with two replaceable miniature cutter discs, mini-cutters, to measure rock abrasiveness. The tool is pressed onto a polished rock sample while rotating, simulating the load and movement of real cutters on a TBM. The discs are 30 mm in diameter and the contact zone is 4 mm wide. A sustainable drive provides a thrust of 1250 N to the tool while rotating at 40 rpm for 30 minutes.

Even though the values of load in RIAT deviate from those mentioned in Section 2.5.1, they have been chosen to simulate real cutter parameters in hard rock TBMs [37]. Though seemingly significant, this deviation may provide only a negligible error. According to [5] and [38] wear of a cutter disc is proportional its rolling distance. Regression analysis has shown a close correlation ($R^2 > 90\%$) between rolling distance and radial wear for all face and gage cutters. By contrast, no correlation of wear and contact force of the disc has been published so far [29]. This may strengthen the weight of potential results despite process parameters in early development.

Disc weight loss as well as penetration depth is measured to characterize the tool wear and effectiveness of cutting in different rock types. In addition to being a measurement for cutter disc lifetime, the test provides valuable insight into wear and penetration from varying operational parameters. Changes in the given parameters may occur as the method is currently under development.



Figure 2.25: The RIAT tool and the mini-cutter rings [37].

2.5.3 Rock Type and Wear

Several properties of rocks affect their ability to initiate abrasive wear in steel. A study on wear on martensitic steels by different rock types indicated that rock properties such as uniaxial compressive strength (UCS) was strongly correlated with wear rates [39]. High UCS rock produced wear by ploughing and cutting, whereas rocks with intermediate UCS properties caused a mix of formation grooves and plastic deformation. Low UCS rock types caused large amounts of debris embedment, resulting in low wear rates. Steel hardness was less important for the wear rates of rocks with lower UCS values [39].

Preliminary results from the RIAT testing show wear rates from four different rock types; basalt, granite, limestone and quartzite. These are shown in Figure 2.26. Quartzite is found to be the most abrasive rock type of the four, with granite, basalt and limestone following in falling order of abrasivity [37]. A recent study also performed wear measurements on granite and quartzite, finding higher rates of wear in granite than quartzite. No clear correlation between UCS and wear rates were reported, as the highest UCS valued rock generated was the least abrasive [40]. As this study will analyse RIAT test mini-cutters, quartzite will be defined as the most abrasive of the rock types used.

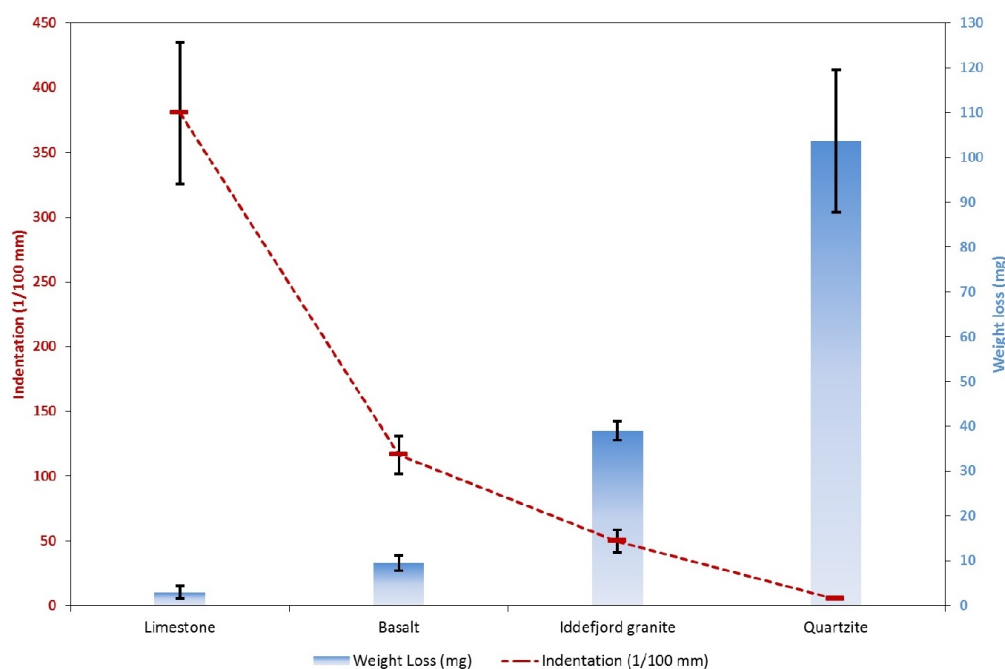


Figure 2.26: Preliminary wear results presented from RIAT testing. Error bars show standard deviation [37].

Chapter 3

Experimental

3.1 Samples

Two types of samples were analysed in this master's thesis; RIAT mini-cutters and discs from a full scale tunnelling project in Røssåga, Norway.

The TBM used in Røssåga is called "Jern Erna" and shown in Figure 3.1. It is 7.23 m in diameter and will drill in total 7 km of tunnel as part of a hydro power plant for Statkraft [41]. Its cutter head houses 46 19" [48.3 cm] diameter discs.



Figure 3.1: The TBM used in Røssåga. Photo provided by The Robbins Company [41].

The samples collected from Røssåga are all used discs which were replaced due to excessive wear. The position on the cutter head, run time and geology were mapped in addition to dominating wear mechanism. Microstructure and hardness has been studied. The exact production method for the TBM samples is unknown, but it is

assumed that they are forged, as this provides a strong material with as few defects as practicable. Probable composition for the discs is shown in Table 3.1.

Table 3.1: Probable composition of the samples from Røssåga [42].

C [wt%]	Mn [wt%]	Si [wt%]	Cr [wt%]
0.57	0.29	0.98	4.84
V [wt%]	Mo [wt%]	Ni [wt%]	Cu [wt%]
0.92	1.35	0.12	0.12

The RIAT mini-cutters are 30 mm in diameter with a tip width of 4 mm. The distance between the two mini-cutters when placed in the tool is 60 mm. A thrust of 1250 N is provided to the tool while rotating at 40 rpm for 30 minutes. Mini-cutter weight loss and rock penetration depth is measured during testing. The mini-cutters were later examined for hardness, microstructure and deformation structure. The samples are made by H13 tool steel of composition given in table 3.2 [43]. They were machined and pre heated at 700 °C prior to annealing at 1020 °C. Tempering was performed twice for 2 hours at 600 °C.

Table 3.2: Composition of the H13 tool steel used in the RIAT samples [43].

C [wt%]	Mn [wt%]	Si [wt%]	Cr [wt%]	V [wt%]	Mo [wt%]
0.39	0.4	1	5.2	0.9	1.4



Figure 3.2: a) 19" samples from Røssåga. b) H13 mini-cutters for small scale testing.

The samples collected from Røssåga and a RIAT mini-cutter are shown in Figure 3.2a and Figure 3.2b respectively. Table 3.3 gives an overview of the different samples and the tests which were performed on them.

Table 3.3: Overview of the different samples and tests performed on each sample. A box marked "x" implies "performed". Boxes marked "-" imply "not performed".

Sample ID	Sample type	Geology	Hardness	Microstructure	FIB	Tempering
140	TBM cutter	Røssåga	x	x	x	-
302	TBM cutter	Røssåga	x	x	x	-
314	TBM cutter	Røssåga	x	x	x	-
383	TBM cutter	Røssåga	x	x	x	-
HD4	TBM cutter	Unused/new	x	x	-	x
001 & 002	RIAT mini-cutter	Basalt, China	-	x	x	-
003 & 004	RIAT mini-cutter	Granite	-	x	x	-
1, 2, 3 & 6	RIAT mini-cutter	Granite, Iddefjord	x	x	x	-
4, 8 & 11	RIAT mini-cutter	Quartzite	-	x	x	-

3.2 Metallography

3.2.1 Sample Preparation

A large bandsaw with a WC grit blade was used to cut sample slices from the discs. The band was water cooled and the temperature resulting in the discs were said to be below 25 °C. The slices were then cut to smaller samples by a water cooled *Discotom-2* saw using a *Struers 60A25* circular blade. The two saws effect on steel microstructure is depicted in Figure 3.3. A bright zone in the material cut by the bandsaw is observed in Figure 3.3b. The zone is assumed to be deformed material, as the WC-cutters of the bandsaw gnaw through the material. The extent of this deformation is not mapped, but the surfaces studied were all cut by the *Discotom-2* saw.

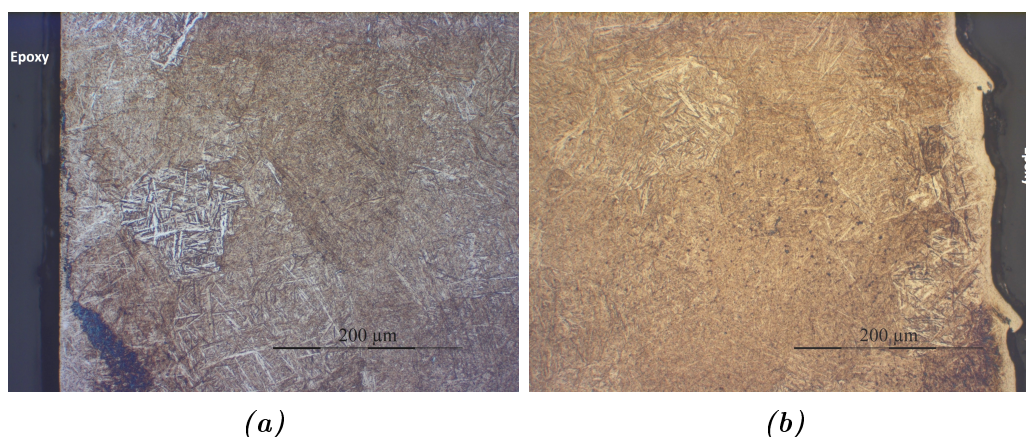


Figure 3.3: **a)** Microstructure of sample 314, left edge cut with *Discotom-2*. Etched with *Vilella's* reagent. 200X magnification. **b)** Sample 314, edge on right side cut with bandsaw. Etched with *Vilella's* reagent. 200X magnification.

To obtain optimal shape for preparation procedures the samples were embedded in the two component epoxy mixture *EpofixTM*. The diameter of the samples were 30 mm after embedment. Following embedment, the specimen were grinded and polished until a maximum roughness of 1 μm was obtained.

3.2.2 Etching

As part of sample preparation for optical microscopy, different etching processes were used depending on the inherent alloying elements. The etchants used in this project are listed in Table 3.4 with further explanations of functionality given below.

Vilella's etchant gave very good contrast between martensite and retained austenite. Unfortunately its use is prohibited at NTNU. It was therefore used only as a base of comparison to test the quality and effect of other potential etchants. Images etched with *Vilella's* etchant are seen in Figure 3.3.

Table 3.4: Etchants used for optical microscopy imaging.

Name	Content	Effect
Vilella's reagent	5 ml HCl (37 %) 1 g picric acid 100 ml ethanol	Martensite is colored. Ferrite, retained austenite and carbides unaffected.
Kalling's no. 2	50 ml HCl (37 %) 50 ml ethanol 2 g CuCl ₂	Martensite turns dark. Ferrite, retained austenite and carbides unaffected.
Marble's reagent	5 g CuSO ₄ 50 ml HCl 50 ml water	Martensite turns dark. Ferrite, retained austenite and carbides unaffected.

Kalling's no. 2 gave results similar to that of Vilella's etchant far from the edges of the sample. An optical image of microstructure produced by this etchant is found in Figure 2.7. During sample preparation, cracks easily formed in the interface between sample and epoxy. The high chloride concentration led to crevice corrosion in these areas, rendering the edges severely corroded. Kalling's etchant was therefore not used further, but is mentioned as an option for other examinations.

Marble's reagent gave results similar to that of Vilella's etchant. This etchant is designed to show microstructure in Ni-alloys and super alloys. Some edge distortion was seen, but accounted for by short etching times and modified concentration of active components of the etchant. The etchant used therefore has a reduced CuSO₄ content compared to original recipes.

3.2.3 Microscopes

The optical microscope *Leica MEF4M* shown in Figure 3.4 was used for microstructure imaging. Lenses with 20X, 50X and 100X magnification were used. Magnification of the ocular lens on the digital camera is 10X, providing images of 200X, 500X and 1000X magnification respectively.

A *Zeiss Ultra 55 Limited Edition* scanning electron microscope (SEM) was used for surface imaging. As the electron beam penetrates the sample, electrons from atoms in the outer most surface layer are excited. These are called secondary electrons and may be used for surface imaging. An Everhart-Thornley detector was used to observe topography through the secondary electron signal. Low current mode was used to give better contrast and an aperture of 20 μm gave good depth of field. Elastically reflected, backscattered, electrons (BSE) were detected by a backscatter electron detector. These images provide poor topography contrast in comparison to secondary electrons, but indicate which atoms were responsible for the reflection by atomic number, Z-contrast. Heavy atoms reflect more electrons than lighter atoms and appear as bright areas in the image [44].

As the SEM was used for wear surface imaging, no grinding or polishing was

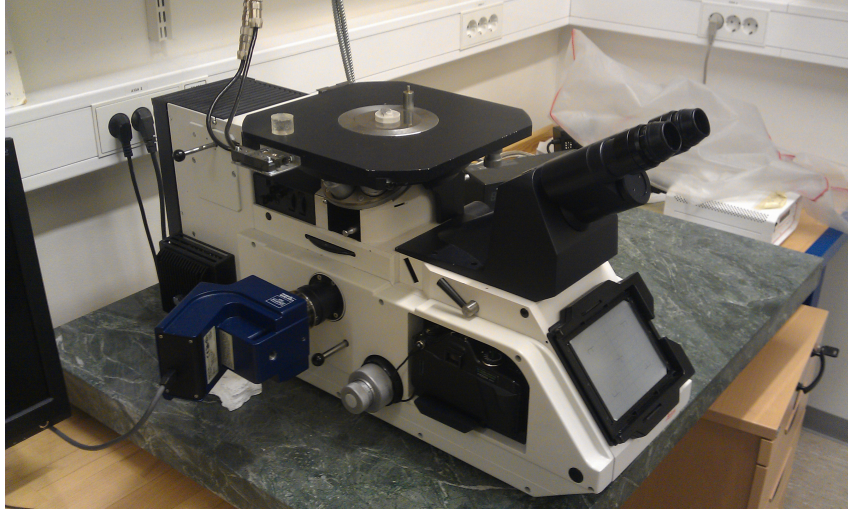


Figure 3.4: Leica MEF4 optical microscope

needed. The samples were cut and cleaned prior to ultrasonic bathing in acetone. Each sample received a bath time of 5 minutes. This removed dust and organic material as well as some embedded rock debris from the surface.

In Focused Ion Beam (FIB) microscopy, ions are used to manipulate and image the sample [45]. The use of ions enables surface manipulation by depositing or sputtering away material as well as imaging. In this project, the FIB was used to cut cross sections into the sample. The cross section was studied immediately after cutting without exposing it to air.

A *FEI Helios NanoLab DualBeam FIB* with a gallium source, shown in Figure 3.5a, was used. DualBeam indicates that in addition to a Ga-source, the FIB is equipped with an electron source, enabling ordinary SEM-imaging. Cross sectional cuts were made into the surface by way of Ga-ion milling and SEM imaging was used to study the nanocrystalline deformation layers in the samples by way of secondary electrons. A cross section milled by Ga-ions are shown in Figure 3.5b. Figure 3.5c shows the SEM image of a cross section. Samples prepared for FIB were cut with the *Discotom-2* and given a five minute ultrasonic bath in acetone. The different parameters used for milling are shown in Table 3.5. When imaging microstructure, the microscope brightness was set to a near 0 % value, with contrast set to near 100 %. Large amounts of rock were still present on the surface after the ultrasonic bath. The non-conductive rock caused charging during SEM imaging and the samples were therefore sputtered with gold for better conductivity and reduced image drift.

The effect of varying FIB-current is illustrated in Figure 3.6. The Ga-beam is cone shaped with a radius proportional to the current output. A large output gives a wide cone while a small current gives a narrow cone. To obtain adequate results the slope of the cross section should be as steep as possible. This is performed by finishing cleaning at a low current. Naturally, the efficiency of the milling is higher at larger current outputs. A compromise is made by milling stepwise, first with

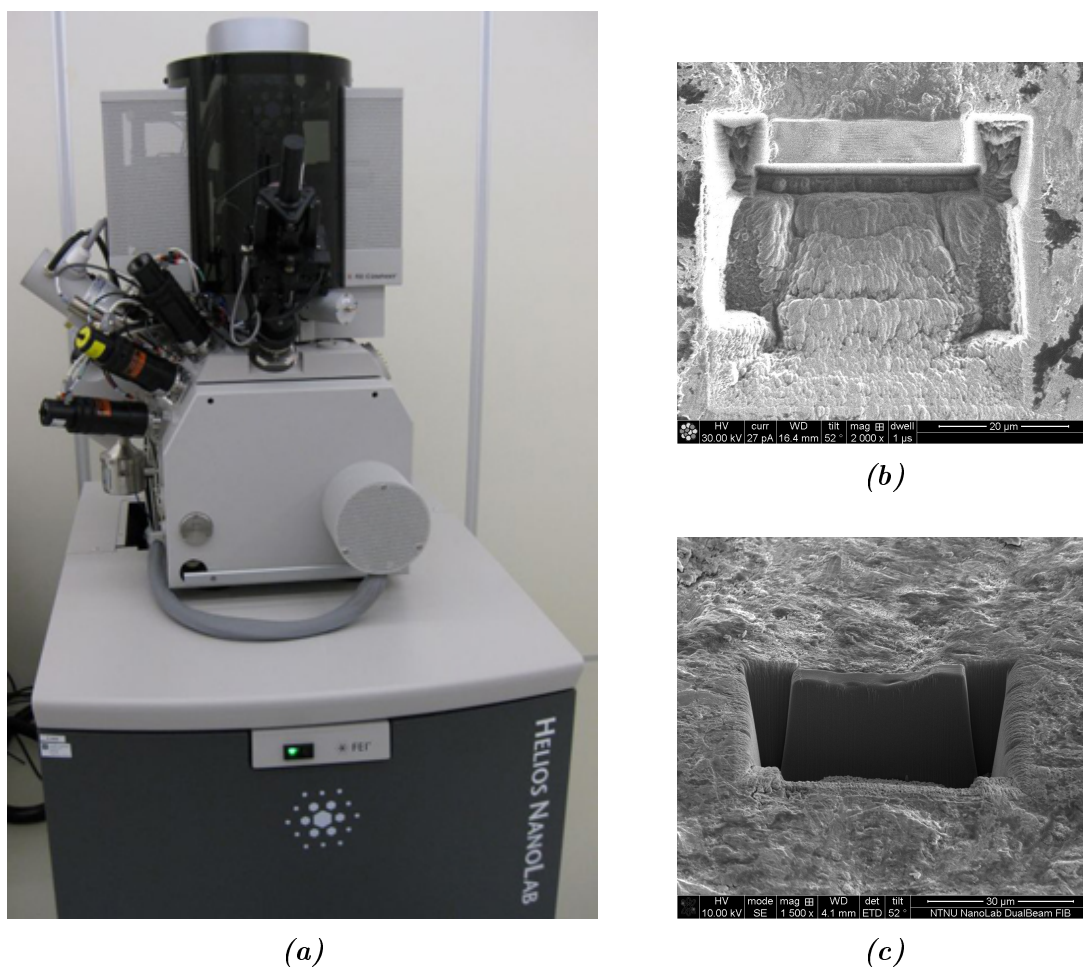


Figure 3.5: a) The FEI Helios NanoLab DualBeam FIB used for imaging [45]. b) FIB milling overview, gallium source image. c) FIB milling overview, electron source image.

a high current, with a gradual reduction to steepen the slope. The finishing step provides a steep and even cross section.

The microscope was also equipped with an Energy Dispersive Spectrometer (EDS). The EDS collects X-rays emitted from atoms in the sample to identify the elements present. Electrons at their ground state inhabit discrete energy levels in each atom. When struck by the electron beam, electrons are excited from these levels leaving "electron-holes". Electrons further away from the nucleus will drop to lower energy levels to fill the holes created, releasing the excess energy as X-rays. Each X-ray corresponds to a unique energy level and may therefore be used to identify the element it was emitted from [44]. Due to large margins of error, the amount of each element present is hard to measure with this technique. It was therefore only used to identify the elements present in particles found in the cross sections.

Table 3.5: Steps in FIB milling.

Step	Description	Current
Carbon deposition	Creates a surface layer of carbon for smoother cross section cuts.	21 nA
Rough cuts	Deep rough cuts to expose cross section for further study. Deep trenches on either side of the carbon layer helps offload removed atoms. Too small rough cut will lead to shadowing.	21 nA
1st cleaning cut	Cuts into carbon layer to straighten out the profile of the cross section.	6.5 nA
2nd cleaning cut	Finalize the cross section by further straightening of the cross section. Stripes and cuts in the surface are removed.	0.92 nA

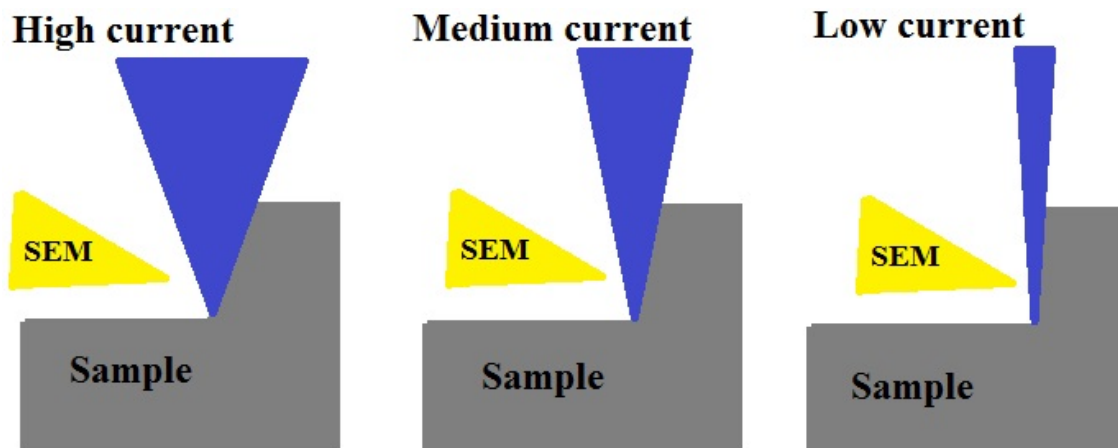


Figure 3.6: FIB milling steps. Effect of varying FIB-current intensity. Blue beam illustrates the ion-beam of the FIB. The yellow beam illustrates the electron beam of the SEM

3.3 Tempering

A tempering experiment was performed to identify the evolution of hardness as a function of time and temperature, without including deformation. Samples were cut from the unused disc, HD4. Tempering was performed at 200, 300, 400, 500, 600 and 700 °C. Three samples were used at each temperature, tempered for 1, 2 and 4 hours respectively. The furnace used was the Nabertherm N17 which is shown in Figure 3.7. No attempts were made to control the atmosphere inside the furnace. The effect of this is decarburization due to lower carbon concentration in the air than in the steel. This is also true during normal TBM operations and is therefore seen as a natural part of the experiment.



Figure 3.7: The Nabertherm N 17 furnace used for specimen tempering.

Each sample was air cooled prior to examination. The effect of tempering was quantified by hardness measurements. This process is further explained in the next section.

3.4 Hardness Measurements

The *Matsuzawa Seiki-DVK-1S* hardness indenter shown in Figure 3.8a was used to perform macro hardness measurements. All measurements on the Matsuzawa were performed at 5 kg_F (kilogram-force), providing results in HV5. For hardness profiles, each distance from the surface was indented three times on a parallel line, and the average value was used. Digital position measurement of the optical microscope specimen stage was used to measure the distance from the surface edge to the indentations. The sample image shown in Figure 3.8b shows the indentation marks.

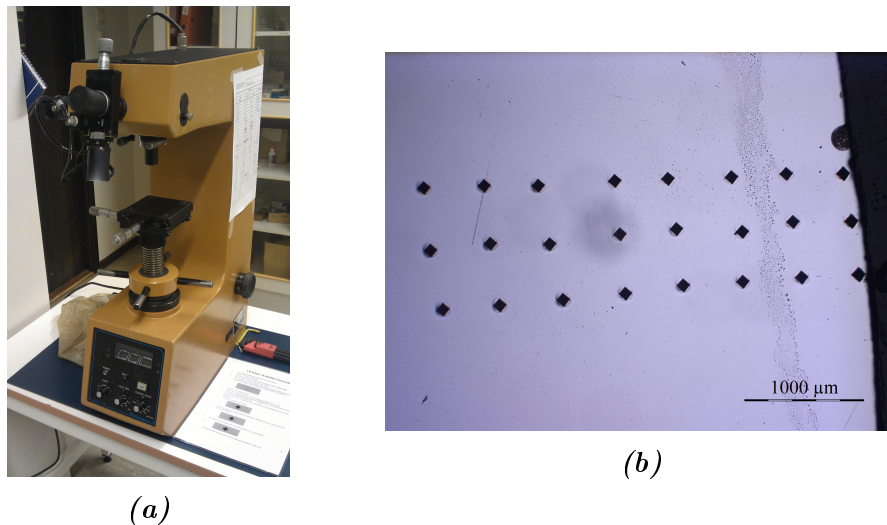


Figure 3.8: a) *Matsuzawa hardness indenter.* b) *Hardness indentations on sample 383. (25X)*



Figure 3.9: *Micro hardness indenter*

For hardness measurements after tempering, each sample was given ten indents and the average value used.

The *Leica VMHT MOT* micro hardness indenter shown in Figure 3.9 was used to measure hardness profiles of a RIAT mini-cutter. The process was similar to that described above and shown in Figure 3.8b, but for the distance from indentation to surface. This was registered manually by way of moving the specimen stage a known distance for each measurement. The measurements were performed with 0.025 kg_F, providing results in HV0.025

Chapter 4

Results

All laboratory work was conducted in accordance with the risk assessment presented in Appendix B.

4.1 Field Data from Røssåga

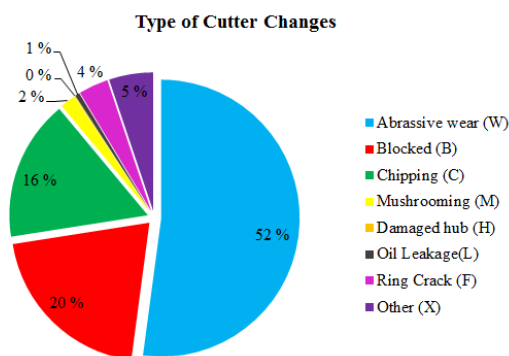


Figure 4.1: Overview of wear mechanisms on the Røssåga TBM.

Figure 4.1 shows an overview of the different wear mechanisms recorded to cause cutter refurbishing or replacement during production from October 2014 to April 2015. The reasons for change are based on the Bruland methodology [5]. The dominating wear mechanism observed in situ is abrasion (52 %), followed by blocked discs (20 %) and chipping (16 %). A detailed graph showing the cutter consumption, with reasons for change, at different cutter head positions is shown in Figure 4.2. As indicated, the disc position has a large im-

act on disc lifetime. An increase in cutter consumption is noted with increasing distance from cutter head centre (position 1). Increased distance from centre imply an increase in rolling distance during cutter life. An illustration of cutter positions relative to centre is shown in Figure 4.3. A more detailed sketch is found in Appendix C.

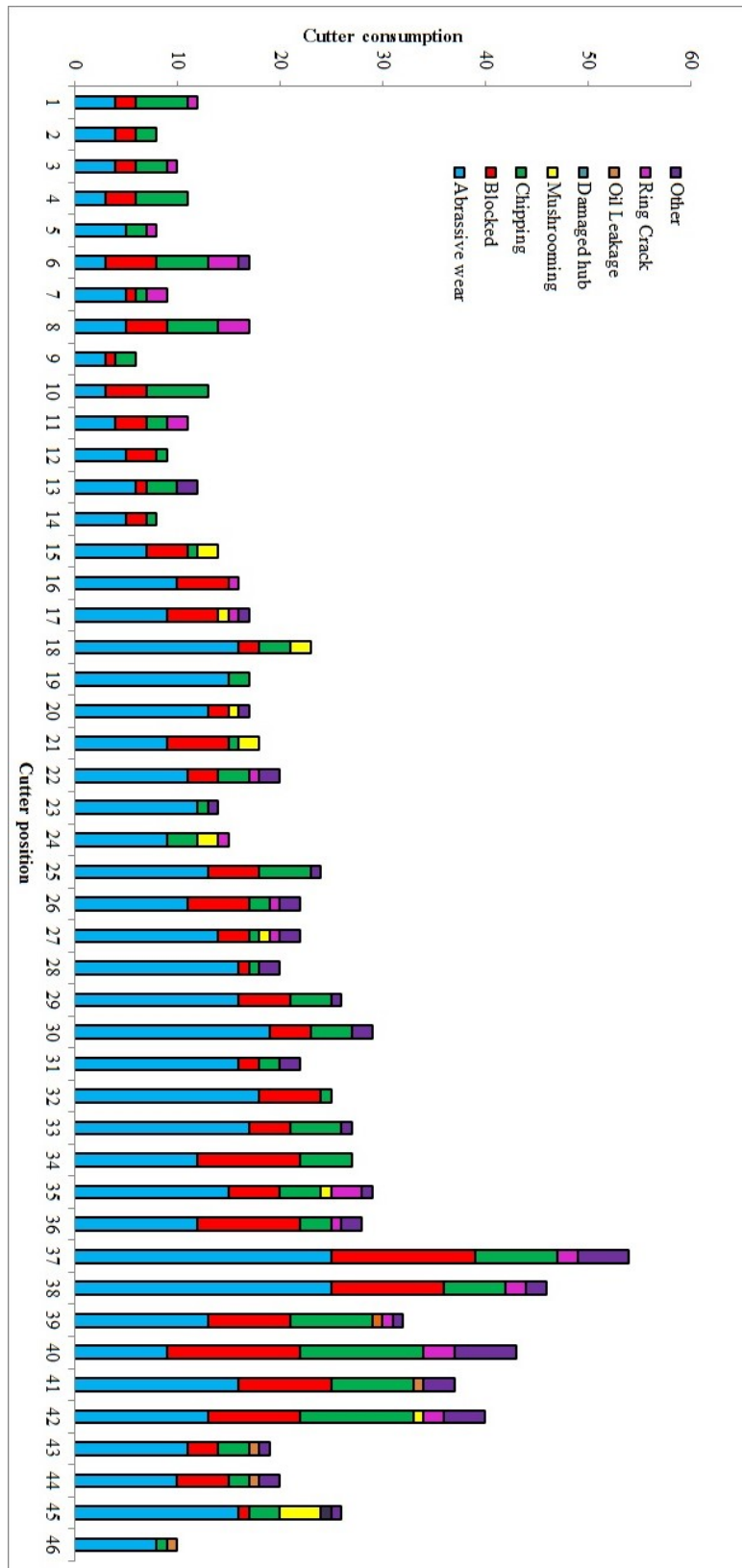


Figure 4.2: Reasons for cutter changes on all cutter head positions.

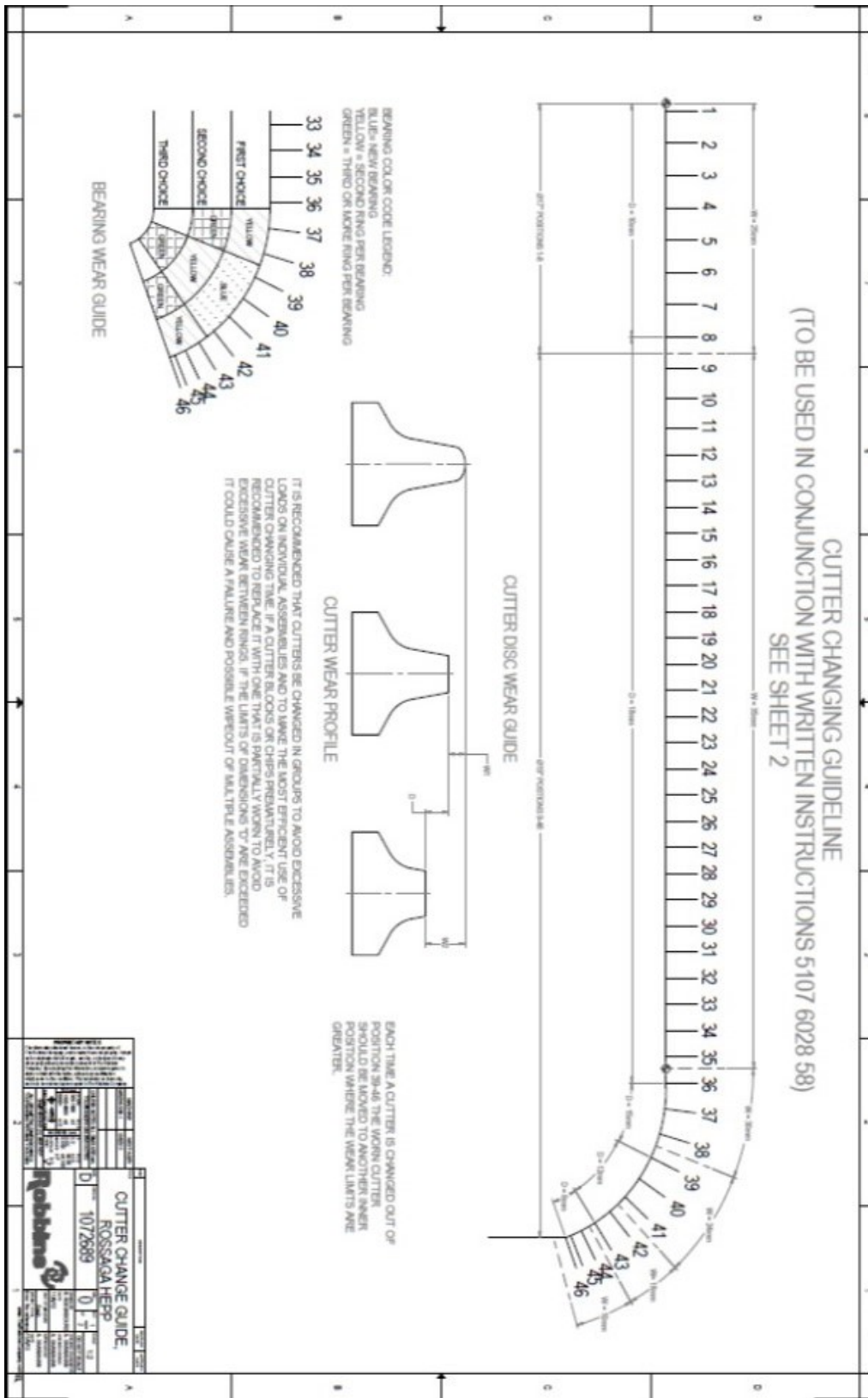


Figure 4.3: Overview of cutter positions from cutter head center.

Cutter 140 is used at similar distances at positions 41 and 39. These have comparable exchange rates and wear types, dominated by abrasive wear, chipping and blocked discs. The relatively high amount of cutters replaced by chipping indicate large fluctuations in load, as this is a fatigue initiated wear mechanism. Blocked discs are often caused by damaged cutter bearings. This type of wear indicate frequent, hard knocks causing bearing damage and eventual blocking of the rolling motion.

Cutter 302 is used in position 30 for its entire lifespan. Cutter changes are predominantly caused by abrasive wear, with small amounts of chipping and blockage.

Cutter 314 served a short stint (39.6 km) at position 43 prior to serving the remainder of its lifetime (595.2 km) at position 23. Both areas experience relatively few cutter changes. Abrasive wear is the dominant reason for change, with negligible amounts of chipping and blockage also noted.

Cutter 383 served approximately half its lifespan (175.7 km) at position 45 prior to a move to position 42, where it was replaced after 120.7 km. A notable difference in reasons for change is noted. Abrasive wear prominent in position 45, whereas chipping and blockage occur an approximate equal amount of times as abrasion in position 42.

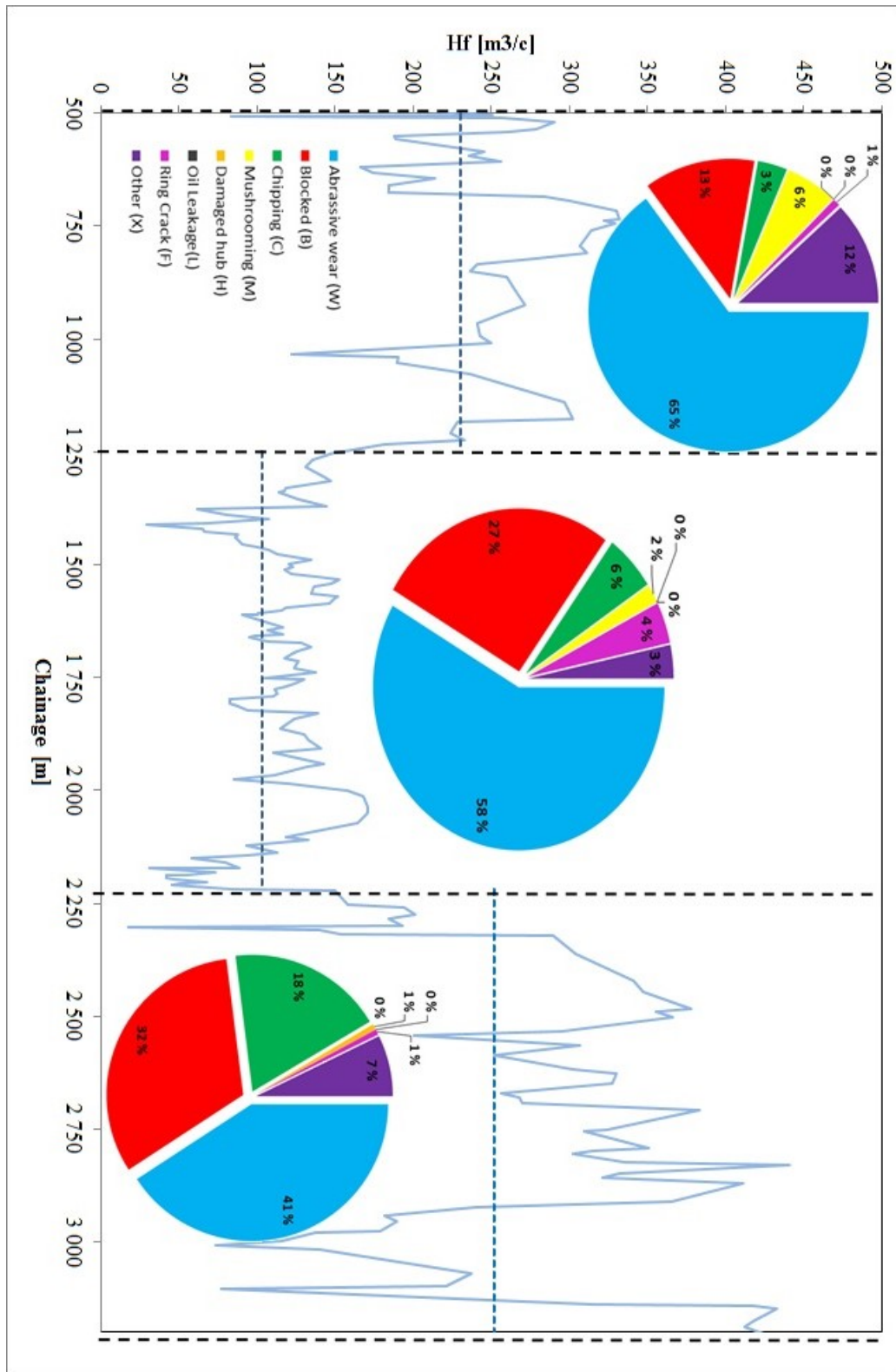


Figure 4.4: Cubic meters of rock per cutter versus tunnel progress, chainage, on TBM at Røssåga.

Geology is also very important to cutter lifetime, as seen in Figure 4.4. Three main regions are seen, with the possibility of a fourth region starting as the measurements end. A delay in the cutter life values should be noted. This arise as cutters from highly abrasive rock areas are replaced well after passing into a softer layer, but ahead of new cutters would have been in the same rock. The TBM cutters analysed in this thesis were collected from chainage 2171 (314 and 302) and 3189 (140 and 383), i.e. at the end of the highly abrasive region two (middle) and the less abrasive region three (bottom). Differences in wear causing cutter replacements are seen. While Abrasive wear dominates all regions, chipping increase three times in influence as cutter life is almost tripled between sections 2 and 3.

Results from rock testing performed at rocks positioned in section two (chainage 1200-1930) of Figure 4.4 show AVS in the regime of 28.5 to 33.0, with sub-classification "high". Only two such results are available for rock from what may be called section three. The measurements are taken at chainage 2105 and 2175, with AVS 1.0, sub-category "Extremely low" and 3.5, sub-category "Very low", respectively. A lower lifetime for cutters 302 and 314, relative to 140 and 383, would therefore be expected.

Table 4.1: TBM cutter log

Cutter ID	Start position	Rolling distance [km]	2nd position	Rolling distance [km]	Replaced at chainage [m]
140	41	172	39	119.7	3189
302	30	620.2	na	na	2171
314	43	39.6	23	595.2	2171
383	45	175.7	42	120.7	3189

A detailed overview of the operational life of the cutters analysed are given Table 4.1 and in Figure 4.5. From Figure 4.5, cutters 140 and 383 are seen to have a linear wear progression in the same area. Cutters 314 and 302 experience significant use without wear in the same area. Measuring errors are seen by the fact that wear seems to be reduced at certain measurements. From Table 4.1, it is noted that cutters 302 and 314 obtained a rolling distance in excess of 600 km each. This is twice as high as the cutters used in the less abrasive area. No explanation for this deviation was found in the cutter records.

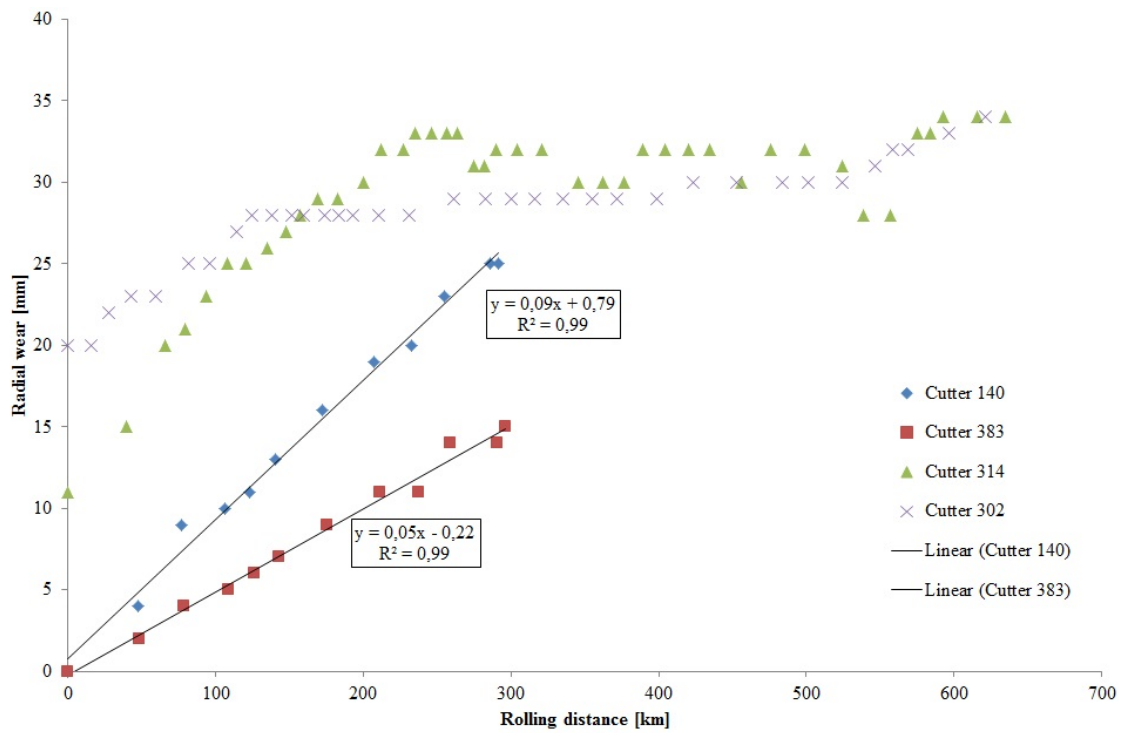


Figure 4.5: Cubic meters of rock per cutter versus tunnel progress, chainage, on TBM at Røssåga.

The gradient of cutter 314 when actually worn is compared with that of cutter 140 and 383 in Figure 4.6. An identical wear rate to cutter 140 is seen. The wear rate recorded on cutter 383 is approximately half of what is registered in disc 140, despite used in the same rock type. This difference further illustrate the dependency of position in cutter life.

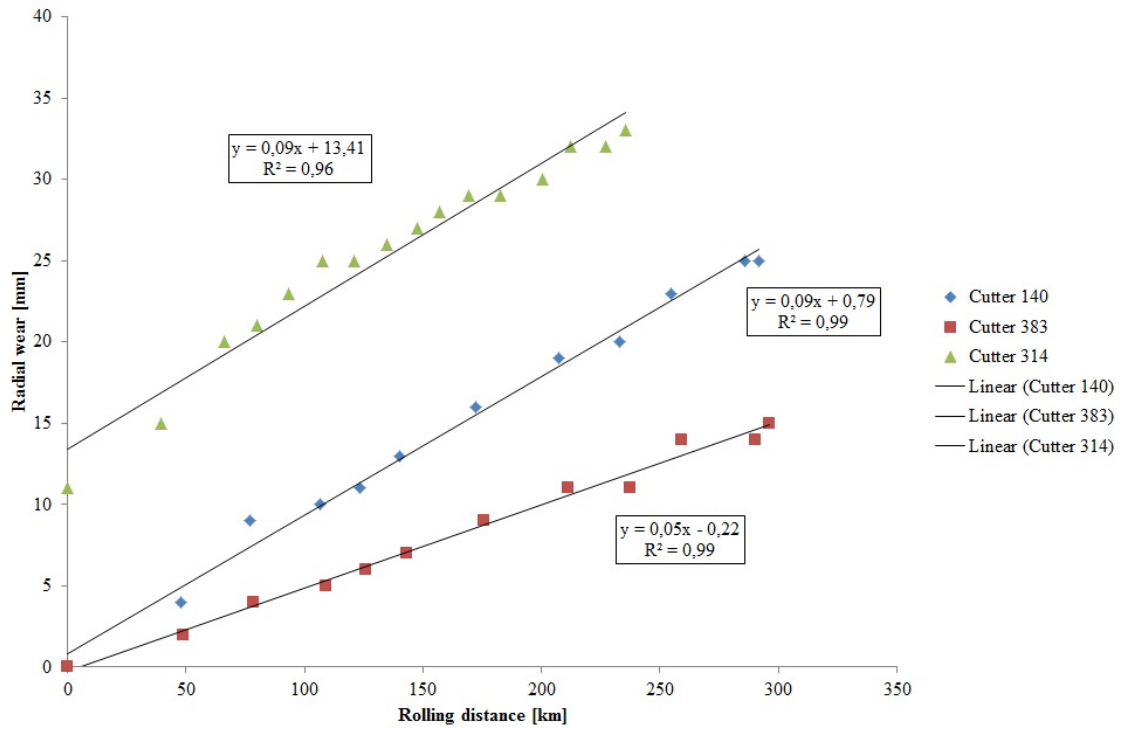


Figure 4.6: Cubic meters of rock per cutter versus tunnel progress, chainage, on TBM. Linear comparison.

4.2 Failure Mechanism Examination

Both optical- and electron microscopical examinations were performed to identify different aspects of the failure mechanisms in the TBM cutter discs and RIAT mini-cutters. The results from these examinations are presented in the following sections.

4.2.1 Modes of Contact

Cross sections were made parallel to the direction of rolling. This was done to study the modes of contact experienced by the TBM cutters and RIAT mini-cutters during operations. Lamellar structures at the surface are caused by a sliding contact mode. The depth of this layer indicate the dominance of sliding versus rolling.

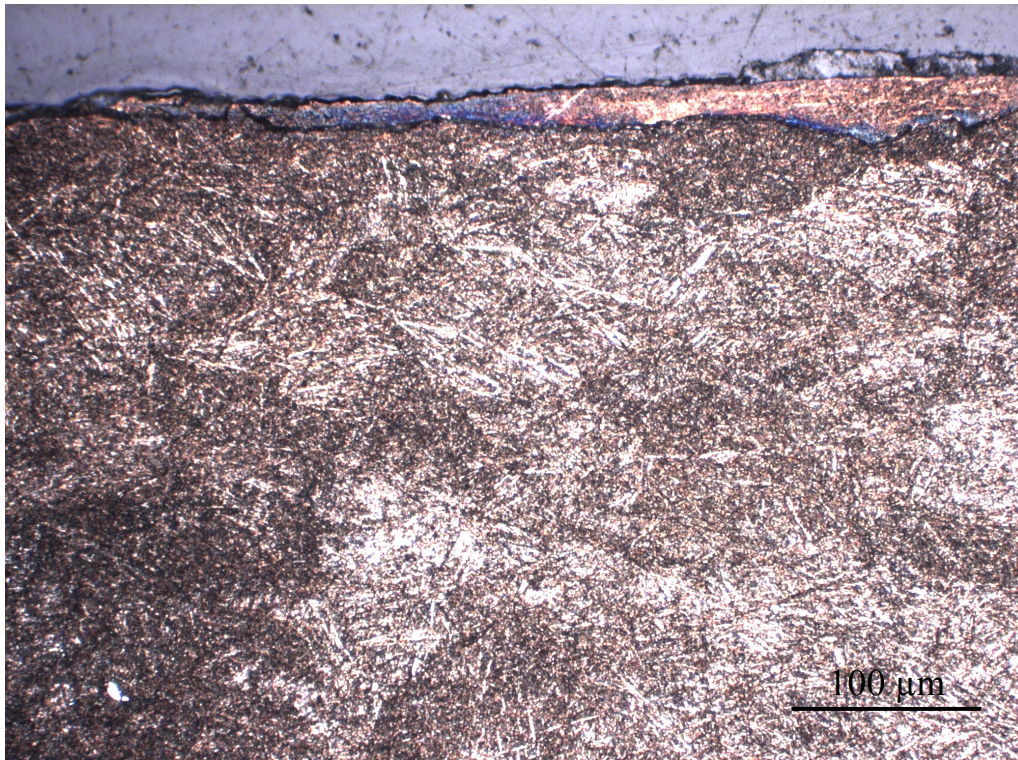


Figure 4.7: Optical image of cross section parallel to rolling direction of TBM cutter 314. 200X magnification.

Figure 4.7 shows an optical image of cutter 314. A crack growing in a direction parallel to the surface is seen, indicating wear by fatigue, commonly seen in rolling contacts. The absence of a lamellar layer at the surface also indicate rolling to be the dominating mode of contact. No TBM cutter sample showed signs of lamellar surface structures. This is therefore the only image presented from these samples.

Figures 4.8 and 4.9 both show RIAT mini-cutters worn by quartzite, sample 8 and 11 respectively. Sample 8 show no sign of a lamellar layer, indicating a rolling

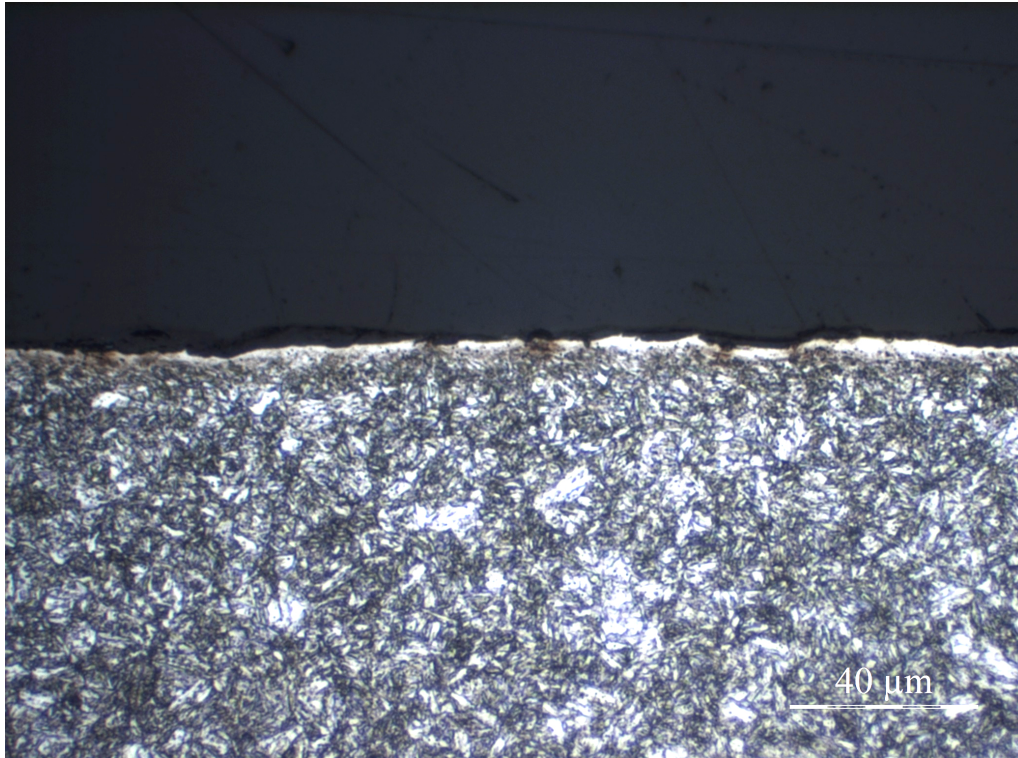


Figure 4.8: Optical image cross section parallel to rolling direction of RIAT mini-cutter 8, worn by quartzite. 500X magnification.

mode of contact. The deformed layer seen in sample 11 indicate sliding to be a contributing contact mode.

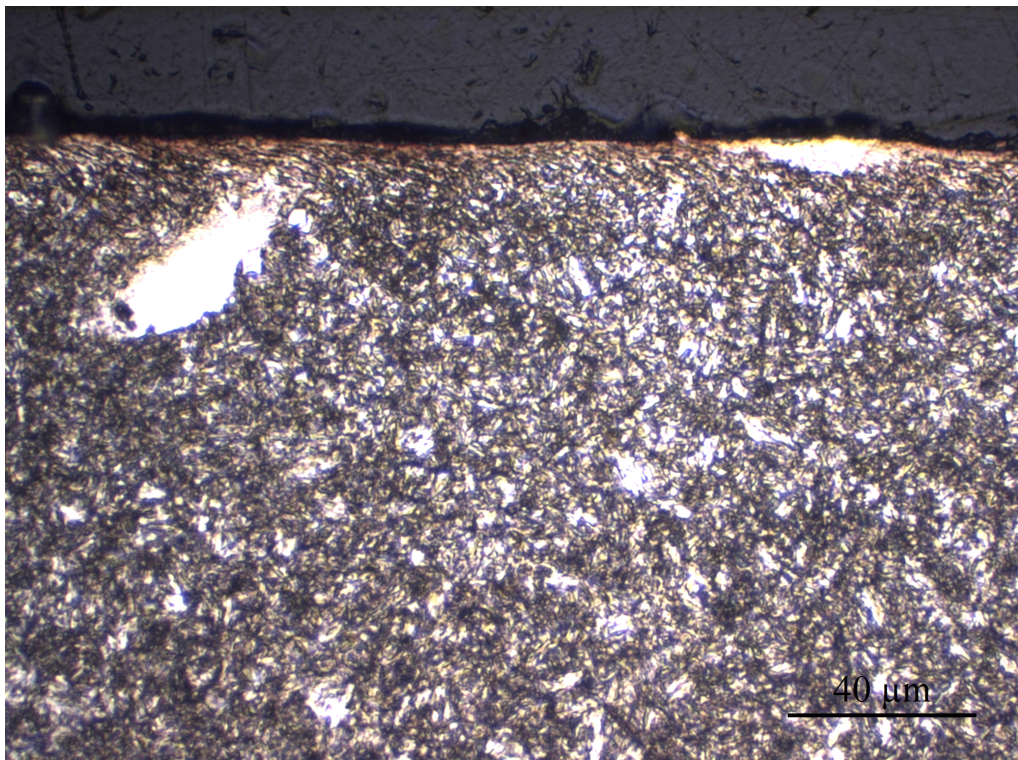


Figure 4.9: Optical image cross section parallel to rolling direction of RIAT mini-cutter 11, worn by quartzite. 500X magnification.

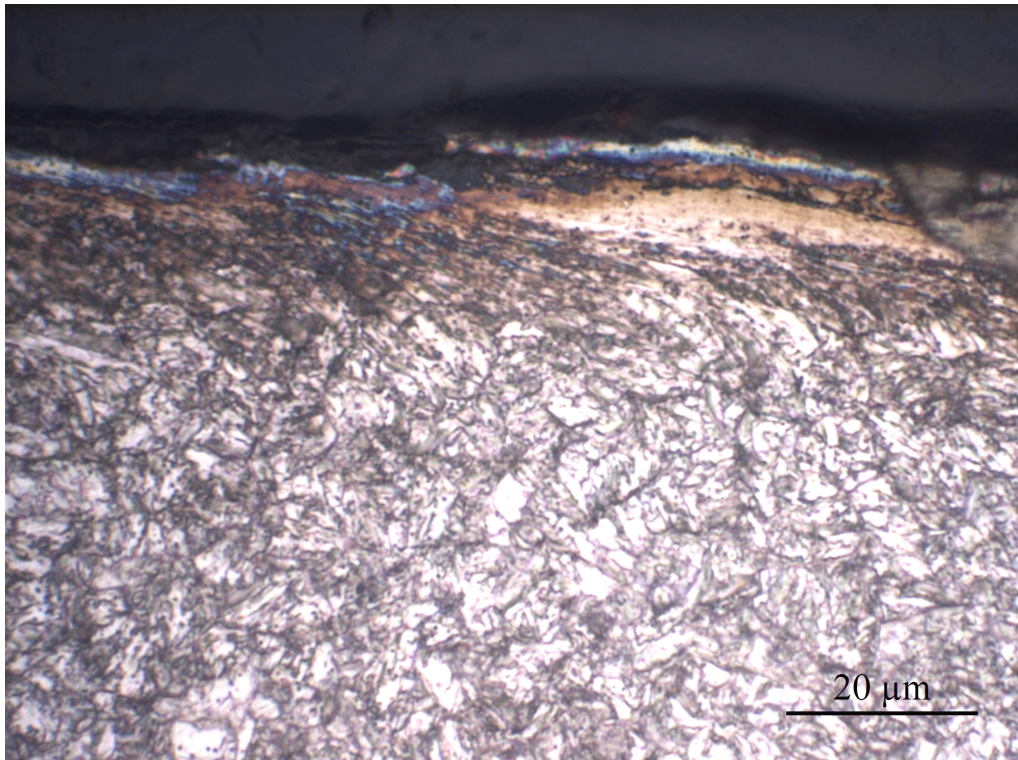


Figure 4.10: Optical image cross section parallel to rolling direction of RIAT mini-cutter 003, worn by granite. 1000X magnification.

Surface lamellae are found in both the Iddefjord granite sample 3, shown in Figure 4.10 and in the Chinese basalt sample 001, in Figure 4.11. This layer indicate sliding to be a contributing contact mode for both these rock types.

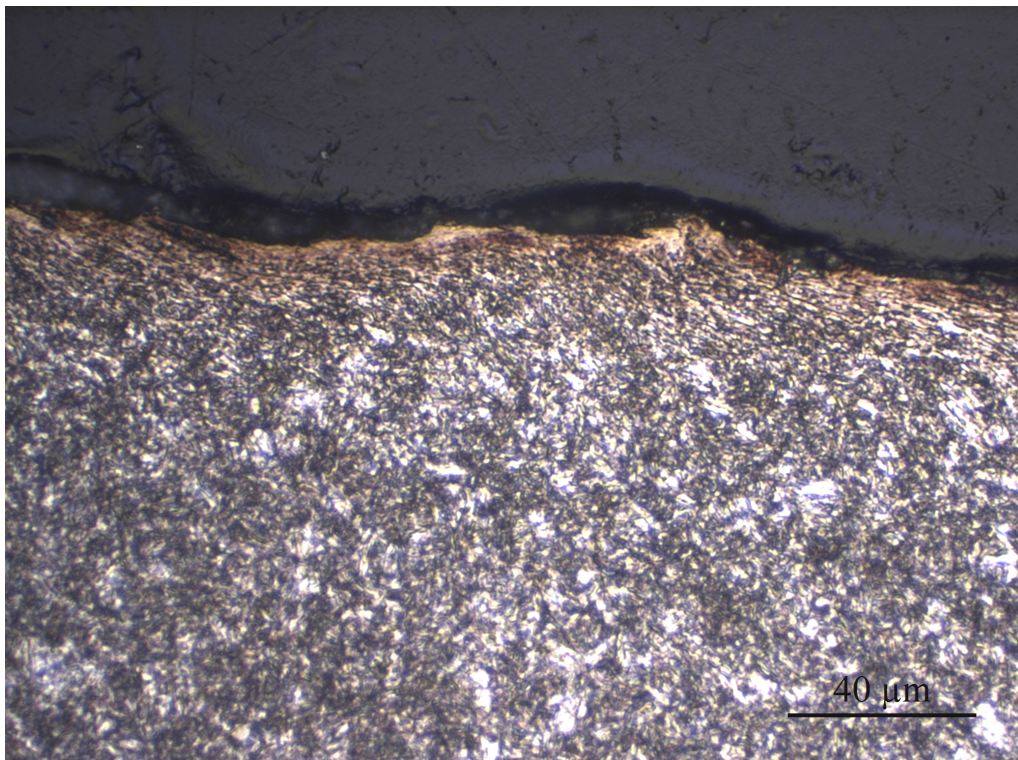


Figure 4.11: Optical image cross section parallel to rolling direction of RIAT mini-cutter 001, worn by Chinese basalt. 500X magnification.

4.2.2 Wear Mechanisms

Cuts both parallel and transverse to the rolling direction were used to identify wear mechanisms of the TBM cutters and RIAT mini-cutters. From optical microscope imaging, fatigue and folding of asperities may be discerned. To identify abrasive wear, the worn surface is studied and SEM-imagery is used.

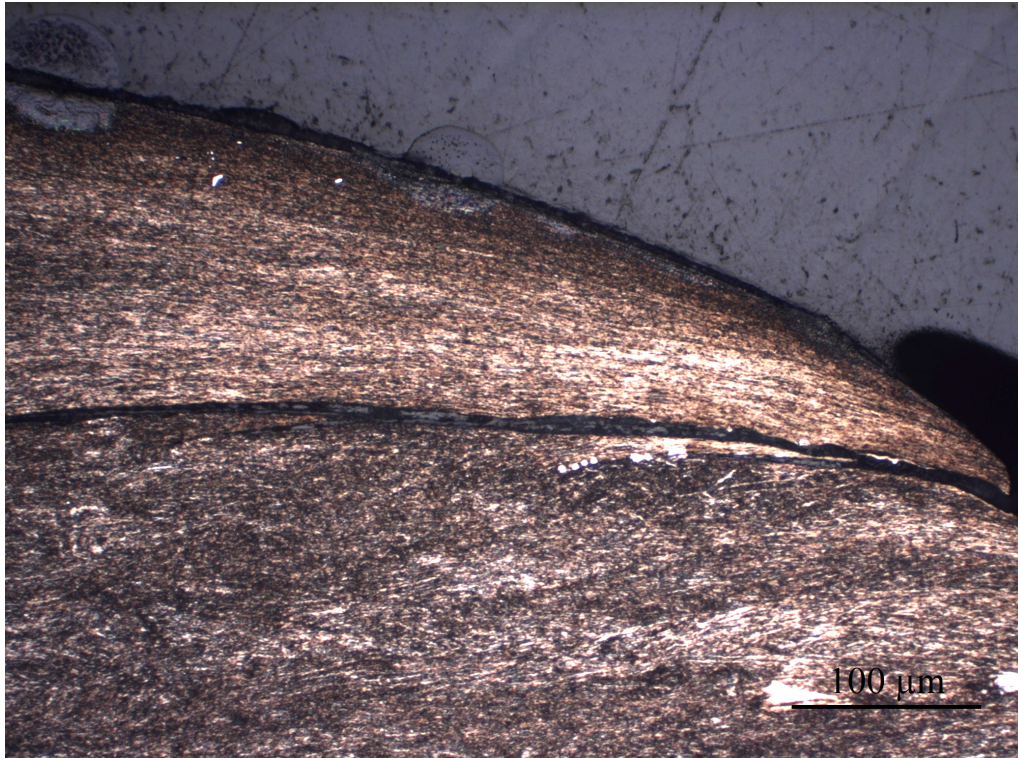


Figure 4.12: Crack growth in TBM cutter 302, transverse cross section. 200X magnification.

Plastic deformation transverse to the rolling direction does not bear significant evidence of dominating contact mode, but may indicate folding of asperities. When folded, a crack forms by the two surfaces pressed together. Figure 4.12 shows a transverse cut of TBM cutter 302. A lamellar structure is seen with a crack growing parallel to the lamellae direction. The white spots seen might be carbides, as these are left unaffected by the etchant used. No further examinations of the white areas have been performed. The oxide layer of the asperity surface will inhibit the formed crack from closing by re-adhesion.

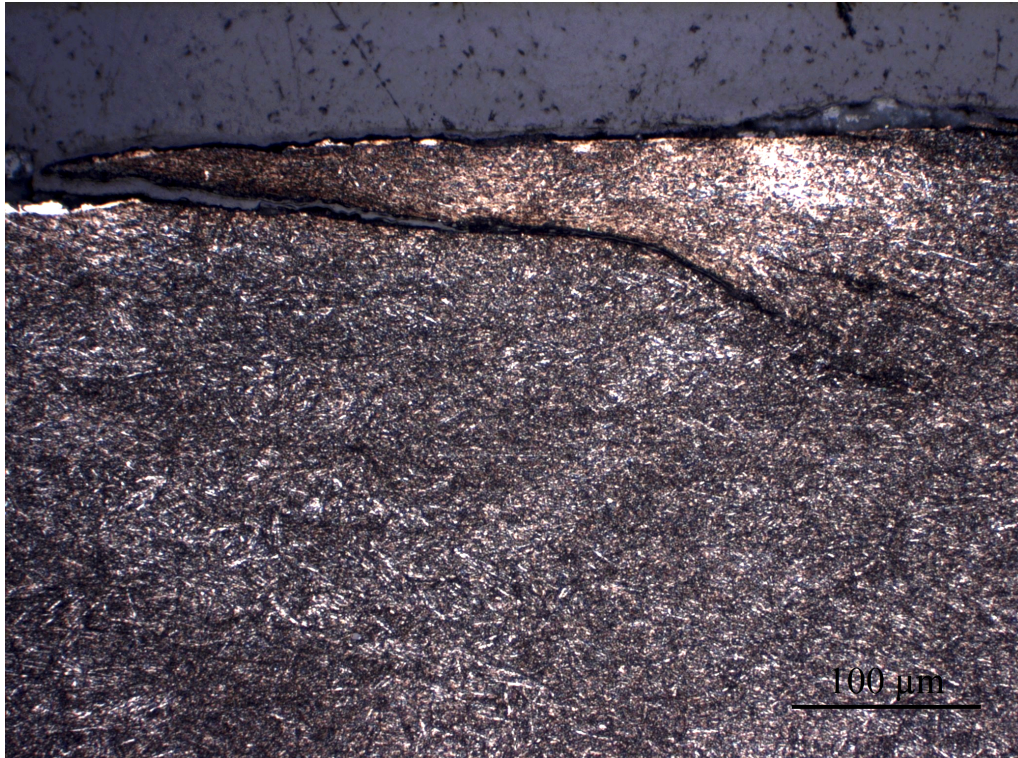


Figure 4.13: Crack growth in TBM cutter 302, parallel cross section. 200X magnification.

Figure 4.13 and Figure 4.14 show parallel cuts of cutter 302. Several cracks are seen, some of which with subsurface origin, as there are no connection to the surface. The crack connected to the surface may have been a subsurface crack which has reached the surface or an asperity folded by plastic deformation with following crack growth from fatigue. The oxide layer of the asperity surface will inhibit the formed crack from closing by re-adhesion. This will also be the case for the new crack formed, as water is present in varying amounts during tunnel boring. No logging of water content has been made during this work.

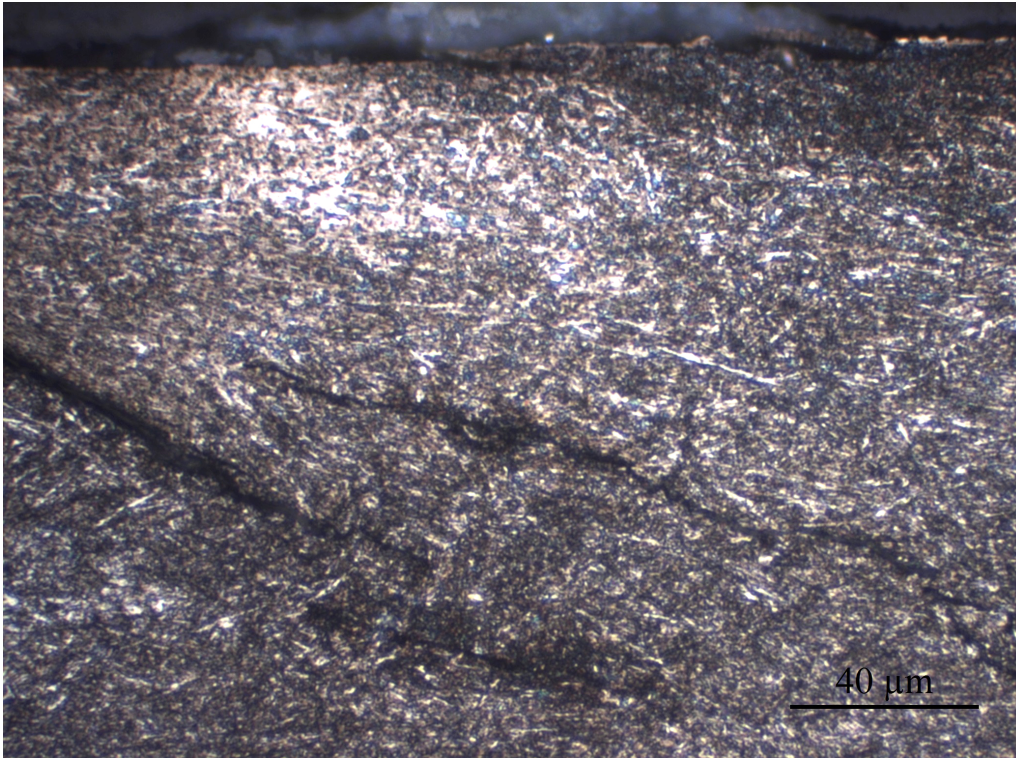


Figure 4.14: Crack growth in TBM cutter 302, parallel cross section. 500X magnification.

The cracks more clearly shown in Figure 4.14 have probably formed subsurface. The formation of such cracks indicate fatigue. When connected to the surface, debris is released by way of chipping.

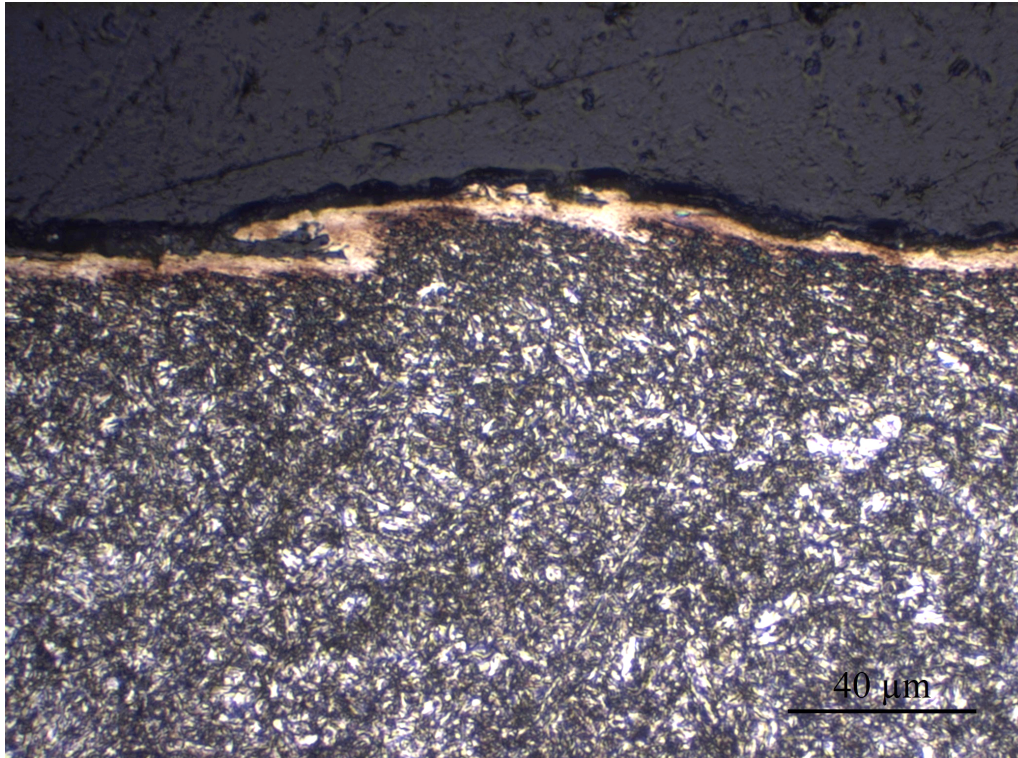


Figure 4.15: Folding in RIAT mini-cutter 002, worn by Chinese basalt, parallel cross section. 500X magnification.

Figure 4.15 shows an optical image of mini-cutter 002, worn by Chinese basalt. A bright layer of deformed metal is seen at the surface. Folding of an asperity is captured, with a crack likely to form in the interface of the two surfaces.

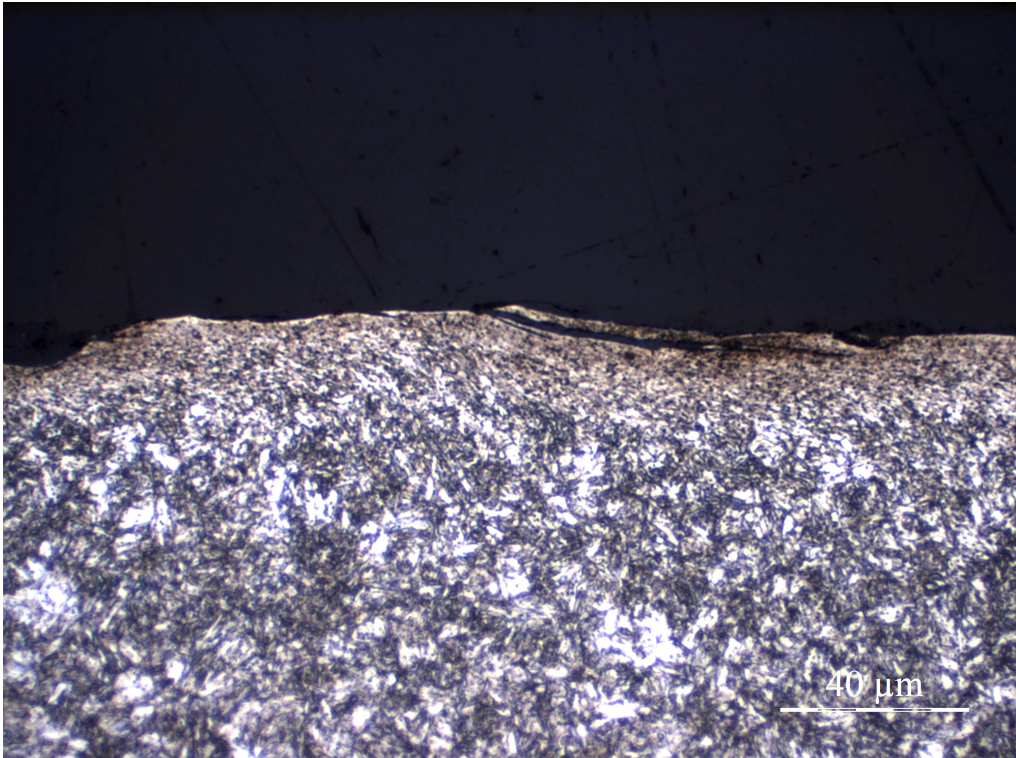


Figure 4.16: *Folding in RIAT mini-cutter 3, worn by Iddefjord granite, parallel cross section. 500X magnification.*

Figure 4.16 depicts a cross sectional image of mini-cutter 3, worn by Iddefjord granite. Folding is seen at a progressed stage, as the crack has grown through the material and is close to resurfacing.

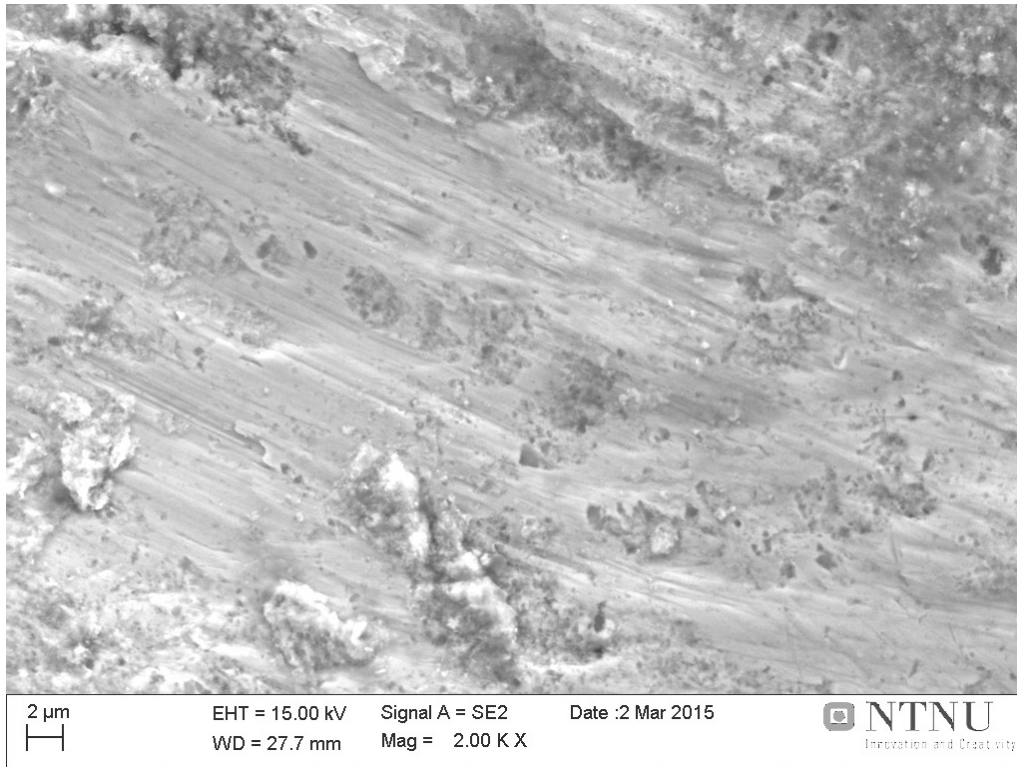


Figure 4.17: SEM image of a RIAT mini-cutter surface. Sample 4, worn by quartzite. Secondary electron signal.

Abrasive wear was studied by way of electron microscope. Figure 4.17 depicts the wear surface of mini-cutter 4, worn by quartzite. The parallel lines in the surface are tracks made by abrasive ploughing.

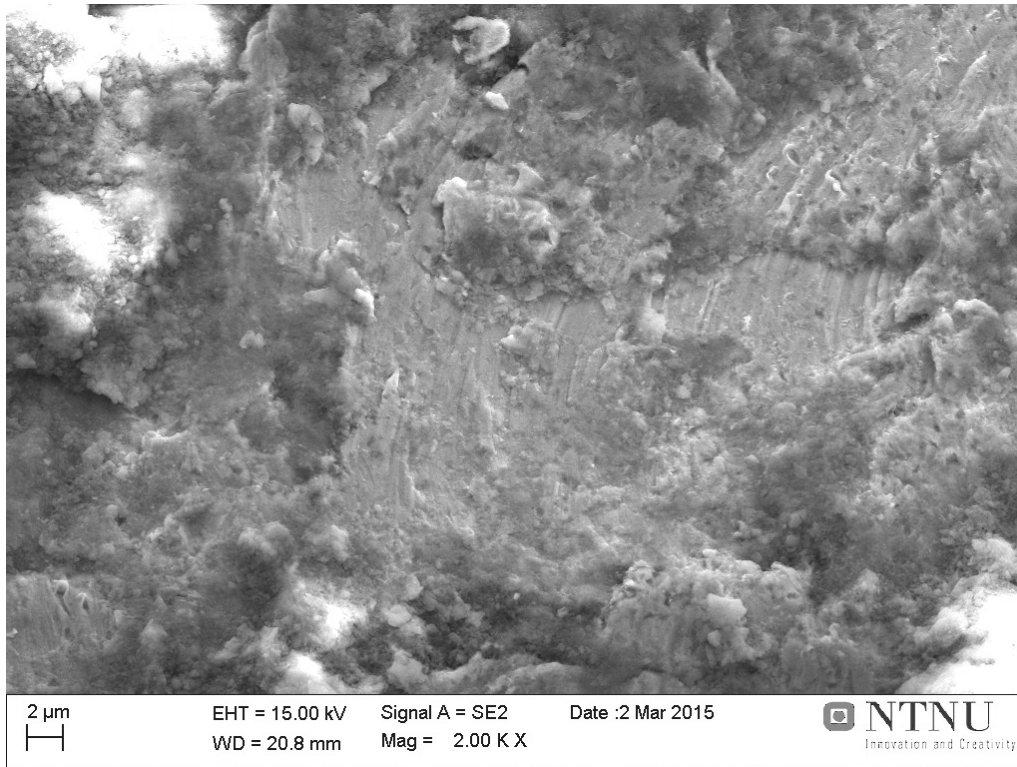


Figure 4.18: SEM image of a RIAT mini-cutter surface. Sample 6, worn by Iddefjord granite. Secondary electron signal.

Figure 4.18 shows the wear surface of mini-cutter 6, worn by Iddefjord granite. Wear lines from abrasive ploughing are seen, although less prominent than in the quartzite sample of Figure 4.17. The bright areas at the top left and bottom right corners of the image are rock debris embedded in the surface. A substantial difference is noted in the amount of debris embedded in the surface from the highly abrasive quartzite and the less abrasive granite. This is seen in Figure 4.19, which shows the wear surface of RIAT mini-cutter 3, worn by Iddefjord granite. The image signal is backscattered electrons, producing a Z-contrast in which steel appears bright relative to rock debris. A further increase of rock debris and decrease in ploughing was found in the basalt sample. Images of rock debris of basalt and quartzite are found in the appendix.

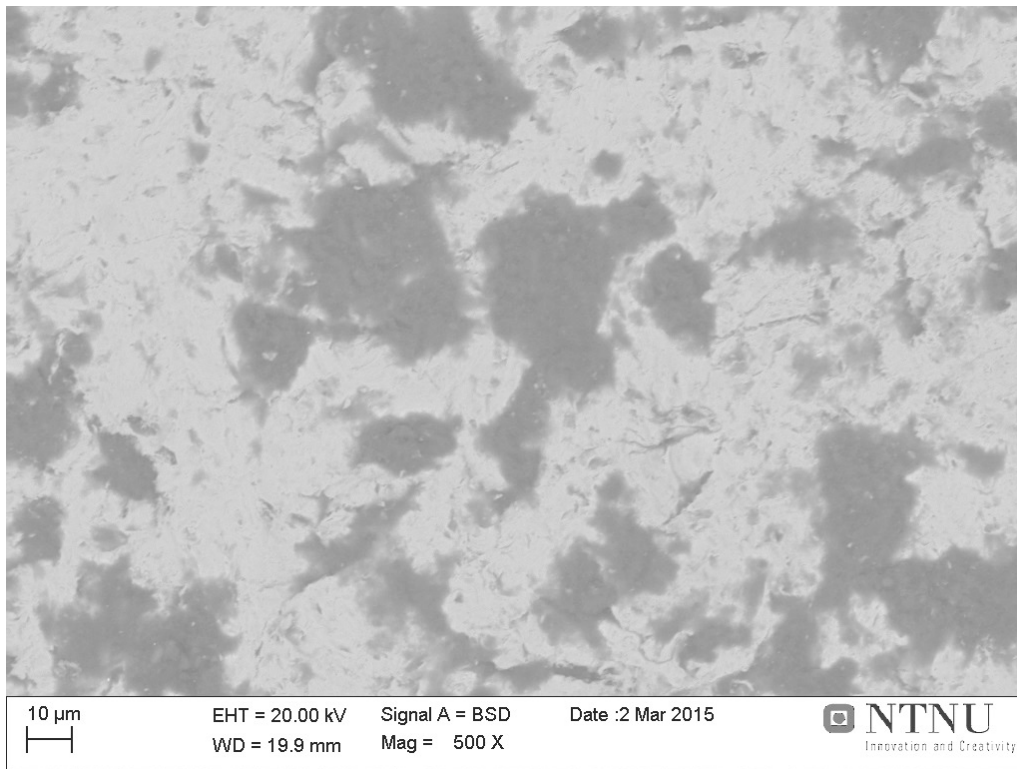


Figure 4.19: SEM image of wear surface of RIAT mini-cutter 3, worn by Iddefjord granite. BSE signal. Bright areas are steel, dark areas are rock debris.

4.2.3 Deformation Structure

Cross sections were cut into the wear surfaces of all sample types by way of FIB. This was done to study the deformation structure of the different samples. Milling by Gions ensures that the cross section causes a minimal amount of plastic deformation. The deformation present is therefore assumed to have occurred during TBM and RIAT operations. Thickness measurements are performed by visual inspection. This may introduce significant scatter to the results when the microstructure is heavily deformed.

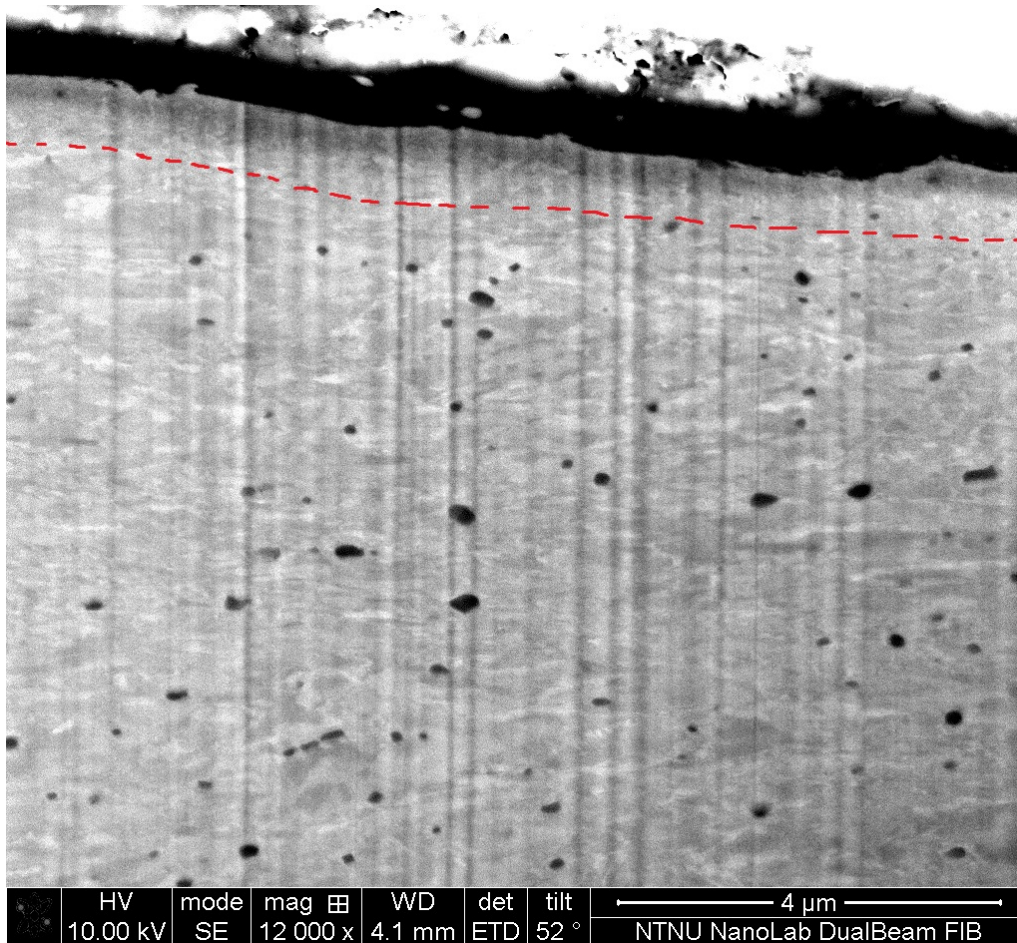


Figure 4.20: TBM cutter disc 314, transverse cut cross section. Dotted line imply border for nanocrystalline deformation layer.

Figure 4.20 shows a cross section of TBM cutter 314 taken perpendicular to the rolling direction. This type of cross section is called a transverse cut. A layer of fine grains, approximately 1 μm thick, is observed just below the specimen surface. This is a nanocrystalline layer, generated by heavy deformation during TBM operations.

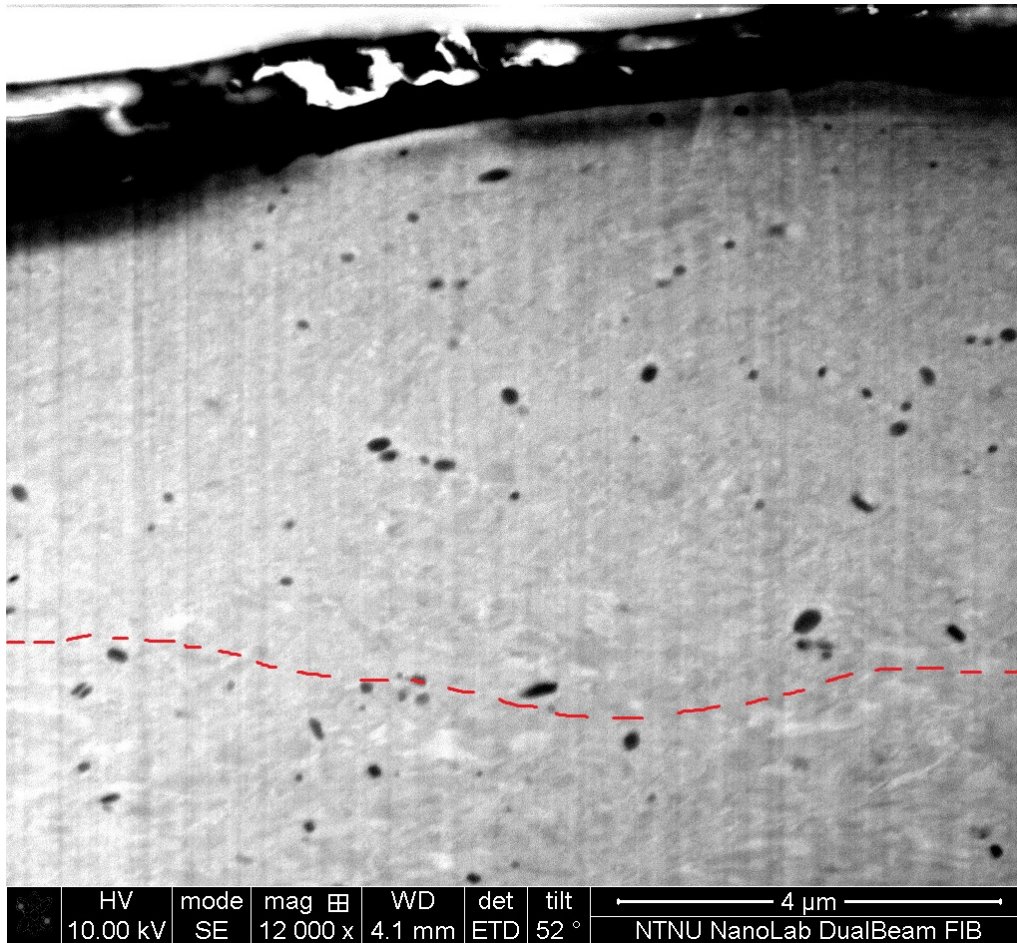


Figure 4.21: TBM cutter disc 302, transverse cut cross section. Dotted line imply border for nanocrystalline deformation layer.

Figure 4.21 shows a transverse cut cross sectional image of TBM cutter 302. A nanocrystalline deformation layer, 4-6 μm in thickness, is seen near the surface. As cutters 314 and 302 were worn by the same rock, differing positions will cause varying depth of deformation. This result is indicated by the difference in layer thickness and supported by Figure 4.2, describing reasons for cutter replacements in different positions.

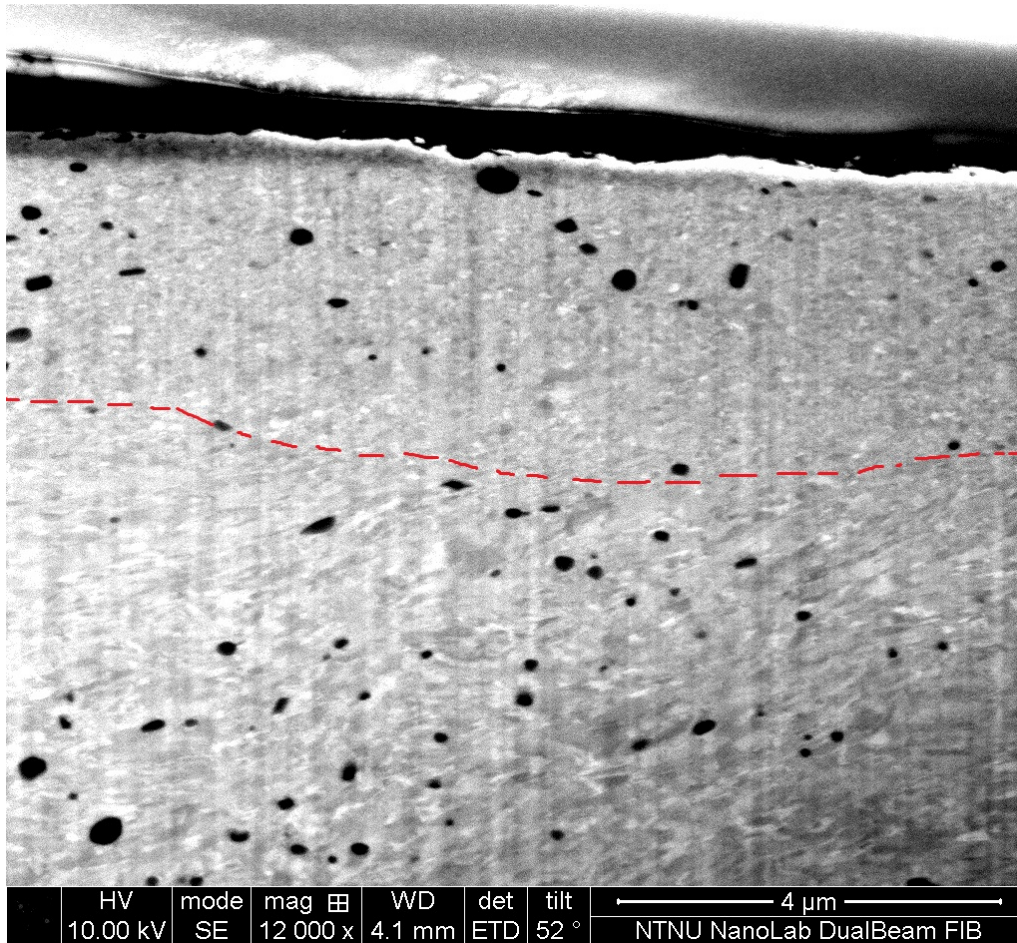


Figure 4.22: TBM cutter disc 302, parallel cut cross section. Dotted line imply border for nanocrystalline deformation layer.

Figure 4.22 shows the cross section of cutter 302 in parallel to the rolling direction. This was done to identify possible differences between the two directions when using FIB. A 3 μm layer of nanocrystalline grains is seen. The two cross sections are not enough to decide if the 2-3 μm thickness difference observed between transverse and parallel cross sections are significant, but they do indicate high local variations as they originate from the same sample area.

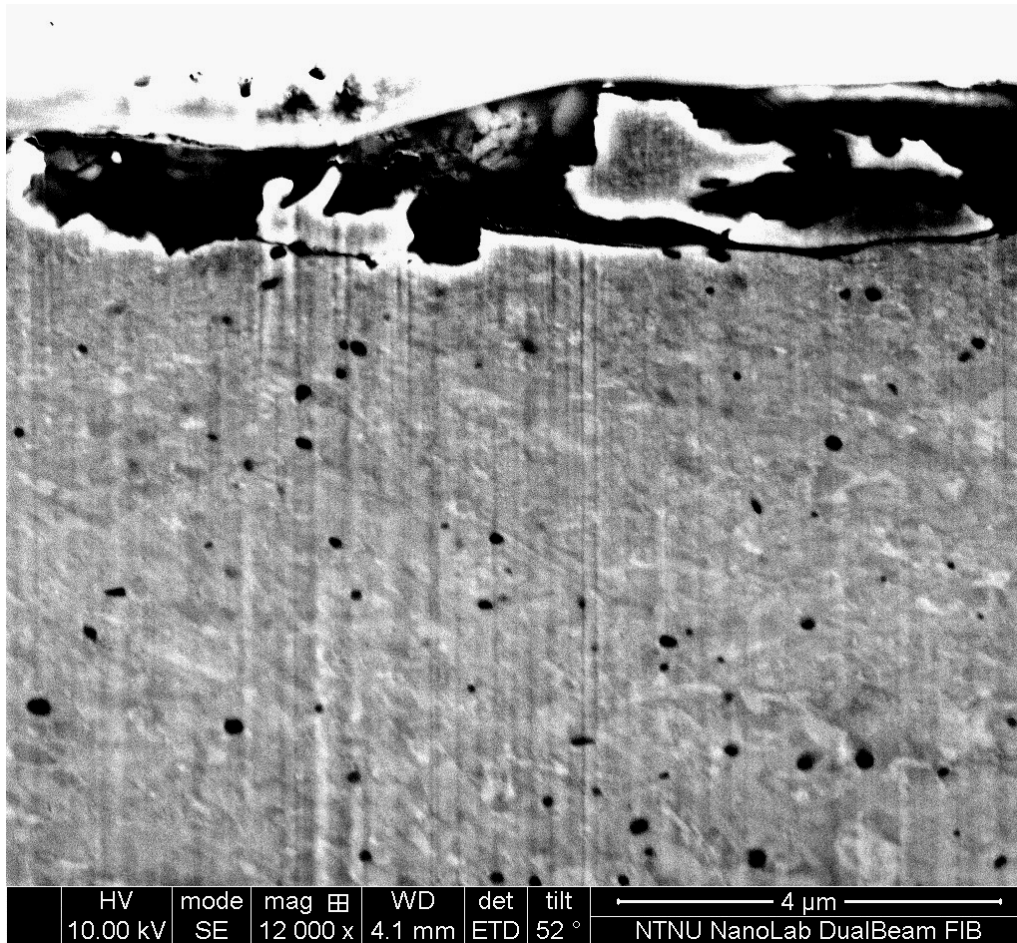


Figure 4.23: TBM cutter disc 140, parallel cut cross section. Dotted line imply border for nanocrystalline deformation layer.

Cross sections in both transverse and parallel direction were taken of TBM cutter 140. These are seen in Figure 4.23 and Figure 4.24, respectively. The parallel cross section shown in Figure 4.23 give no indication of a nanocrystalline deformation layer. Homogeneous microstructure is seen with smaller areas of fine grain structure near the surface.

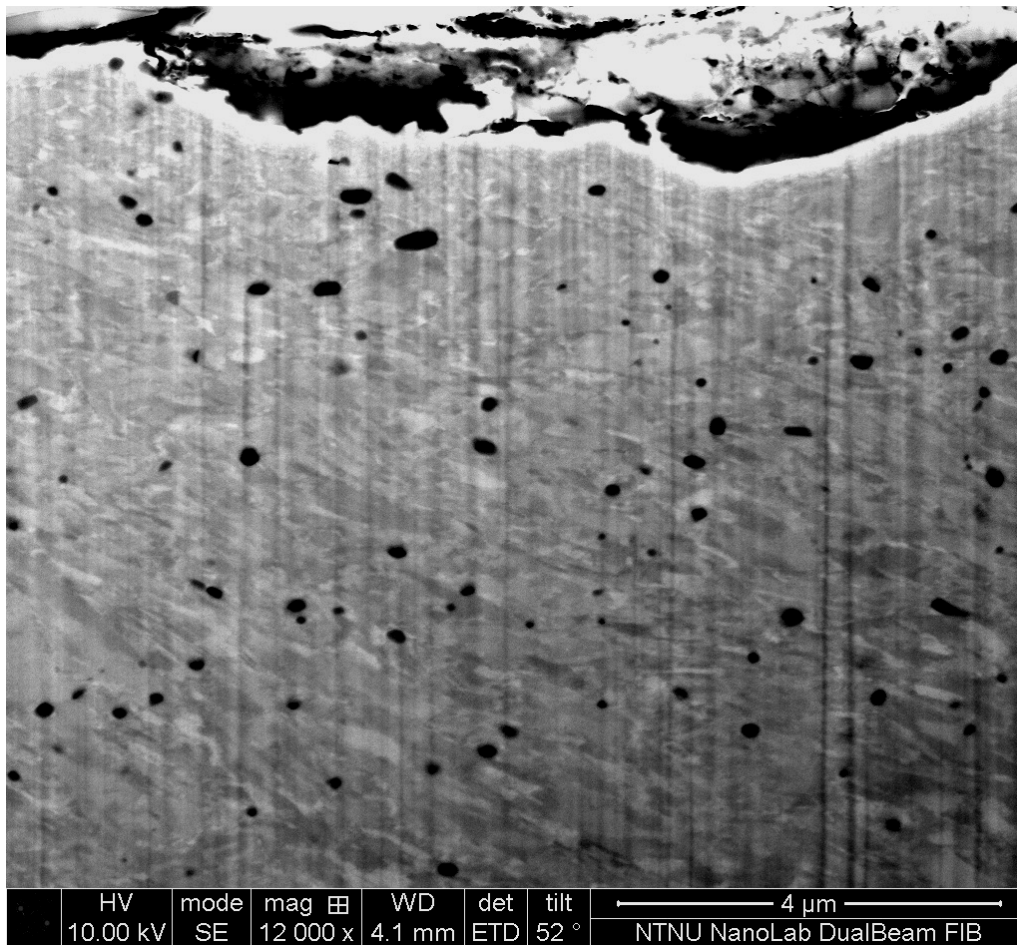


Figure 4.24: TBM cutter disc 140, transverse cut cross section.

Figure 4.24 shows the transverse cross section of TBM cutter 140. No indication of a nanocrystalline grain structure is seen. The similarity between transverse and parallel cross sections in cutter 140 give no reason to assume directional dependency in deformation layer thickness. The lack of a nanocrystalline structure reduce the value of comparing these results to the various layer thickness found in cutter 302.

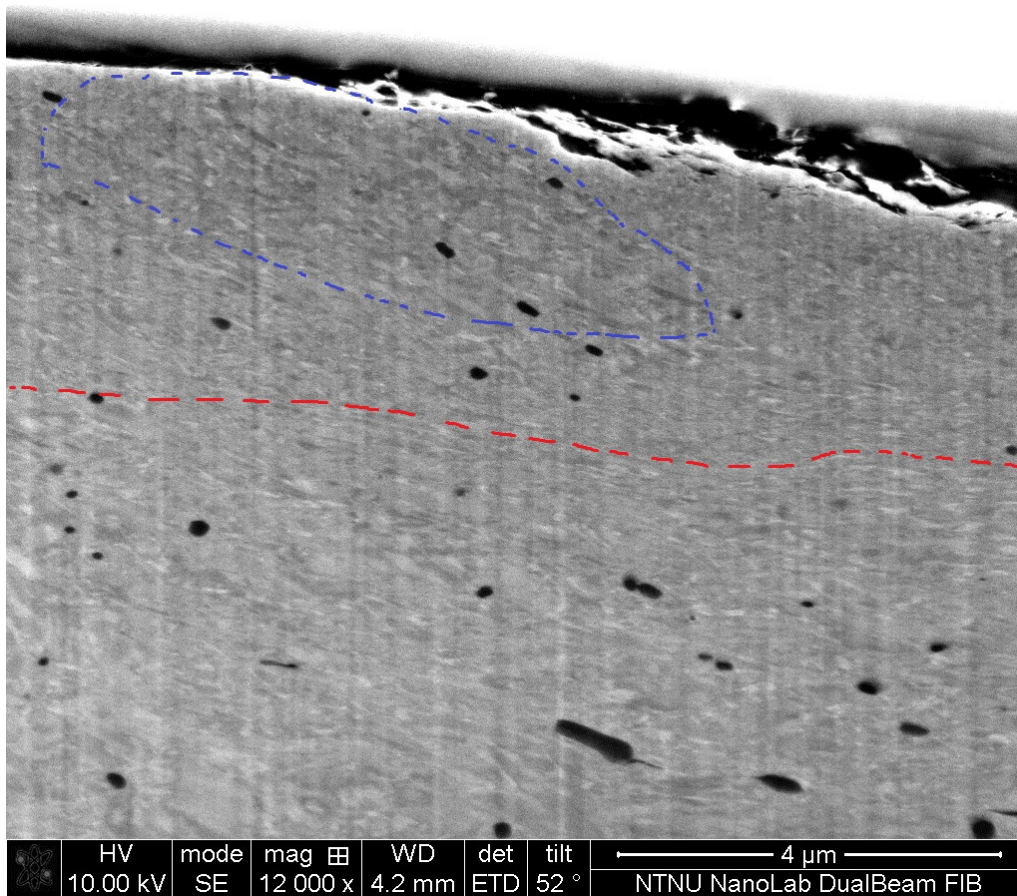


Figure 4.25: TBM cutter disc 383, transverse cut cross section. Dotted red line imply possible border for nanocrystalline deformation layer. Dotted blue line indicate area of possible grain growth.

Figure 4.25 depicts a cross section of TBM cutter 383. A possible nanocrystalline layer of thickness 2-3 μm is seen. The microstructure appears to be greatly deformed, with bulk structure only appearing at the bottom of the image. The grains in the top layer marked by a blue dotted line appear larger than in for example Figure 4.24. This might indicate grain growth.

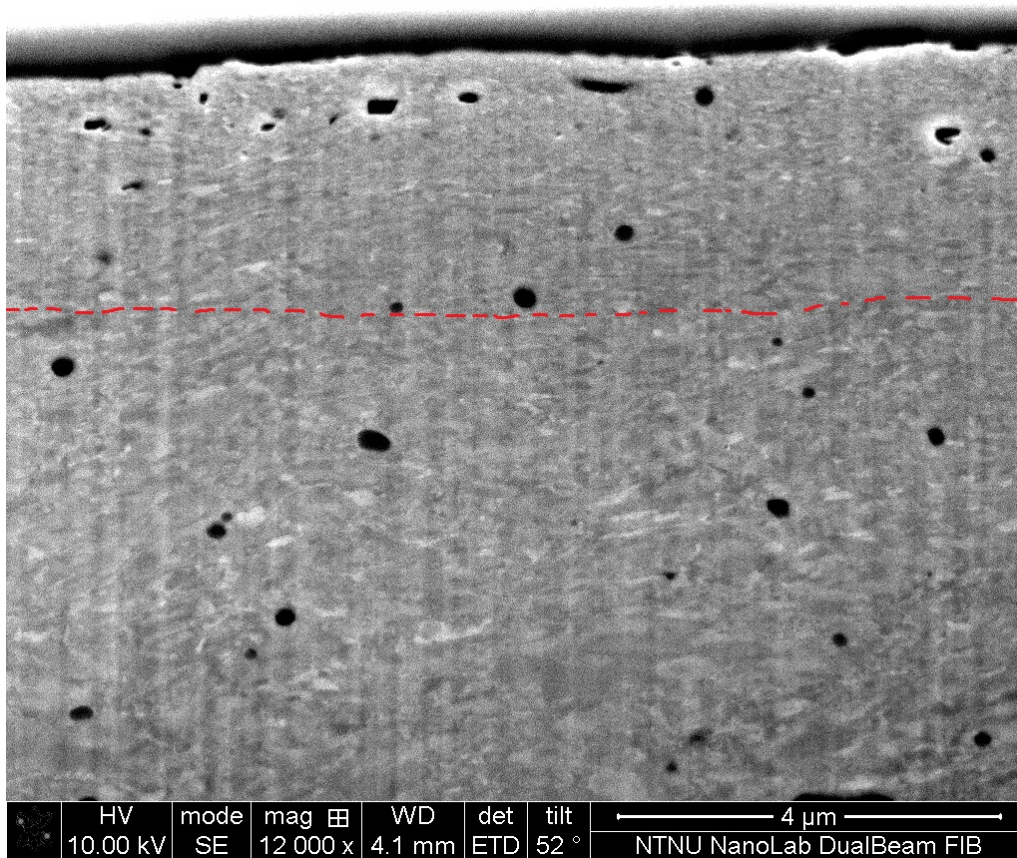


Figure 4.26: FIB cross section. Surface worn by Chinese basalt, sample 002, transverse cut cross section. Dotted line imply border for nanocrystalline deformation layer.

Figure 4.26 shows a cross section of RIAT mini-cutter 002, worn by Chinese basalt. Nanocrystalline grains are observed in a 2-3 μm thick layer. Bulk microstructure is seen at the bottom of the image. The intermediate layer is a gradual transition between bulk and nanocrystalline, indicating a high degree of deformation. This makes layer thickness determination challenging. As this cross section is in the transverse relative to the rolling direction, no lamellar structure is visible.

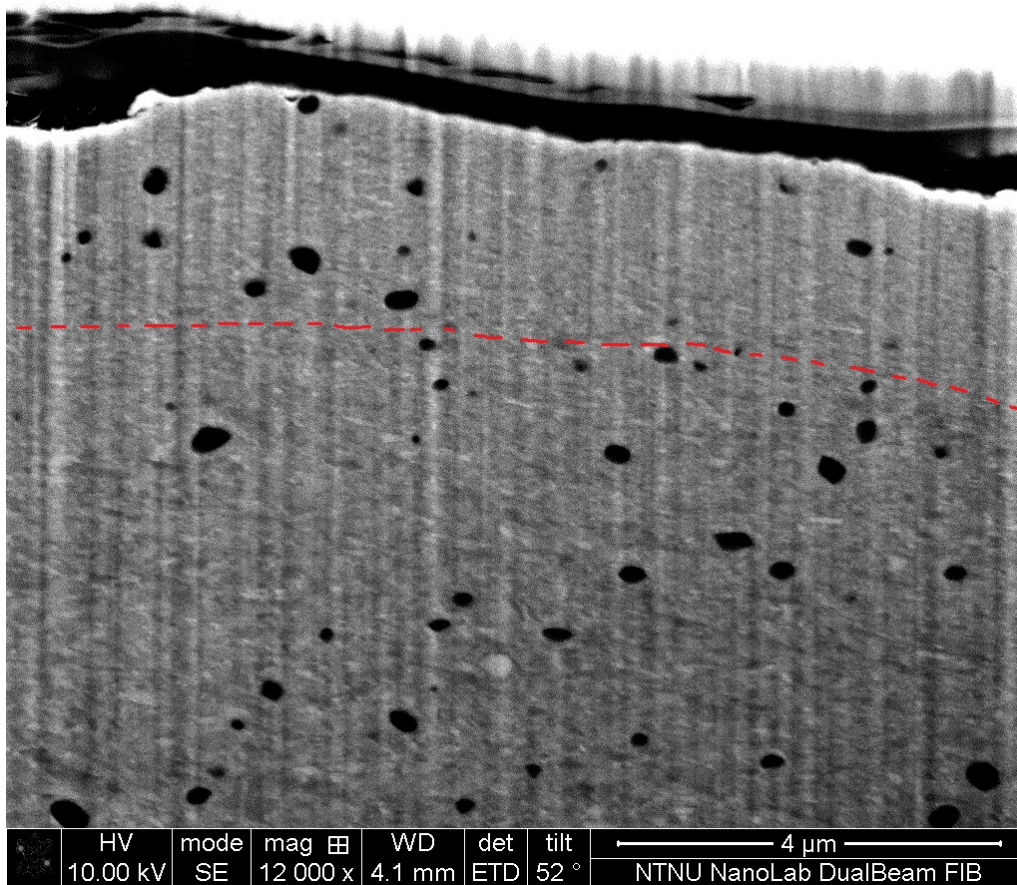


Figure 4.27: FIB image of RIAT mini-cutter 3, worn by Iddefjord granite. Fine grained area visible at the surface of the specimen. Dotted line imply possible border for nanocrystalline deformation layer.

The FIB cross section of sample 3, worn by Iddefjord granite is shown in Figure 4.27. A nanocrystalline layer of approximate thickness 2-3 μm is seen. An area of uncertainty to address when measuring these layers is the lack of an exact "boundary" separating "nanocrystalline" and "heavily deformed, but larger" grain structure. An image of the cross section shown in Figure 4.27 is presented with a lower magnification in Figure D.7. A possible layer thickness of 5-7 μm is indicated. Discussion of these results will assume the layer thickness to be 2-3 μm . This is due to the higher magnification of the former image, which is believed to give better grounds for layer thickness estimation.

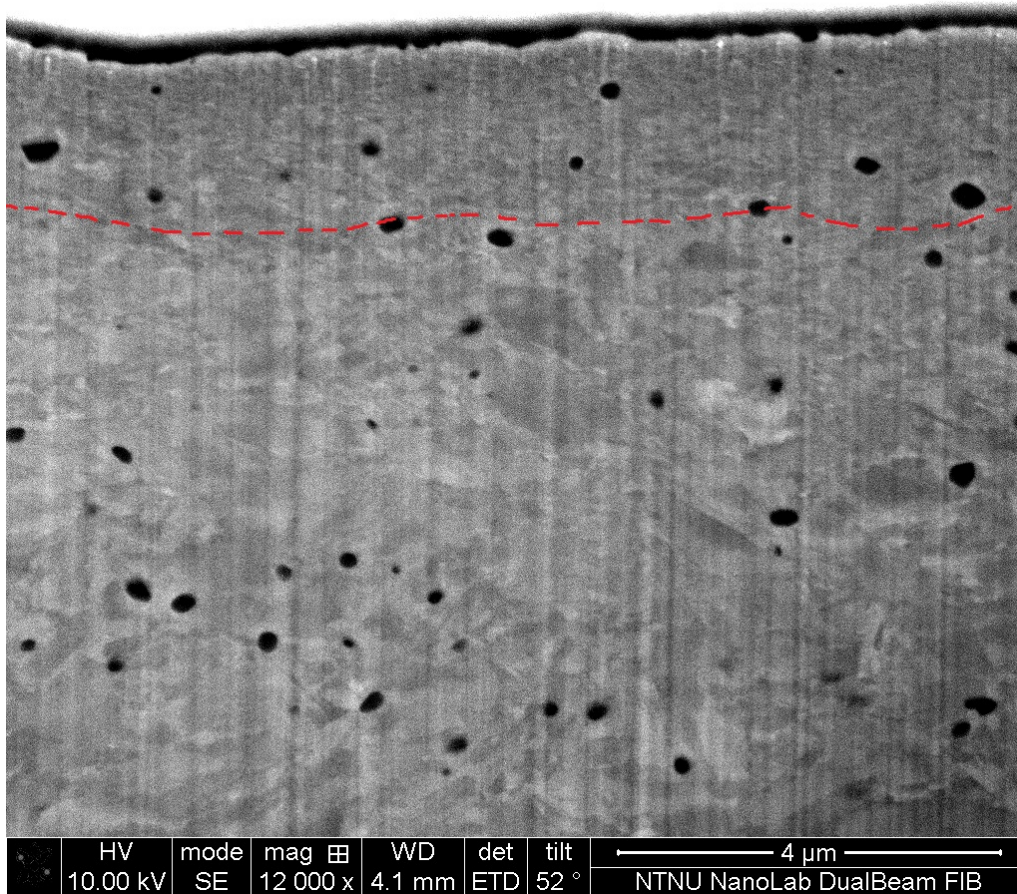


Figure 4.28: FIB cross section. Surface worn by Quartzite, sample 11, transverse cut cross section. Dotted line imply border for nanocrystalline deformation layer.

Figure 4.28 shows a cross sectional image of RIAT mini-cutter 11, worn by quartzite. A nanocrystalline deformation layer is seen at the upper most area of the microstructure. The deformed region stretches about $2\ \mu\text{m}$ into the material. A coarse microstructure below the nanocrystalline layer, relative to the mini-cutters worn by basalt and granite, is observed.

An observation, unrelated to the effect of load, concerning both the TBM cutters and RIAT mini-cutters is the presence of small, black spots throughout the FIB sample images. EDS mapping was used to decide the elements present in these spots. Results indicate that they are mainly VC (vanadium carbides) with a slight, but clear, contribution from Mo. Quantitative analysis of the particles was not performed. The size of the carbides indicate that they might give a strengthening effect, while their shape is optimal to avoid stress concentrations.

4.3 Tempering

Hardness profiles were measured on each of the TBM cutter samples and one RIAT mini-cutter. To measure areas of similar load and rolling distance, the indentations were made on cross sections parallel to the rolling direction. Each hardness value presented represent one indentation. Some scatter and erroneous values is seen due to the mixed nature of martensitic microstructure.

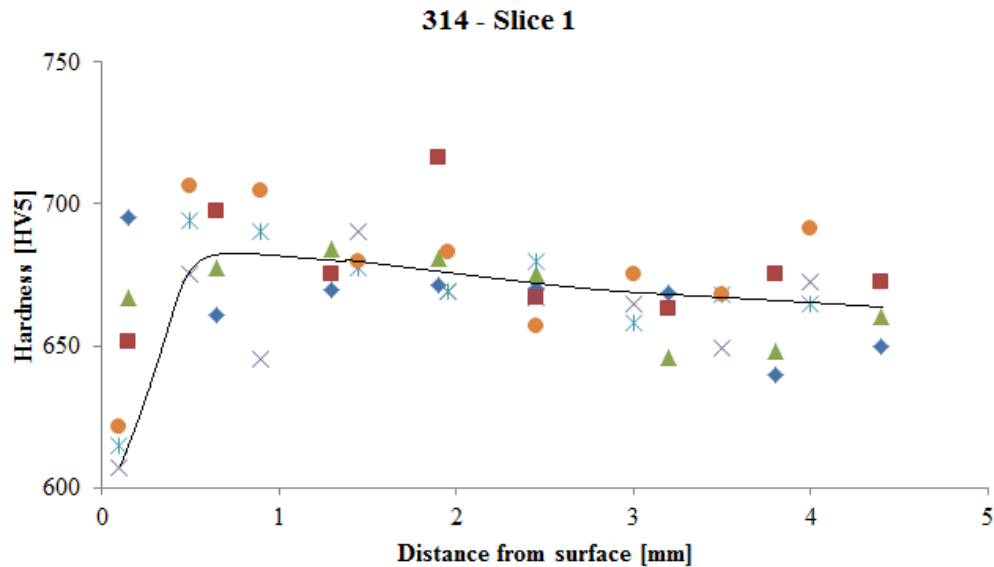


Figure 4.29: Vickers hardness profile of 314 disc, slice 1

Figure 4.29 and Figure 4.30 show the hardness profiles of TBM cutter disc 314, slice 1 and 2, respectively. A drop in hardness is seen at the surface of slice 1. The softening is followed by an increase in hardness prior to stabilizing at approximately 660 HV5. This stable value is bulk hardness. Slice 2 shows no indication of surface softening, reaching a hardness increase of 6.1 %.

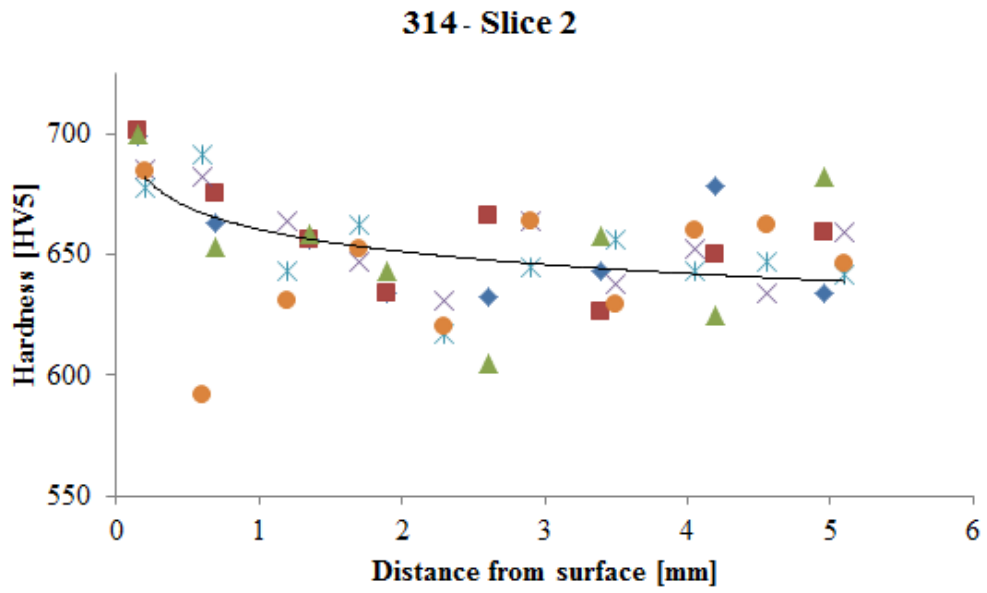


Figure 4.30: Vickers hardness profile of 314 disc, slice 2.

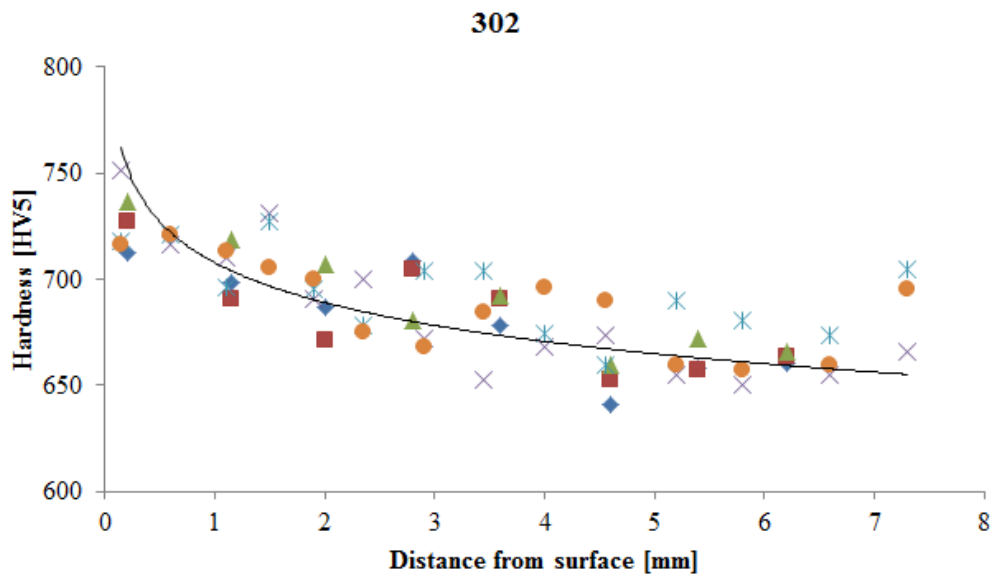


Figure 4.31: Vickers hardness profile of 302.

Figure 4.31 and Figure 4.32 show the hardness profiles of TBM cutter 302 and RIAT mini-cutter 3, worn in Iddefjord granite, respectively. An increase in hardness is seen in both graphs, with an approximate work hardening of 12.1 % in cutter 302 and 6.5 % in mini-cutter 3. A sharper gradient is observed in the RIAT mini-cutter. In addition, a slight gradient of softening is observed from bulk to near surface material.

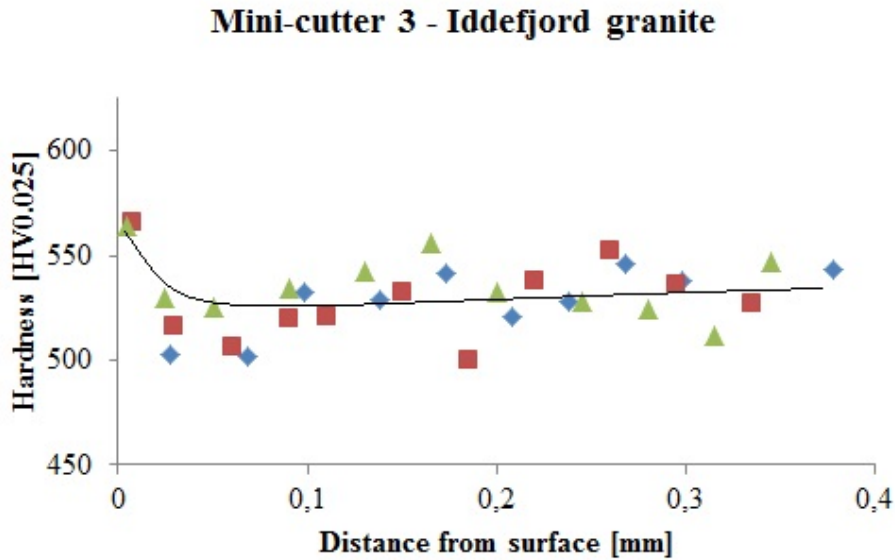


Figure 4.32: Vickers hardness profile of RIAT mini-cutter 3, worn by Iddefjord granite.

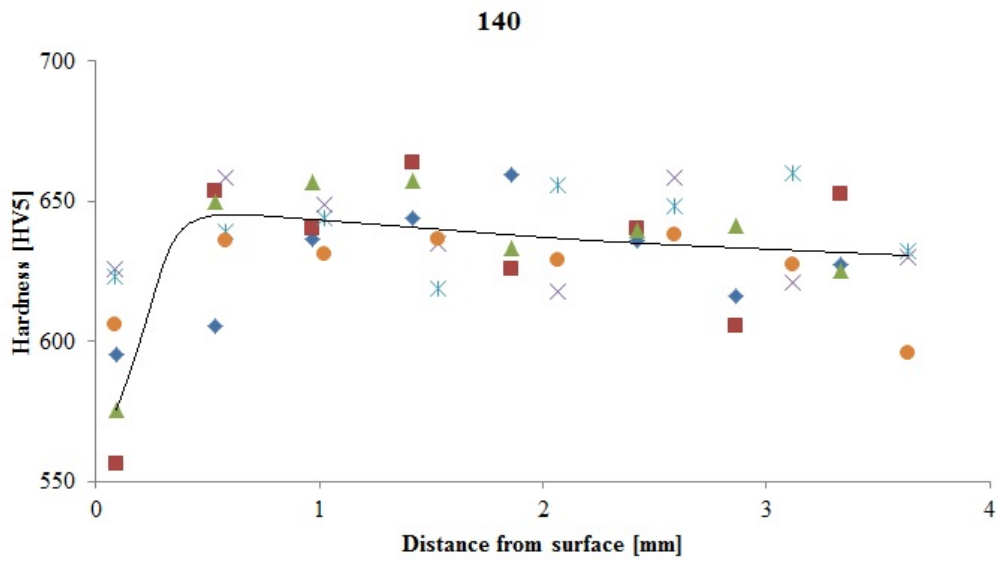


Figure 4.33: Vickers hardness profile of disc 140.

Figure 4.33 and Figure 4.34, depicting the hardness profiles of TBM cutters 140 and 383, respectively. Both indicate surface softening. The gradient of softening in all cutters appear similar and occur at approximately the same distance from the surface.

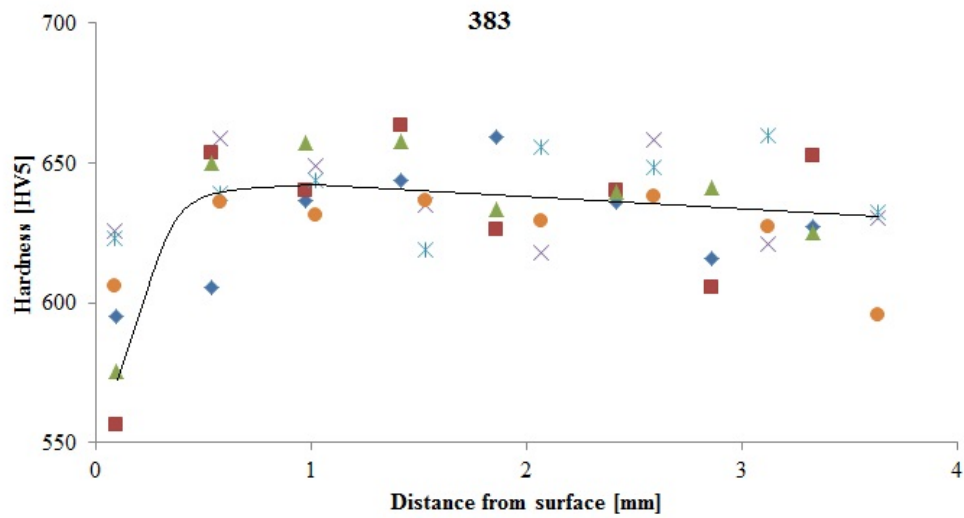


Figure 4.34: Vickers hardness profile of disc 383.

In parallel with hardness profiles, a tempering experiment has been performed on an unused TBM cutter, HD4. Three samples were tempered at each temperature and the tempering profile is shown in Figure 4.35. A slight softening is seen prior to a secondary hardening. The hardness decrease at approximately 500 °C, dropping from 670 HV5 to 300 HV5 at 700 °C.

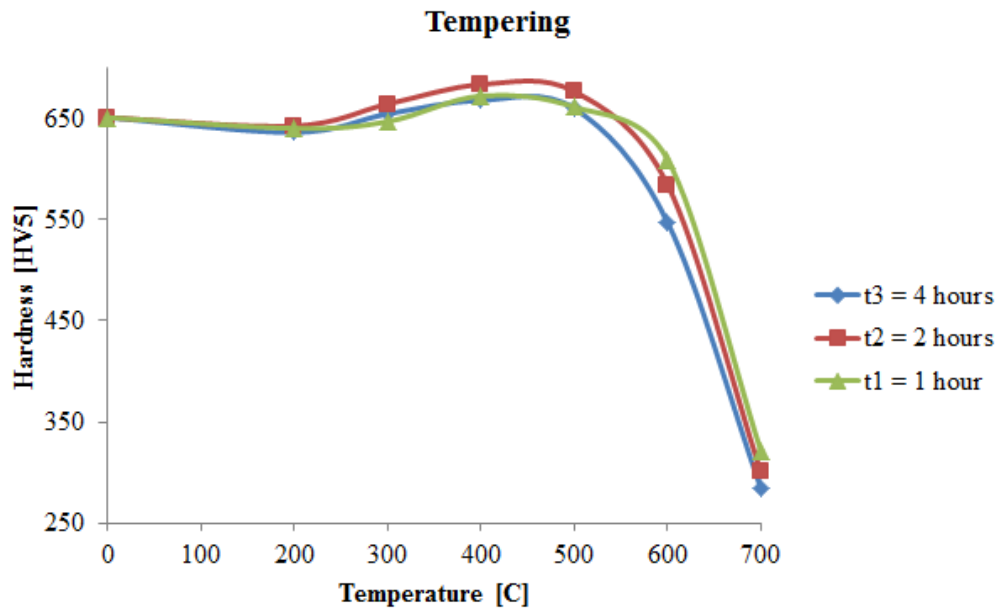


Figure 4.35: Hardness profile of cutter disc HD4 after 1, 2 and 4 hours of tempering.

Figure 4.36 illustrate an enlarged image of the most relevant parts of Figure 4.35. In addition, the surface hardnesses of cutters 140, 314 and 383 are shown as horizontal lines. The lines indicate which temperature is needed at various holding times to obtain the softening found in the cutters. The lines are the average of three hardness indentations made in the same area, at the same distance from the surface. Slight differences are seen from the different holding times, with 1 hour giving the highest temperature reached. As tempering is highly dependent of time and temperature, this result is expected.

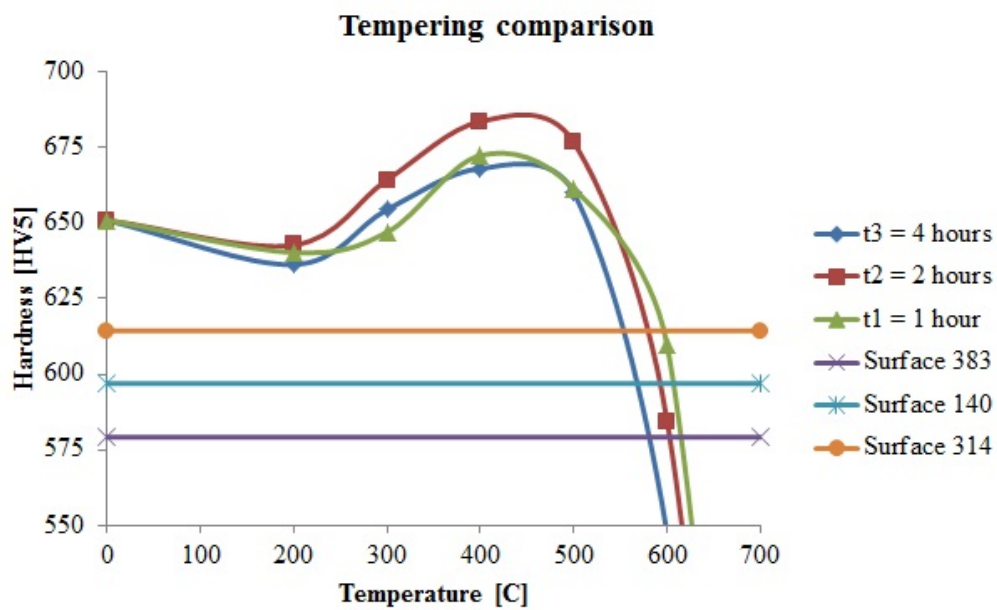


Figure 4.36: Hardness profile of cutter disc HD4 after 1, 2 and 4 hours of tempering. Horizontal lines indicate hardness at the wear surface of TBM cutters 140, 314 (slice 1) and 383.

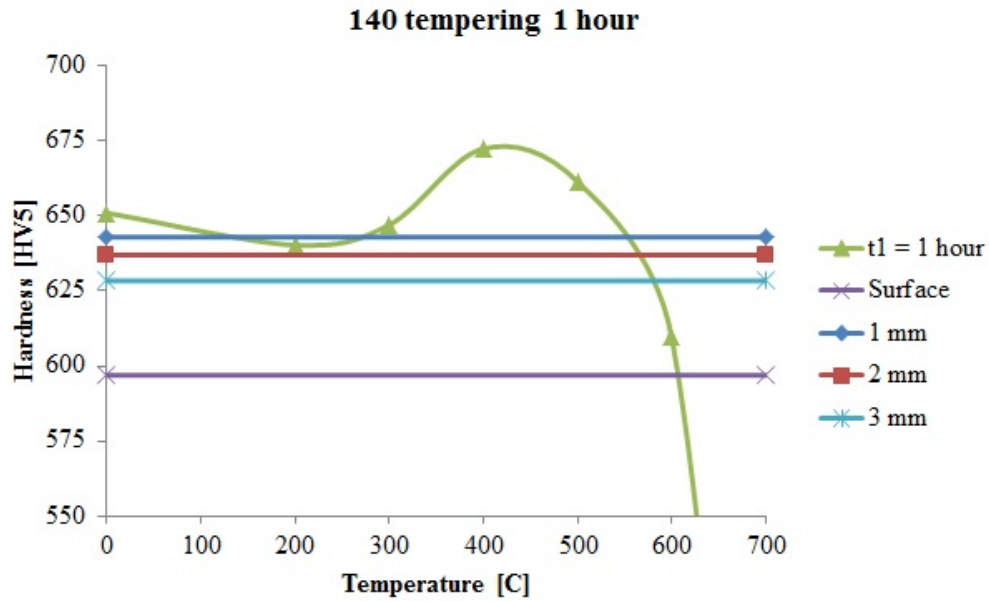


Figure 4.37: Hardness profile of cutter disc HD₄ after 1 hour of tempering. Horizontal lines indicate hardness at known distances from the wear surface of TBM cutter 140.

Figure 4.37 shows the hardness of TBM cutter 140 compared to the tempering profile for the one hour test. A surface temperature of approximately 620 °C is seen. The hardness measurements at distances further from the surface appear to show an increase in temperature inwards, with 3 mm corresponding to a higher temperature than 1 mm. This result indicates a sharp temperature gradient, resembling the hardness profile seen in Figure 4.33. The small differences measured are probably scatter caused by retained austenite or brittle zones.

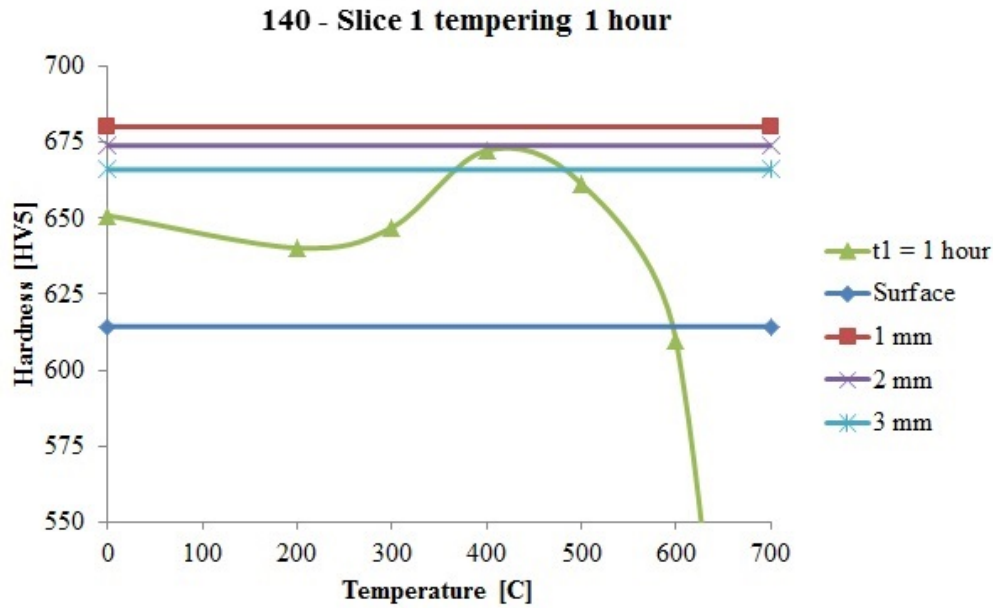


Figure 4.38: Hardness profile of cutter disc HD4 after 1 hour of tempering. Horizontal lines indicate hardness at known distances from the wear surface of TBM cutter 314, slice 1.

Figure 4.38 shows the hardness of cutter 314 compared to the 1 hour tempering profile of HD4. A surface temperature of approximately 600 °C is seen. This is followed by a steep temperature gradient, as seen for cutter 140. No speculations about the temperature at distances further from the surface can be based on this graph, as the 1 mm measurement does not intersect the tempering curve. A sharp temperature gradient was expected, as this would correlate with the hardness profile shown in Figure 4.29.

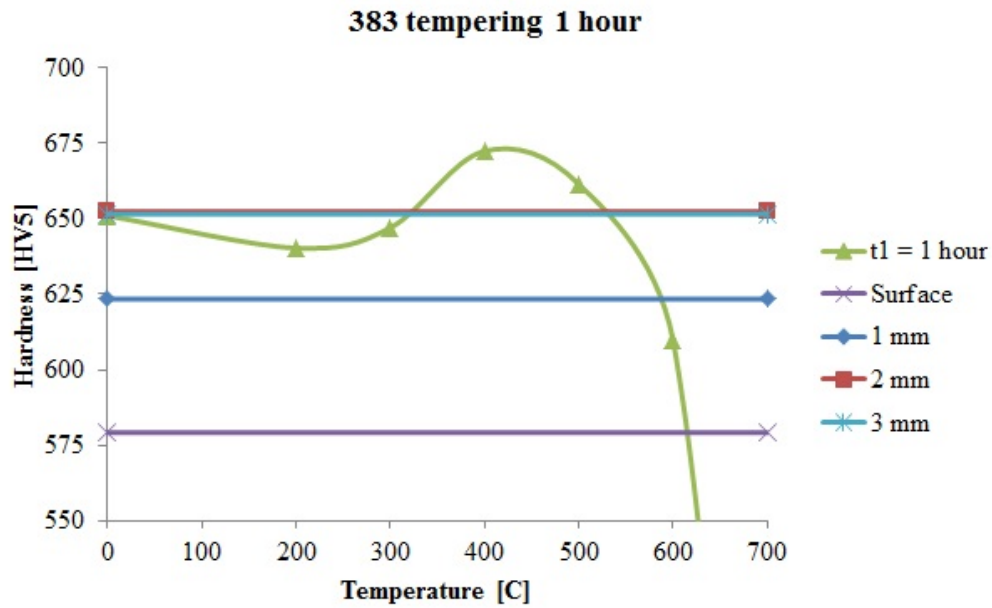


Figure 4.39: Hardness profile of cutter disc HD_4 after 1 hour of tempering. Horizontal lines indicate hardness at known distances from the wear surface of TBM cutter 383.

Figure 4.39 shows the hardness of TBM cutter 383 compared to the 1 hour tempering profile. Surface temperatures are found to be approximately 620 °C, with falling temperatures as measurements are performed deeper into the cutter material. The graphs for two hours holding time are found in Appendix E. A holding time of 4 hours is not deemed realistic and these graphs will therefore not be presented in this master's thesis.

Chapter 5

Discussion

5.1 Field Data from Røssåga

Field data from Røssåga show abrasive wear to be the dominant cause of replacement for cutter discs. As seen in Figure 4.1, blocked discs account for 20 % of all replacements, while 16 % is credited to chipping. This is to be expected, as rock testing results show highly abrasive rock in most of the areas tested during this project. Figure 4.2 illustrate the importance of cutter head position as a function of cutter consumption. Differences in wear mechanisms are noted even for neighbouring cutters. Figure 4.4 shows an average cutter life of just over 100 m³/cutter in the area where cutters 314 and 302 are collected. The average is seen to be approximately 250 m³/cutter for cutters 140 and 383. The reasons for cutter replacements in the mentioned regions are similar, with abrasion being the most dominant. A notable change recorded is a threefold increase of replacements due to chipping as the cutter life is near tripled. As chipping is caused by crack growth, it is closely related to fatigue. The variations in load recorded in Figure 2.24 and Figure 2.24b imply an increase in fatigue-caused cracking by time. The rise in cutter life corresponds well with this notion, as high abrasivity leads to less rock chipping, actually reducing the load variations experienced by the cutters. This is believed to reduce the influence of fatigue on the cutters.

Figure 4.5 shows the evolution of wear on the TBM cutter analysed. While cutters 140 and 383 experience a linear wear rate from start until replacement, the results from cutters 302 and 314 indicate extraordinary circumstances and measuring error. This is seen by their rolling distance in excess of 600 km in highly abrasive rock and reduced wear measured at different intervals. A possible explanation is that both cutters were worn at similar speeds as 140 and 383, but neglected during replacement intervals. With new cutters inserted on both sides of the worn ones, the discs were not in proper use prior to their replacements. Such a scenario corresponds to the results only in very hard rock, which was the case, as seen in Figure 4.4. It is noted that cutter 314 rolled almost 600 km at position 23, which has a recorded average rolling distance of 750 km/cutter. No reasons for this extensive lifetime at

one specific position has been found and no discussion will therefore be given.

Figure 4.6 shows a comparison of the linear part of wear on cutter 314 along side cutters 140 and 383. An equal wear rate is seen for discs 140 and 314. Cutter 383 experienced half the wear of the other two. As cutters 140 and 383 were worn at the same time, this difference is probably due to their position on the cutter head. A correlation may also be found by studying the influence of neighbouring cutter replacements, but no such data have been analysed in this study.

5.2 Failure Mechanism Examination

Microstructural analysis were performed on all TBM cutters and RIAT mini-cutters with the intention of identifying the different wear mechanisms active during tunnelling operations. As far as practicable, the results will be discussed by comparing TBM discs to RIAT mini-cutters.

Modes of Contact

The first area of interest is the mode of contact which occur in TBM cutters and RIAT mini-cutters. From section 2.4.2 it is seen that sliding contact, if the frictional forces are of sufficient magnitude, will produce a lamellar pattern close to the contact surface. A separation is made between lamellar structures parallel and perpendicular to the rolling direction. If sliding is a dominating contact mode, the lamellar structure will be visible in parallel. Plastic deformation during rolling contact mode may cause a similar structure, but this will be in the perpendicular direction. To study dominating modes of contact, cross sections parallel to the rolling direction were made.

Figure 4.7, showing TBM cutter 314, indicate rolling as the dominating mode of contact in TBM operations. This is seen from the lack of a lamellar deformation layer close to the surface. The fact that no TBM cutter showed signs of sliding contact indicate a predominant rolling behaviour, even during changing geologies. The same was not true for the RIAT mini-cutters, as lamellar structures were found both in quartzite, Iddefjord granite and Chinese basalt. Thickness of the lamellar layer was however observed to vary in thickness, with Chinese basalt producing the largest sliding component and quartzite only showing periodic indications, illustrated in Figure 4.8 and Figure 4.9. A correlation between abrasiveness and plastic deformation is therefore seen, as also reported by [39]. This correlation of course also affects the mode of contact, as a rolling mode will produce less deformation than sliding.

Wear Mechanisms

As mentioned earlier, a lamellar layer in the direction perpendicular to the rolling motion does not necessarily indicate mode of contact. Figure 4.12 shows a transverse

cross section of TBM cutter 302. A lamellar structure is clearly shown. The probable cause of this layer is plastic deformation by folding of asperities. What is seen is crack growth parallel to the lamellae. It is probable that the crack created by the folding has grown by fatigue from cyclic loading. This effect is also seen in the parallel cross section of cutter 302 in Figure 4.13. What may have started as a fold initiated crack appears to have grown into the material to a level beyond the surface plane, depicted in Figure 4.13. In addition, subsurface initiated cracks are found in Figure 4.14. These are clear indications of wear by fatigue, common in rolling contacts. If allowed to grow, these cracks will reach the surface causing chips of debris to be released. This wear mechanism is seen to cause 17 % of all TBM cutter replacements in Figure 4.1.

The optical images of Chinese basalt and Iddefjord granite shown in Figure 4.15 and Figure 4.16 respectively, show a natural progression of crack growth from asperities. The Chinese basalt mini-cutter in Figure 4.15 shows an asperity folding about to occur, with further cyclic loading likely to cause crack growth. This has further progressed in Figure 4.16, where the crack is about to re-surface to create wear debris. Given longer runtime it is believed that fatigue would have been a larger contributor to wear than what is apparent at this stage.

As already seen in Figure 4.1, abrasion is the dominating wear mechanism in TBM cutters. Signs of abrasion by ploughing and cutting were also found in RIAT mini-cutters worn by quartzite and granite. The parallel lines seen in Figure 4.17 and Figure 4.18 clearly indicate abrasive wear. The more pronounced lines in Figure 4.17, which was worn by quartzite, further state this to be more exposed to aggressive abrasion than the sample worn by Iddefjord granite. This is to be expected as quartzite is the most abrasive rock type used in these tests. Figure 4.18 shows rock debris stuck in the surface as brightly coloured areas. With increased abrasivity, the amount of rock debris found in the wear surface is reduced. These results correlate well with the findings presented in Section 2.5.3.

Deformation Structure

Along with microstructural analysis, the presence of nanocrystalline layers were studied to compare the deformation in TBM cutters and RIAT mini-cutters.

Section 2.3.3 states that a strain of 7 to 8 is needed as a minimum to create nanocrystalline deformation layers. Such layers were found in TBM cutters 314, 302 and 383 and in all RIAT mini-cutters. TBM cutter 140 showed no signs of such a layer. A difference in layer thickness was noted in the TBM cutters. 1-1.5 μm thick layers were seen in cutters 314 and 383. FIB images from cutter 302 indicated 2-6 μm thick nanocrystalline layers. The layer thickness in cutter 302 varied with cross sectional direction. A 2-3 μm layer was observed in the transverse direction, while the cross section parallel to the rolling motion showed a layer 4-6 μm thick. No such deviation was found in the cross sections of cutter 140, but these results lack in comparison as no nanocrystalline layer was found in either cross section. It

is therefore not possible to conclude why such deviating values were observed. For further conclusions, several cross sections must be observed in different areas of the samples. Electron backscattered diffraction (EBSD) analysis would also give better results, as they might indicate texture of the grains.

The cross sections of the RIAT mini-cutters all indicated nanocrystalline layers of approximately 2-3 μm thickness. A coarser microstructure below the deformed layer of sample 11 is observed. The lamellar layer found in mini-cutter 11, worn by quartzite, by optical microscope was determined to be less dominant than those seen in samples worn by granite and basalt. This may indicate layers of highly deformed material below the nanocrystalline layer in the basalt and granite samples. Such a result corresponds well with the recorded contact mode of the RIAT cutters. Quartzite was found to have only a slight sliding component, indicated by a less deformed microstructure below the nanocrystalline layer. A more dominant sliding component should introduce greater plastic deformation, producing a highly deformed microstructure.

The high deformation in the near surface microstructure also made determining the nanocrystalline layer thickness difficult. This was seen in RIAT mini-cutters worn by granite and basalt and TBM cutters 302 and 383. TBM cutter 314 and 140 were worn by the same rock types as cutters 302 and 383 respectively. The lack of similar deformation in these cutters reduce the comparability between rock abrasivity and nanocrystalline deformation layer thickness for TBM discs. However, a difference is seen in the RIAT mini-cutters, indicating a correlation between rock abrasivity and deformation structure. Highly abrasive rock appears to reduce the thickness of the nanocrystalline deformation layer. Further testing should be performed on RIAT mini-cutters without lamellar deformation structures for better accuracy in the results.

5.3 Tempering

Figure 2.24 shows the forces measured on TBM cutter discs in situ. As mentioned in Section 2.4.3, the true contact area is actually only asperities on the surface. The small area combined with high forces indicate that the cutter surface is exposed to extreme stresses during use. It is to be expected that the magnitude of these stresses will cause plastic deformation in the contact points on the cutter surface. This generates dislocations and transforms retained austenite to untempered martensite, both effects leading to work hardening of the metal. Such an effect is seen in the hardness profiles of TBM cutters 314, slice 2, and 302, shown in Figure 4.30 and Figure 4.31 respectively. It is also indicated in RIAT mini-cutter number 3 in Figure 4.32.

A thinner layer of work hardened material is seen in the RIAT mini-cutter relative to the TBM cutters. This is natural due to the difference in load experienced by the TBM and RIAT cutters. The spatial resolution of the micro hardness indenter

was too low to obtain a clear hardness gradient in the RIAT samples. It should be noted that the most work hardened parts of samples 302 and 314 show an increase of 12.1 and 6.1 %, respectively. The hardening in the RIAT sample is measured to be 6.5 % and the plastic deformation is therefore assumed to be of the same order of magnitude in the RIAT mini-cutter and TBM cutters. This was also indicated by the FIB cross sections, where a similar thickness of the nanocrystalline layers were observed in several RIAT and TBM cutters.

Softening is apparent in the measurements of TBM cutter 314, slice 1. This softening is also observed in cutters 140 and 383. Reduction in hardness in martensitic steel is brought about by tempering or decarburization. Both processes require high temperatures to be effective in short time spans. The tempering results from sample HD4, show a peak hardness reached at around 500 °C prior to extensive softening. This hardness increase is possibly caused by precipitation of VC particles. As mentioned in Section 2.3.2, small and finely spread precipitates hinder dislocations, thereby increasing yield strength. Such particles were seen in all FIB cross sections of both TBM cutters and RIAT mini-cutters. No particle density measurements were made from FIB imagery. It is recommended that such an analysis is performed in full cross sections in either SEM or optical microscope. This will provide better view of the gradients of particle coarsening. No such gradient is probable in the FIB images, where the maximum depth studied was approximately 15 μm .

Section 2.4.3 states that most of the energy expended in plastic deformation is converted to heat. Also, with sufficient strain rate, heat generation is effectively adiabatic, transferring negligible amounts of heat to the surrounding areas. Heat generated from such a deformation will therefore lead to a very high local temperature, as seen in Figure 2.20, potentially softening the metal through tempering. The local temperature increase may be used to explain the discrepancy found in slice 1 and 2 of TBM cutter 314. Two different measurements indicate hardening (slice 2) and softening (slice 1), illustrating the local variations found. The linear difference between the hardness measurements taken in the two slices was 1.5 cm. These soft zones may prove ideal for crack initiation, as softer steel was found to be more prone to wear by highly abrasive rocks [39]. However, no crack initiation in soft zones has been observed during this work. Further analysis is therefore needed prior to further discussions on this subject.

In cutters 140, 314 and 383, bulk hardness is restored approximately 0.5 mm from the surface indentation. This is surprising, as cutters 140 and 383 were exposed to quite different geologies than cutter 314, varying significantly in abrasivity and cutter life as seen in Figure 4.4. The FIB cross sections of cutter 140 showed no nanocrystalline deformation layer, while the cross section from 314 indicated a layer of thickness 1 μm . This difference may be caused by the less abrasive rock found in the area of cutter 140. A conflicting result was the increase in near surface deformation with reduced rock abrasivity, found in the RIAT mini-cutters. In addition, the deformation observed in cutter 383 by FIB was far greater than that of disc 314. Further study is therefore needed to examine the root causes for

these conflicting results.

A tempering experiment was performed with samples cut from the HD4 cutter disc. The section of the cutter used had not been exposed to deformation and is therefore regarded as new. Some secondary hardening was seen at 300 to 500 °C prior to a loss of hardness going all the way to sub 300 HV5 at 700 °C. A comparison was also made of the surface hardness of cutters 140, 314 and 383 relative to the tempering profile. The lines indicated a temperature at the first hardness indentation of approximately 600-620 °C. It should be noted that the first indentation was made at a distance x , $0.04 < x < 0.1$ mm from the surface, indicating a surface temperature higher than the ones indicated here. As tempering is diffusion dependent, temperature and time are governing parameters. Shorter holding times require higher temperatures to obtain the same results. Further testing should therefore consider studying shorter holding times for temperature mapping. No data on TBM operational times were used during this work, but one hour of continuous operations is believed to be feasible. As this will not equal a tempering time of one hour, the actual holding temperature is probably shorter. This indicate a higher surface temperature than indicated in these experiments.

The lack of heat penetration from deformation is illustrated in the tempering comparison for cutter 140. The horizontal line symbolizing 3 mm from the surface appears to have reached a higher temperature than the areas 1 and 2 mm closer to the edge. It is more likely that the temperature never reached 400 °C beyond 0.5 mm from the surface, as was also indicated by the hardness profile in Figure 4.33. With strain rates in excess of 10/s, heat conductivity is poor, resulting in high local temperatures. This might explain the sharp temperature gradients found in cutters 140 and 314 and the local softening from disc 314, slice 1. Such an argument is supported by the FIB cross section of cutter 314, showing a nanocrystalline deformation layer, but only a thin layer of deformed microstructure before bulk material is seen. It is however thwarted by the cross section of cutter 140, showing no clear indication of plastic deformation. No clear conclusions may therefore be drawn based on the current results of these discs.

Figure 4.39, showing temperatures compared with the hardness profile of cutter 383, indicate a surface temperature in excess of 620 °C. In contrast to sample 140 and 314, a reasonable temperature gradient was seen, with temperatures at 1 mm shown to be 590 °C and at 2 and 3 mm even lower. The hardnesses measured at 2 and 3 mm from the edge are virtually the same, and both intersect the tempering profile in three places. One possibility is that the temperature 2 mm from the edge reach 540 °C, while the temperature at 3 mm is 320 °C. This corresponds to the lines actually intersecting the right and left side of the top, respectively. If this was the case, it would be natural to find an increase in hardness between these distances in Figure 4.34. Despite a large spread in hardness, this might actually be the case, as all hardness indentations in this area lay above the trendline. This gives some support to the hypothesis above. Grain growth observed in FIB supports the theory of a high surface temperature in cutter 383.

It should be noted that the temperatures indicated at the surface by tempering experiments may be upper estimates. This is due to the increase in free energy from plastic deformations. The influence of dislocations could also give reason to why the hardness profile of cutter 314 was so steep. A highly deformed area will contain more dislocations than an area of low deformation. These dislocations are assumed to increase the tempering reaction kinetics. If the temperatures reached are the same in both areas, tempering will occur at a higher rate in the highly deformed area, leading to greater softening. A thin layer of high deformation will thereby correspond to a steep hardness gradient. A balance of the effect from shorter holding times and added plastic deformation will govern the kinetics of the tempering reactions. Tempering tests with plastically deformed material should be performed at shorter holding times to study this hypothesis.

The final piece of information to be alluded by the tempering profile of Figure 4.35 is the heat treatment used on production of all the TBM cutter discs. This may be done by comparing the bulk hardness of the RIAT mini-cutter shown in Figure 4.32 with the tempering profile. As mentioned in section 3.1, the RIAT mini-cutters are tempered twice for 2 hours at 600 °C. From the four hour tempering in Figure 4.35, this corresponds to a hardness of 550 HV5, which is also seen as the bulk hardness from Figure 4.32. It is therefore possible that the TBM discs undergo a minimal tempering prior to use, relying only on austenitization at approximately 1020 °C.

Chapter 6

Conclusion and Future Work

6.1 Conclusion

The goal of this master's thesis was to investigate the cause of failure and the temperatures reached at the contact surface of failed cutter rings. Samples from two different scales, a full scale TBM stationed in Røssåga and a miniature scale laboratory experiment, RIAT, have been analysed. An overview of cutter replacement statistics has also been presented.

It establishes that general wear is the most dominant wear factor, by causing 52 % of all replacements. This corresponds well with rock analysis, with AVS values rating the rock mass as highly abrasive. An increase in fatigue wear is seen with reduced abrasivity and increased cutter life. This is probably caused by heavier fluctuations in load from rock crushing, as well as prolonged exposure to such cyclic loads.

Examinations of the microstructure in both sample types indicate rolling as the primary mode of contact. A slight component of sliding contact was seen in the RIAT samples, with increasing importance corresponding to reduced abrasiveness of the rock type.

Fatigue was seen to cause wear in the TBM cutters. This was indicated by formation of subsurface cracks, and growth of cracks formed by folding of asperities. Abrasive wear has been established by SEM imaging of the RIAT mini-cutters.

Cross sections were made by way of FIB for microstructural analysis. Nanocrystalline deformation layers were seen in both TBM cutters and RIAT mini-cutters. This indicate comparable deformations in the two processes. The lack of such a layer in one TBM cutter correlate low abrasivity to low plastic deformation. The opposite indication is seen by RIAT testing, where high abrasivity indicate a thinner deformation layer. However, too few samples were analysed for decisive conclusions on this point to be made.

Hardness profiles of the different steel samples have been made. The tests showed work hardening in both TBM cutters and RIAT mini-cutters, but also showed significant softening in some of the TBM cutters. The samples showing work hardening

were in good agreement with each other, showing an increase in hardness of approximately 6-12 %.

A tempering experiment was carried out on samples from an unused TBM cutter and a hardness profile made to correlate the different temperatures to distances from the surface of the worn cutters. Results indicate a temperature in excess of 620 °C at the surface of several discs. No clear pattern was found with regards to temperature gradients into the cutter, indicating heating from very rapid deformation ($>10/s$). Temperatures of 540 °C and 320 °C were recorded 2 and 3 mm from the cutter surface, respectively. The temperatures found are regarded as unsure, due to the influence of stored energy and holding time on tempering. Signs of grain growth in one cutter indicate a high temperature, but no conclusions can be made at the present time. No such temperature increase was found in the RIAT mini-cutters.

6.2 Future Work

A main goal of this study is to better understand the wear mechanisms in the deformed surface of a cutter disc. In future work:

- Several samples, from different areas of the cutter head, should be analysed to observe metallurgical differences within the same geology and operational parameters.
- Several tempering experiments, at 1 hour and shorter holding times, should be performed, both on undeformed and deformed samples.
- A finer mesh of indentations will give better insight to the evolution of hardness due to tempering of the material.
- RIAT mini-cutters should be used on geological samples taken from Røssåga at the same positions where the analysed TBM cutters are used. This will introduce better grounds for correlation of data than what is possible at the moment.
- Chemical analysis should be performed on all TBM cutter discs involved in the experiment to verify if the cutters are made from the same alloy. This will improve the integrity of the results.

Bibliography

- [1] B. Maidl, L. Schmid, W. Ritz, and M. Herrenknecht, *Hardrock tunnel boring machines*. John Wiley & Sons, 2012.
- [2] G. B. Hemphill, “Tunnel-Boring Machines,” *Practical Tunnel Construction*, pp. 171–185.
- [3] G. Girmscheid and C. Schexnayder, “Tunnel boring machines,” *Practice periodical on structural design and construction*, vol. 8, no. 3, pp. 150–163, 2003.
- [4] C. Frenzel, *Wear patterns and prediction of disc cutter consumption for tunnel boring machines*, 2011.
- [5] A. Bruland, *Hard rock tunnel boring*. Fakultet for ingeniørvitenskap og teknologi, 2000.
- [6] EFNARC, *Specification and Guidelines for the use of specialist products for Mechanized Tunneling (TBM) in Soft Ground and Hard Rock*, 2005.
- [7] H. Bhadeshia and R. Honeycombe, *Steels: Microstructure and Properties: Microstructure and Properties*. Butterworth-Heinemann, 2011.
- [8] M. Hansen, K. Anderko, and H. Salzberg, “Constitution of binary alloys,” *Journal of the Electrochemical Society*, vol. 105, no. 12, pp. 260C–261C, 1958.
- [9] J. K. Solberg, *Teknologiske Metaller og Legeringer*, 2011.
- [10] W. D. Callister and D. G. Rethwisch, *Materials science and engineering: an introduction*. Wiley New York, 2007, vol. 7.
- [11] G. E. Dieter and D. Bacon, *Mechanical metallurgy*. McGraw-Hill New York, 1986, vol. 3.
- [12] A. Barron and C. Smith, “Crystal Structure,” Apr. 2015. [Online]. Available: http://cnx.org/contents/e90d5161-66b0-4214-bd6c-9f1d20a35bae@10/Crystal_Structure
- [13] M. Umemoto, “Nanocrystallization of steels by severe plastic deformation,” *Materials Transactions*, vol. 44, no. 10, pp. 1900–1911, 2003.

-
- [14] Y. Estrin and A. Vinogradov, "Extreme grain refinement by severe plastic deformation: A wealth of challenging science," *Acta Materialia*, vol. 61, pp. 782–817, Feb. 2013.
- [15] M. A. Meyers, A. Mishra, and D. J. Benson, "Mechanical properties of nanocrystalline materials," *Progress in Materials Science*, vol. 51, pp. 427–556, May 2006.
- [16] M. Wei, S. Wang, L. Wang, X. Cui, and K. Chen, "Effect of tempering conditions on wear resistance in various wear mechanisms of H13 steel," *Tribology International*, vol. 44, no. 7, pp. 898–905, 2011.
- [17] A. Rollett, F. J. Humphreys, G. S. Rohrer, and M. Hatherly, *Recrystallization and related annealing phenomena*. Elsevier, 2004.
- [18] Z. X. Yuan, S. H. Song, Y. H. Wang, J. Liu, and A. M. Guo, "Effect of pre-deformation on the age hardening of a niobium-microalloyed steel," *Materials Letters*, vol. 59, no. 16, pp. 2048–2051, Jul. 2005.
- [19] A. Bahrami, S. Anijdan, M. Golozar, M. Shamanian, and N. Varahram, "Effects of conventional heat treatment on wear resistance of AISI H13 tool steel," *Wear*, vol. 258, no. 5, pp. 846–851, 2005.
- [20] ASM, *Metallography and microstructures*, 2004, vol. 9.
- [21] T. L. Anderson, *Fracture mechanics: fundamentals and applications*. CRC press, 2005.
- [22] A. W. Batchelor and G. Stachowiak, *Engineering tribology*. Elsevier Science & Technology, 2005.
- [23] D. Rigney and J. Hirth, "Plastic deformation and sliding friction of metals," *Wear*, vol. 53, no. 2, pp. 345–370, 1979.
- [24] D. Rigney and W. Glaeser, "The significance of near surface microstructure in the wear process," *Wear*, vol. 46, no. 1, pp. 241–250, 1978.
- [25] N. Suh and H.-C. Sin, "On prediction of wear coefficients in sliding wear," *ASLE transactions*, vol. 26, no. 3, pp. 360–366, 1983.
- [26] F. Franklin, G.-J. Weeda, A. Kapoor, and E. Hiensch, "Rolling contact fatigue and wear behaviour of the infrastar two-material rail," *Wear*, vol. 258, no. 7, pp. 1048–1054, 2005.
- [27] Y. H. Kim and R. Wagoner, "An analytical investigation of deformation-induced heating in tensile testing," *International journal of mechanical sciences*, vol. 29, no. 3, pp. 179–194, 1987.

-
- [28] J. H. Sung, J. H. Kim, and R. Wagoner, “A plastic constitutive equation incorporating strain, strain-rate, and temperature,” *International Journal of Plasticity*, vol. 26, no. 12, pp. 1746–1771, 2010.
- [29] C. Frenzel, H. Käsling, and K. Thuro, “Factors influencing disc cutter wear,” *Geomechanics and Tunnelling*, vol. 1, no. 1, pp. 55–60, 2008.
- [30] M. Köhler, U. Maidl, and L. Martak, “Abrasive wear and tool wear in shield tunnelling in soil/Abrasivität und Werkzeugverschleiß beim Schildvortrieb im Lockergestein,” *Geomechanics and Tunnelling*, vol. 4, no. 1, pp. 36–54, 2011.
- [31] G. West, “Rock abrasiveness testing for tunnelling,” *International Journal of Rock Mechanics and Mining Sciences & Geomechanics Abstracts*, vol. 26, pp. 151–160, Mar. 1989.
- [32] M. Alber, O. Yarali, F. Dahl, A. Bruland, H. Käsling, T. N. Michalakopoulos, M. Cardu, P. Hagan, H. Aydin, and A. Özarlan, “ISRM Suggested Method for Determining the Abrasivity of Rock by the CERCHAR Abrasivity Test,” *Rock Mechanics and Rock Engineering*, vol. 47, pp. 261–266, Jan. 2014.
- [33] H. Käsling and K. Thuro, “Determining rock abrasivity in the laboratory,” *Rock mechanics in civil and environmental engineering—Proc EUROCK*, pp. 425–428, 2010.
- [34] F. Dahl, A. Bruland, P. D. Jakobsen, B. Nilsen, and E. Grøv, “Classifications of properties influencing the drillability of rocks, based on the NTNU/SINTEF test method,” *Tunnelling and Underground Space Technology*, vol. 28, pp. 150–158, 2012.
- [35] M. Entacher, G. Winter, and R. Galler, “Cutter force measurement on tunnel boring machines: Implementation at Koralm tunnel,” *Tunnelling and Underground Space Technology*, vol. 38, pp. 487–496, 2013.
- [36] F. Dahl, E. Grøv, and T. Breivik, “Development of a new direct test method for estimating cutter life, based on the Sievers J miniature drill test,” *Tunnelling and Underground Space Technology*, vol. 22, no. 1, pp. 106–116, Jan. 2007.
- [37] F. Macias, A. Bruland, and F. Dahl, “New rock abrasivity test method by rolling disc,” *ISRM Congress 2015*, 2015.
- [38] J. Rostami, *Development of a force estimation model for rock fragmentation with disc cutters through theoretical modeling and physical measurement of crushed zone pressure*. Colorado School of Mines, 1997.
- [39] M. Petrica, M. Painsi, E. Badisch, and T. Peinsitt, “Wear Mechanisms on Martensitic Steels Generated by Different Rock Types in Two-Body Conditions,” *Tribology Letters*, vol. 53, no. 3, pp. 607–616, 2014.

-
- [40] V. Raitai, V. Heino, K. Valtonen, M. Vippolai, A. Kemppainen, P. Shtonen, and V.-T. Kuokkala, “Effect of abrasive properties on the high-stress three-body abrasion of steels and hard metals.”
- [41] K. Solbakken, “Gigantboremaskin til Røssåga,” 2014. [Online]. Available: <http://www.ranablad.no/naringsliv/article6470810.ece>
- [42] E. Krogstad, “Degradation mechanisms due to wear and corrosion interaction of cutter tools used in Tunnel Boring Machines.” Master’s thesis, Norwegian University of Science and Technology, NTNU, 2013.
- [43] Uddeholm, “Uddeholm Orvar Supreme | Uddeholm,” Apr. 2015. [Online]. Available: <http://www.uddeholm.com/products/orvar-supreme.php>
- [44] J. Hjelen, *Scanning elektron-mikroskopi*. Metallurgisk institutt, NTH, 1989.
- [45] NorFab, “Focused Ion Beam (FIB) microscopy (1405),” 2015. [Online]. Available: <http://ntnu.norfab.no/WebForms/Equipment/EquipmentView.aspx?toolId=6>

Appendices

Appendix A

Problem Text

THE NORWEGIAN UNIVERSITY
OF SCIENCE AND TECHNOLOGY
DEPARTMENT OF ENGINEERING DESIGN
AND MATERIALS

**MASTER THESIS SPRING 2015
FOR
STUD.TECHN. Jarand Nærland**

Failure mechanisms in cutter tools for tunnel boring

Tunnel Boring Machines (TBMs) are used to excavate long tunnels. The cutter head diameters for these machines are ranging from 3 to 15 m, and cutter disc diameters from 432 mm to 508 mm. Generally, TBMs can encounter all types of geology, from soft rock to extremely hard rock.

A specific area of interest for TBMs is their cutter discs consumption. The cutters are continuously wearing out as boring takes place and replacement of cutters can in some geological formation be as high as 15 % of the total tunneling cost. In some cases worn out cutter tools and in fact worn out cutter head structure can jeopardize whole tunneling projects.

The goal of this project is to perform a microscopical study of a group of failed cutter rings of a real tunnel project in order to investigate the degradation mechanics causing these failures and the temperatures achieved in the contacting surfaces. Temperature changes can lead to microstructural changes and thus unexpected failures. The goal is to map fracture mechanisms to different geological formations and disc positions on the TBM cutter head. Testing will be performed on samples from a full scale TBM and from a small-scale testing machine developed in a PhD project at NTNU. The ultimate goal is to evaluate the feasibility of the small-scale machine to be used as a tool for predicting failures.

The project will be conducted in close cooperation with world leading Tunnel Bore Machine (TBM) manufacturers (The Robbins company) and a tunnel project contractor.

Specific objectives of the project are:

- Identify the degradation mechanisms (microstructural changes) by using material characterization techniques (i.e.: Optical microscopy, SEM, FIB, XRD).
- Microstructure and hardness of the discs to correlate the changes in mechanical properties to tempering due to frictional heating during use.
- Identify the temperatures achieved in the cutter tool – rock interface during the boring process by analyzing the microstructural and hardness changes.
- Compare real failures (field data) with lab scale testing.
- Identify the role of the geology and cutting additives (if used in the application) in the degradation/failure of the tools.

Formal requirements:

Three weeks after start of the thesis work, an A3 sheet illustrating the work is to be handed in. A template for this presentation is available on the IPM's web site under the menu "Masteroppgave" (<http://www.ntnu.no/ipm/masteroppgave>). This sheet should be updated one week before the master's thesis is submitted.

Risk assessment of experimental activities shall always be performed. Experimental work defined in the problem description shall be planned and risk assessed up-front and within 3 weeks after receiving the problem text. Any specific experimental activities which are not properly covered by the general risk assessment shall be particularly assessed before performing the experimental work. Risk assessments should be signed by the supervisor and copies shall be included in the appendix of the thesis.

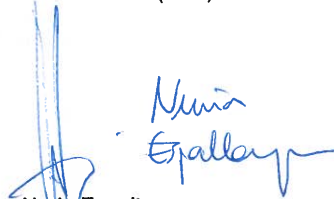
The thesis should include the signed problem text, and be written as a research report with summary both in English and Norwegian, conclusion, literature references, table of contents, etc. During preparation of the text, the candidate should make efforts to create a well arranged and well written report. To ease the evaluation of the thesis, it is important to cross-reference text, tables and figures. For evaluation of the work a thorough discussion of results is appreciated.

The thesis shall be submitted electronically via DAIM, NTNU's system for Digital Archiving and Submission of Master's theses.

The co-supervisor of the work is PhD candidate Francisco Javier Macías (BAT).



Torgeir Welo
Head of Division



Nuria Espallargas
Professor/Supervisor



Appendix B

Risk Analysis

NTNU	Utskriftet av	Nummer	Dato
	HMS-avd	HMSRV2801	22.03.2011
HMS	Godkjent av	Sida	Erstatler
	Rektor	01.12.2006	

Kartlegging av risikofylt aktivitet

Enhet: Institutt for Materialteknologi

Dato: 20.05.2015

Linjeleder: Jostein Mårdalen

Nuria Espallargas

(Ansv. veileder, student, evt. medveileder, evt. andre m. kompetanse)

Metallografisk undersøkning av verktøystål

Masteroppgave student Jarand Nærland. Failure mechanisms in cutter tools for tunnel boring

Kort beskrivelse av hovedaktivitet/hovedprosess:

NEI

*JA betyr at veileder innstår for at oppgaven ikke inneholder noen aktiviteter som krever risikovurdering

Signaturer:

Ansvartlig veileder:

Dersom 'JA': Beskriv kort aktiviteten i kartleggingskjemaet under. Risikovurdering trenger ikke å fylles ut.

Student:

ID nr.	Aktivitet/prosedyre	Ansvartlig	Existerende dokumentasjon	Eksterne sikkerhetsforhold	Lov, forskrift o.l.	Kommentar
1	Kutting	Student	Laboratorie- og verktøystedhandboken	Gjerast bak glassdeksel	Bruk av pålagt verneutstyr, HMS-prosedyrer	Fyll HMS-prosedyrer
2	Metallografisk sliping og polering	Student	Laboratorie- og verktøystedhandboken		Bruk av pålagt verneutstyr, HMS-prosedyrer	Fyll HMS-prosedyrer
3	Blanding av kjemikalier til prøveveising	Student	Laboratorie- og verktøystedhandboken	Avtrekkskap	Bruk av pålagt verneutstyr, HMS-prosedyrer	Fyll HMS-prosedyrer
4	Eising av prøver	Student	Laboratorie- og verktøystedhandboken	Avtrekkskap	Bruk av pålagt verneutstyr, HMS-prosedyrer	Fyll HMS-prosedyrer
5	Bruk av orm til temperering	Student	Laboratorie- og verktøystedhandboken	Verneløy for varme og ildlang	Bruk av pålagt verneutstyr, HMS-prosedyrer	Fyll HMS-prosedyrer
6	Bruk av hardleksmåler	Student	Laboratorie- og verktøystedhandboken		Bruk av pålagt verneutstyr, HMS-prosedyrer	Fyll HMS-prosedyrer
7	Lysmikroskopering	Student	Laboratorie- og verktøystedhandboken		Bruk av pålagt verneutstyr, HMS-prosedyrer	Fyll HMS-prosedyrer
8	SEM og FIB	Student	Laboratorie- og verktøystedhandboken		Bruk av pålagt verneutstyr, HMS-prosedyrer	Fyll HMS-prosedyrer
9	Kjøring til/tilbake testområde	Student		Billbelle og annen HMS-utstyr i bilen	Bruk av pålagt verneutstyr, HMS-prosedyrer	Fyll HMS-prosedyrer
10	Vilting av testområde	Student	Laboratorie- og verktøystedhandboken	All vilting i fylgje av områdeansvarlig	Bruk av pålagt verneutstyr, HMS-prosedyrer	Fyll HMS-prosedyrer

NTNU	Risikovurdering		Utbedret av	Nummer	Dato
			HMS-ansv.	HMSRV2803	04.02.2011
HMS/KS			Godkjent av	Skde	Erstater
			Rektor		09.02.2010
					

Dato: 20.05.2015

Enhet: Institutt for Materialteknologi
 Linjeleder: Jostein Mårdalen
 Deltakere ved risikovurderingen (nr/funksjon):
 (Ansv. veileder, student, evt. medveileder, evt. andre m. kompetanse)

Risikovurderingen gjelder hovedaktivitet:

Mastseppoppgave student Jarand Nærland. Failure mechanisms in cutter tools for tunnel boring

Signaturer:

Ansv. veileder: *Nina Egeberg*

Student:

Jarand Nærland

ID nr.	Aktivitet/prosess fra kartleggingskjølemaet	Mulig uønsket hendelse	Vurdering av sannsynlighet (1-5)	Vurdering av konsekvens			Risiko-verdi (menneske)	Kommentarer/ status Forslag til tiltak
				Menneske (A-E)	Vite miljø (A-E)	Øk./ Om-domme (A-E)		
1	Kutting	Kuttskader	1	B	A	A	B1	Bruk av vernebriller og hansker
2	Metallografisk sliping og polering	Slipeskader	5	A	A	A	A5	Bruk av vernebriller
3	Blanding av kjemikalier til prøvveisling	Etseskader	2	D	C	A	D2	Fylg HMS-prosedyrer
4	Eising av prøver	Etseskader	2	D	C	A	D2	Fylg HMS-prosedyrer
5	Bruk av omn til temperering	Brannskader	2	D	1	A	D2	Fylg HMS-prosedyrer
6	Bruk av hardleksmålar	Klærskader	1	B	1	A	B1	Fylg HMS-prosedyrer
7	Lysmikroskopering	Ufarlig for meg, men kan skade usisyr	1	A	A	B	A1	Fylg HMS-prosedyrer
8	SEM og FIB	Ufarlig for meg, men kan skade usisyr	1	A	A	C	A1	Fylg HMS-prosedyrer
9	Køyring til/frå testområde	Kollisjon	1	E	C	C	E1	Køyr varsamt
10	Vifting av testområde	Kan trefest av stein (prosjekttil)	1	E	A	A	E1	Opptre varsamt og etter rettleiing frå områdeansvarleg

Risikoverdi = Sannsynlighet (1, 2 ...) x konsekvens (A, B ...). Risikoverdi A1 betyr svært liten risiko, Risikoverdi E5 betyr svært stor og svært alvorlig risiko.

Sannsynlighet		Konsekvens					
Verdi	Kriterier	Gradering		Menneske	Ytre miljø: Vann, jord og luft	Øvmateriell	Omdømme
1	Svært liten: 1 gang pr 50 år eller sjeldnere	E	Svært alvorlig	Død	Svært langvarig og reversibel skade	Dritts- eller aktivitetsstans > 1 år.	Troverdighet og respekt, høydelig og varig svekket
2	Liten: 1 gang pr 10 år eller sjeldnere	D	Alvorlig	Alvorlig personskade. Mulig uføretet	Langvarig skade. Lang reslitusjonstid	Drittsstans > ½ år. aktivitetsstans oppill 1 år	Troverdighet og respekt høydelig svekket
3	Middels: 1 gang pr år eller sjeldnere	C	Moderat	Alvorlig personskade.	Mindre skade og lang reslitusjonstid	Dritts- eller aktivitetsstans < 1 mnd	Troverdighet og respekt svekket
4	Stor: 1 gang pr måned eller sjeldnere	B	Liten	Skade som krever medisinsk behandling	Mindre skade og kort reslitusjonstid	Dritts- eller aktivitetsstans < tjuke	Negativ påvirkning på troverdighet og respekt
5	Svært stor: Skjer ukenlig	A	Svært liten	Skade som krever førstehjelp	Ubehagelig skade og kort reslitusjonstid	Dritts- eller aktivitetsstans < 1dag	Liten påvirkning på troverdighet og respekt

MATRISE FOR RISIKOVURDERINGER ved NTNU

KONSEKVENNS		SANNSYNLIGHET				
Svært alvorlig	E1	E2	E3	E4	E5	
Alvorlig	D1	D2	D3	D4	D5	
Moderat	C1	C2	C3	C4	C5	
Liten	B1	B2	B3	B4	B5	
Svært liten	A1	A2	A3	A4	A5	
	Svært liten	Liten	Middels	Stor	Svært stor	
	SANNSYNLIGHET					

Prinsipp over akseptkriterium. Forklaring av fargene som er brukt i risikomatrisen.

Farge	Beskrivelse
Red	Uakseptabel risiko. Tiltak skal gjennomføres for å redusere risikoen.
Gul	Vurderingsområde. Tiltak skal vurderes.
Grønn	Akseptabel risiko. Tiltak kan vurderes ut fra andre hensyn.

Appendix D

Failure Mechanism Examination

D.1 Modes of Contact

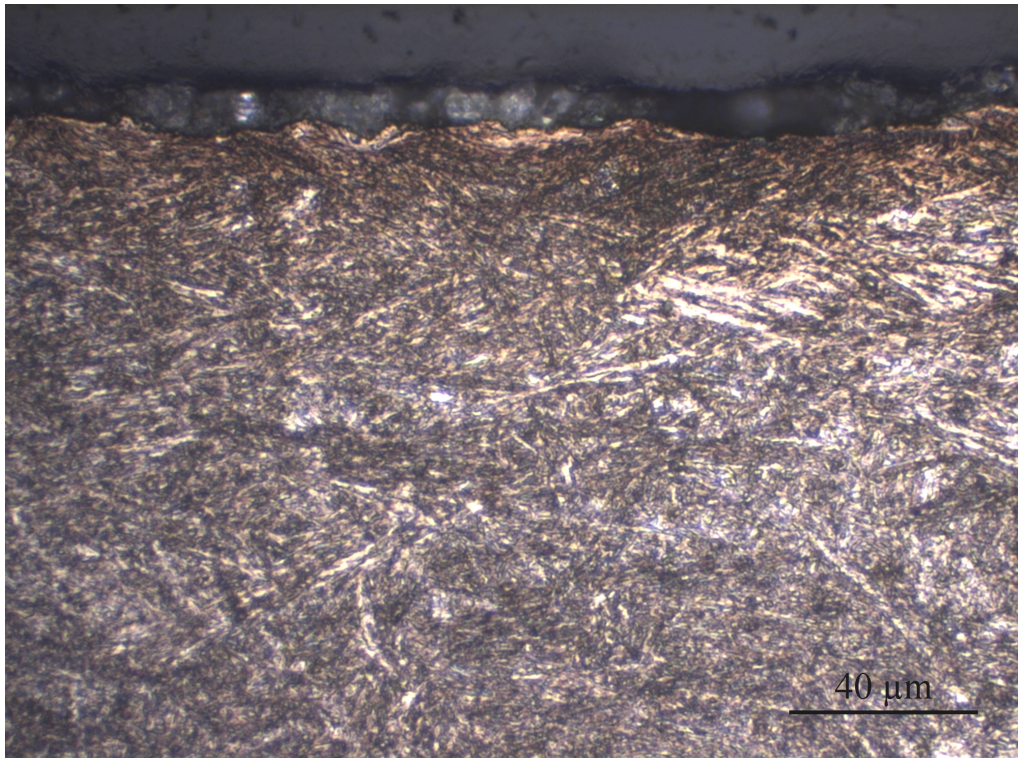


Figure D.1: Optical image of cross section in TBM cutter 140, transverse cut. No lamellar surface layer observed. Some deformation apparent, with no clear direction of orientation. 500X magnification.

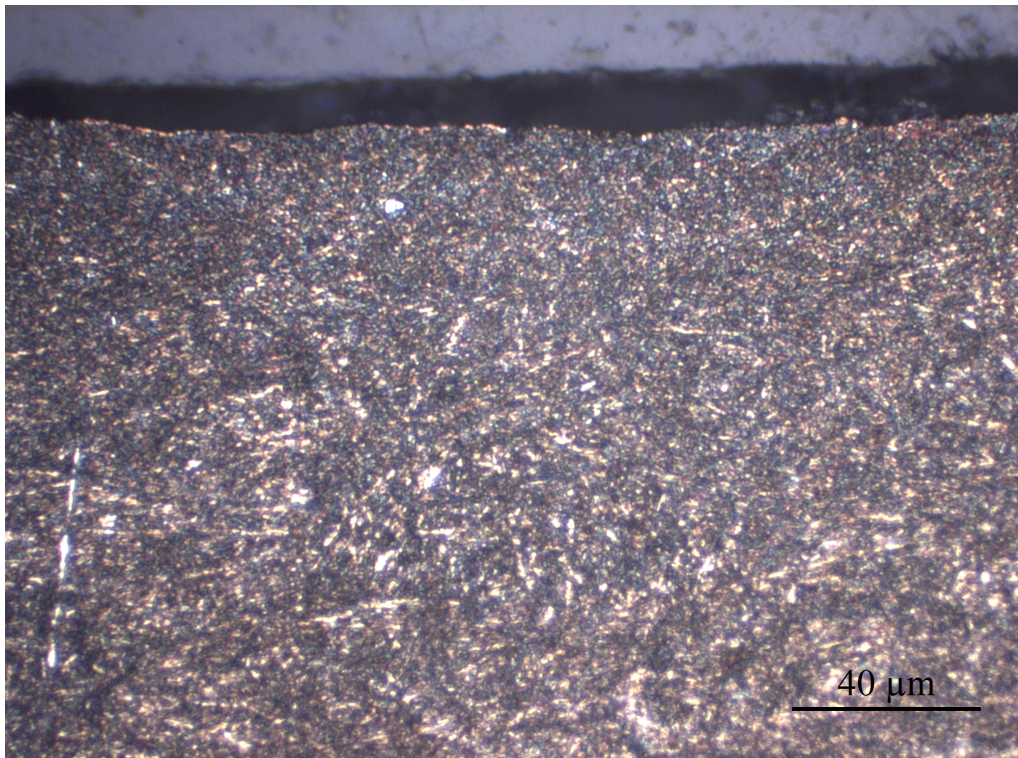


Figure D.2: Optical image of cross section in TBM cutter 302, transverse cut. No lamellar surface layer observed. Microstructure highly deformed, seen from lack of retained austenite (white phase). 500X magnification.

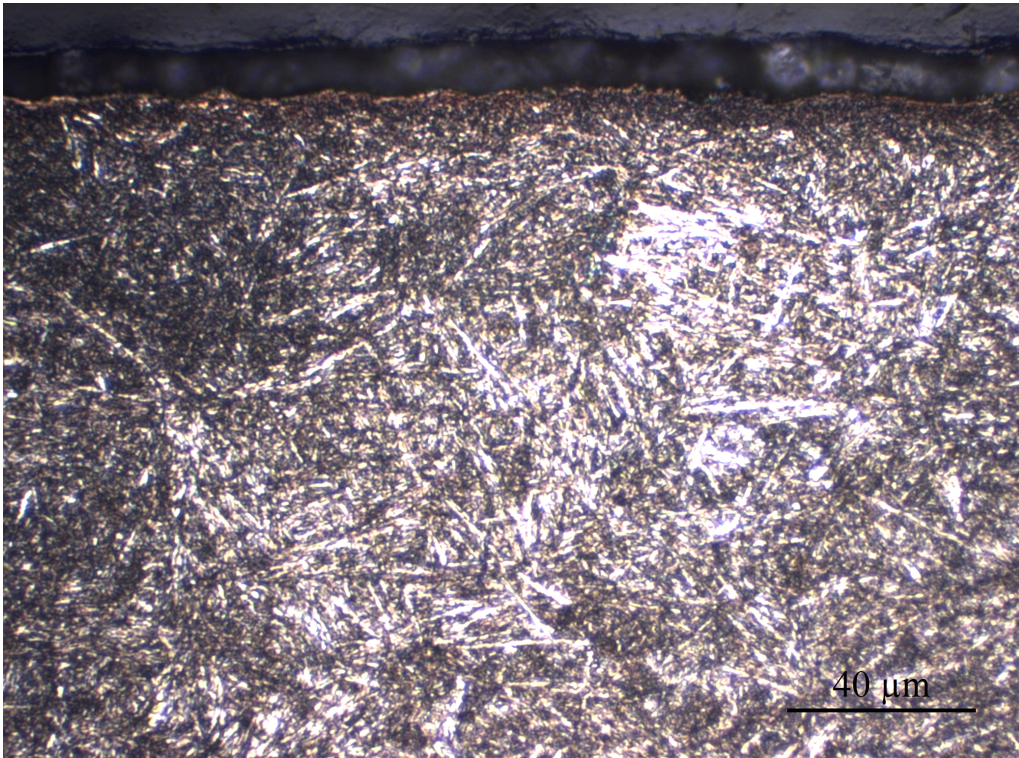


Figure D.3: Optical image of cross section in TBM cutter 383, transverse cut. No lamellar surface layer observed. Some deformation apparent at the surface. 500X magnification.

D.2 Wear Mechanisms

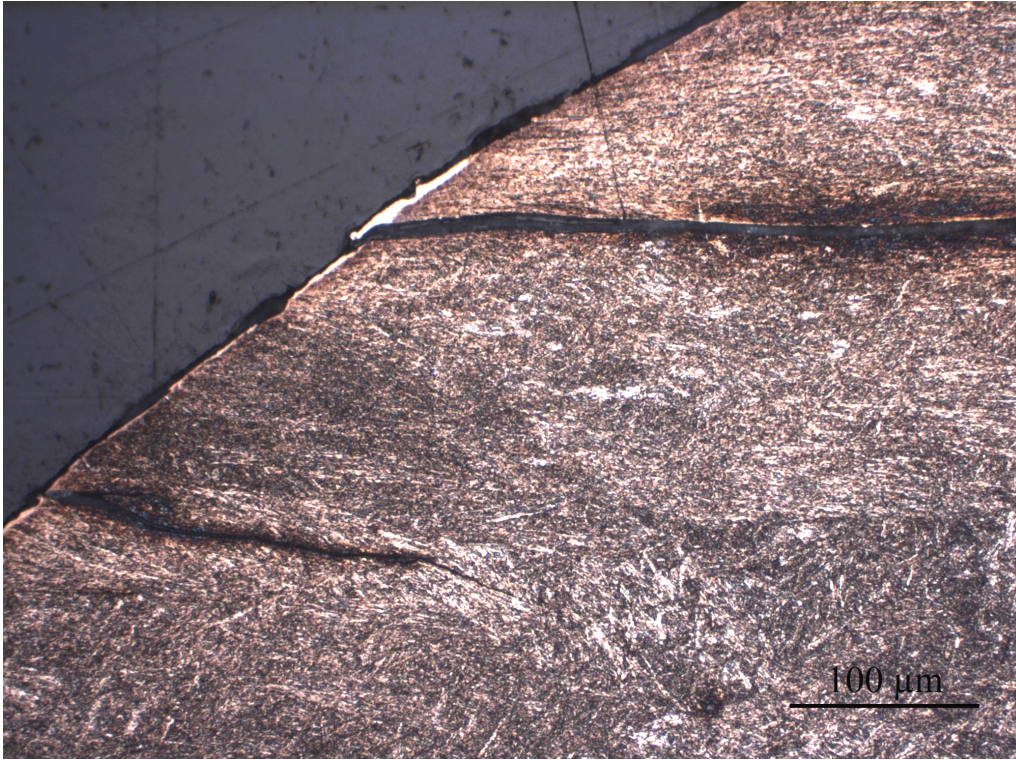


Figure D.4: Optical image of cross section in TBM cutter 314, parallel cut. Lamellar structure seen, with crack growth in parallel with the lamellae direction. Lamellar structure possibly caused by folding of asperities. 200X magnification.

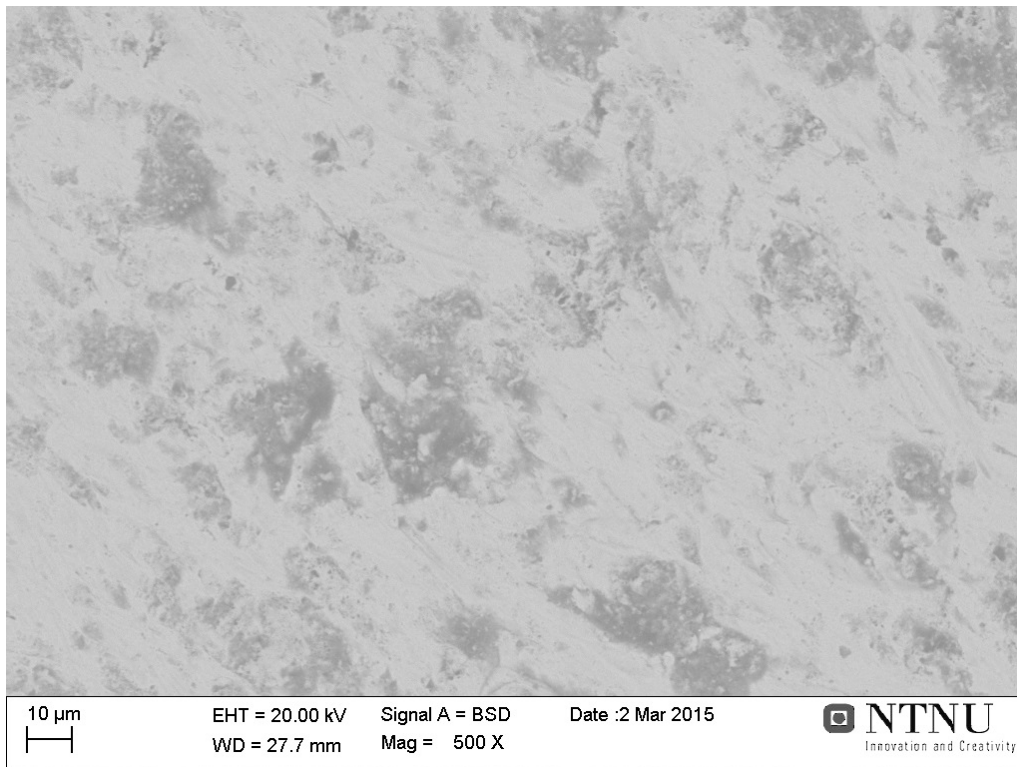


Figure D.5: SEM image of wear surface of RIAT mini-cutter 8, worn by quartzite. BSE signal. Bright areas are steel, dark areas are rock debris.

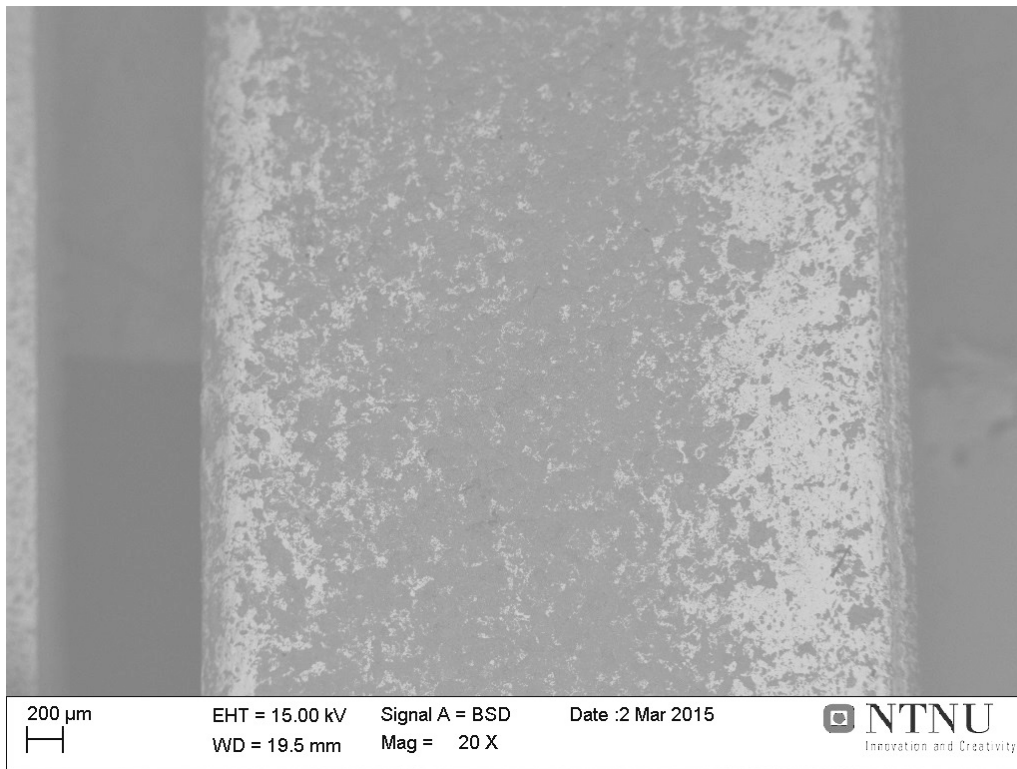


Figure D.6: SEM image of wear surface of RIAT mini-cutter 7, worn by basalt. BSE signal. Bright areas are steel, dark areas are rock debris.

D.3 Deformation Structure

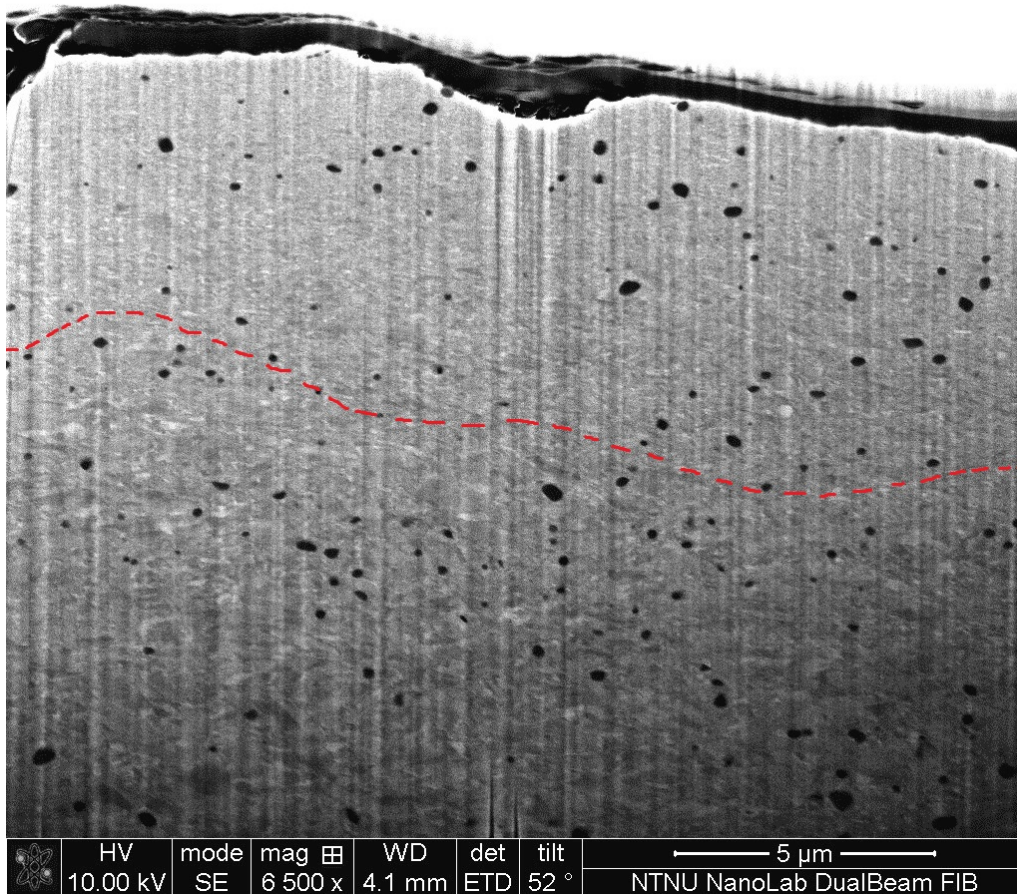


Figure D.7: FIB image of RIAT mini-cutter 3, worn by Iddefjord granite. Fine grained area visible at the surface of the specimen. Dotted line imply border for nanocrystalline deformation layer. Possible nanocrystalline layer approximately 5 - 7 μ m thick.

Appendix E

Tempering

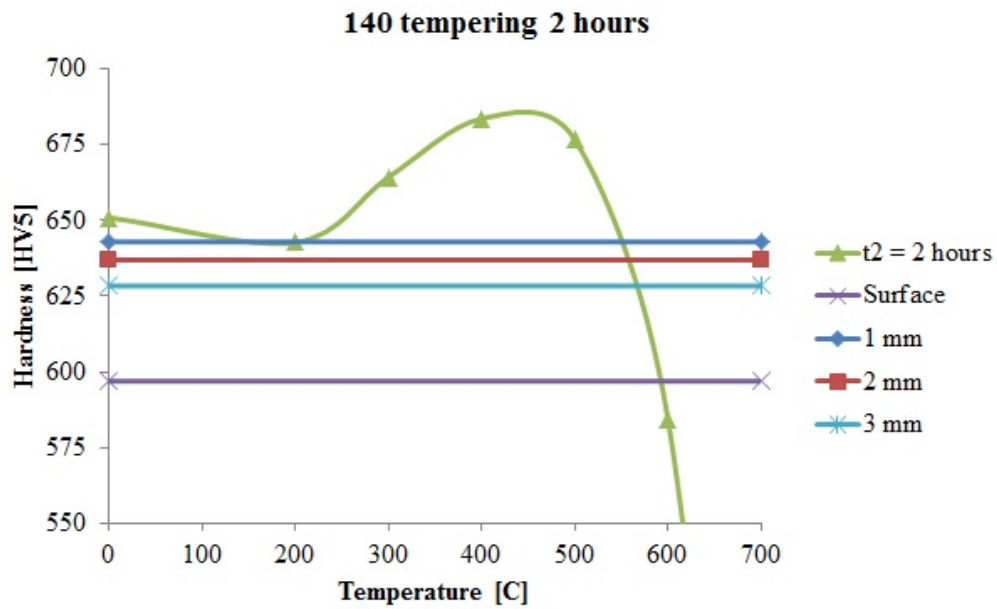


Figure E.1: Hardness profile of cutter disc HD₄ after 2 hours of tempering. Horizontal lines indicate hardness at known distances from the wear surface of TBM cutter 140.

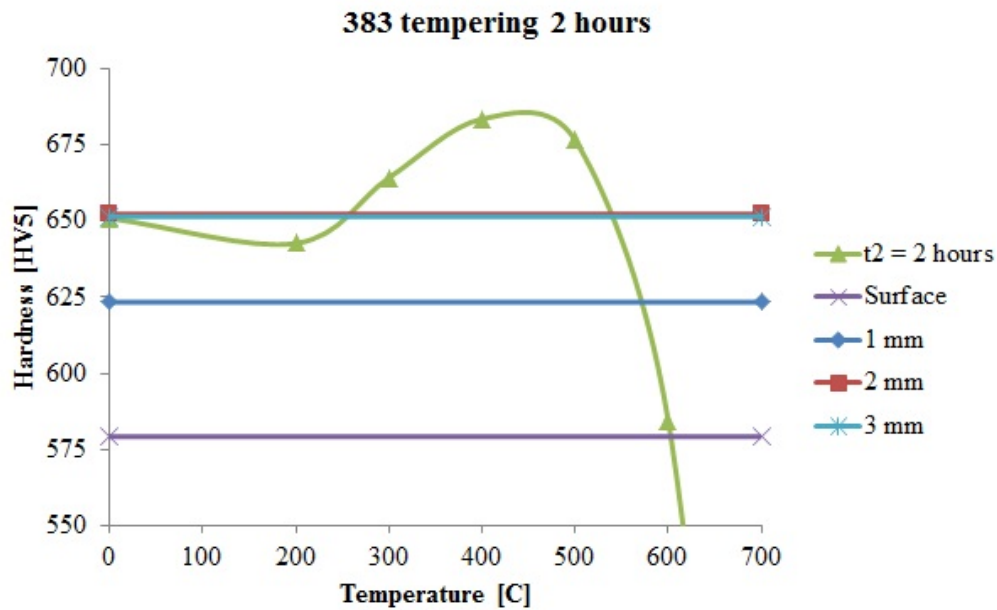


Figure E.2: Hardness profile of cutter disc HD_4 after 2 hours of tempering. Horizontal lines indicate hardness at known distances from the wear surface of TBM cutter 383.

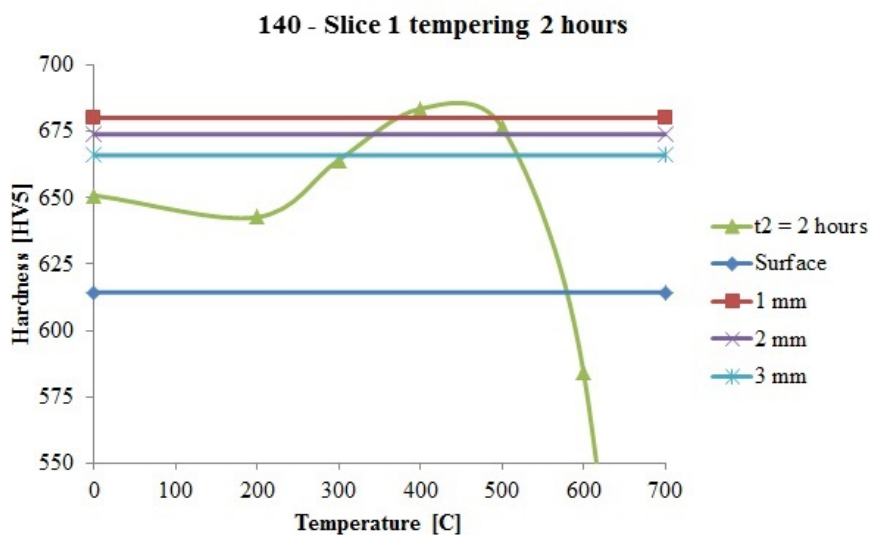


Figure E.3: Hardness profile of cutter disc HD_4 after 2 hours of tempering. Horizontal lines indicate hardness at known distances from the wear surface of TBM cutter 314.